E83-10355

SOIL TEMPERATURE INVESTIGATIONS USING SATELLITE ACQUIRED THERMAL-INFRARED DATA IN SEMI-ARID REGIONS

CR-172882

Rick L. Day

Gary W. Petersen

Department of Agronomy
College of Agriculture

and

Office for Remote Sensing of Earth Resources

Final Report
Contract Number NAS5-26612

to

National Aeronautics and Space Administration
Goddard Space Flight Center
Greenbelt, Maryland

THE PENNSYLVANIA STATE UNIVERSITY
UNIVERSITY PARK, PENNSYLVANIA

SOIL TEMPERATURE INVESTIGATIONS USING SATELLITE ACQUIRED THERMAL-INFRARED DATA IN SEMI-ARID REGIONS

Rick L. Day
Graduate Assistant

Gary W. Petersen
Professor of Soil Genesis and Morphology
Co-Director, ORSER

Department of Agronomy
College of Agriculture

and

Office for Remote Sensing of Earth Resources

Final Report
Contract Number NAS5-26612

The work upon which this report was based was supported by the National Aeronautics and Space Administration, Goddard Space Flight Center, Greenbelt, Maryland.

Institute for Research on Land and Water Resources
The Pennsylvania State University
University Park, Pennsylvania 16802

April 1983

ABSTRACT

Temperature is an important soil property influencing chemical, biological and physical processes and is a criterion for soil taxonomic classification. Most soil temperature measurements are randomly spaced, providing little information about their spatial landscape distribution. Thermal-infrared data acquired from the Heat Capacity Mapping Mission (HCMM) satellite were used to map the spatial distribution of diurnal surface temperatures and to estimate mean annual soil temperatures (MAST) and annual surface temperature amplitudes (AMP) in semi-arid east central Utah. Diurnal data with minimal snow and cloud cover were selected for five dates throughout a yearly period and geometrically co-registered using the Office for Remote Sensing of Earth Resources (ORSER) processing system. Rubber-sheet stretching was aided by the WARP program which allowed preview of image transformations. Daytime maximum and nighttime minimum temperatures were averaged, thereby generating an average daily temperature (ADT) data set for each of the five dates. Five ADT values for each pixel were used to fit a sine curve describing the theoretical annual surface temperature response as defined by a solution of a one-dimensional heat flow equation. Linearization of the equation produced estimates of MAST and AMP plus associated confidence statistics. MAST values were grouped into classes defined by the USDA Soil Survey Staff and displayed on a color video screen. Diurnal surface temperatures and MAST were primarily correlated with elevation. Aspect, moisture and soil and rock densities were of secondary importance.

HCMM, Landsat and Digital Terrain Elevation (DTE) data were spatially registered through a common 1:250000 scale topographic base map and merged digitally. Statistical relationships and redundancy among the combined data types were evaluated by channel correlation and principal component analysis. It was found that the DTE data was highly correlated with HCMM daytime and nighttime thermal-infrared data. Either DTE or HCMM thermal-infrared data improved the value of Landsat data by adding topographic information.

TABLE OF CONTENTS

TABLE OF CONTENTS (CONTINUED)

TABLE OF CONTENTS (CONTINUED)

LIST OF TABLES

LIST OF TABLES (CONTINUED)

LIST OF FIGURES

LIST OF FIGURES (CONTINUED)

LIST OF FIGURES (CONTINUED)

GENERAL INTRODUCTION

Temperature is an important component of a soil's natural environment. Biological, chemical and physical processes affecting biotic activity, vegetative adaptability, and soil formation are all partially controlled by soil temperature. Knowledge of the temperature environment of a soil can be used to infer important soil physical characteristics.

Thermal-infrared data from the Heat Capacity Mapping Mission (HCMM) satellite can be used to map the spatial variability of surface temperatures across a landscape. Orbital characteristics of the HCMM satellite provide diurnal and annual multi-temporal coverage over the same geographic area such that the dynamic nature of soil and rock temperatures can be monitored.

Additional surface terrain characteristics, such as albedo and topography, are provided by Landsat MSS and Digital Terrain Elevation (DTE) digital data. Digital overlay of HCMM, Landsat and DTE data can combine several types of information for comprehensive surface terrain analysis.

LITERATURE REVIEW

Factors Affecting Annual Soil Temperatures

Soil temperatures fluctuate on both diurnal and annual cycles. Smith 91964) and Shul'gin (1957) comprehensively discuss factors affecting these fluctuations. Diurnal temperature fluctuations decrease exponentially with depth and are generally not significant below 50 cm. The magnitude of diurnal and annual temperature fluctuations depends upon topographic position, vegetative cover,

surface albedo, moisture content, depth to groundwater, material density and mineral composition. Annual fluctuations caused by solar radiation fluctuations may penetrate to greater depths of approximately 14 meters (Smith et al., 1964).

Elevation and Latitude

Mean annual soil temperatures (MAST) decrease linearly with increasing elevation (Whittaker et al., 1968; Carter and Ciolkosz, 1980; Schmidlin, 1981). The rate of change varies depending on regional and localized climatic variability. Carter and Ciolkosz (1980) measured MAST reductions of 3.4°C/1000 m in the central Appalachians. Larger gradients of 6.4°C/1000 m and 8.9°C/1000 m were reported in Arizona (Whittaker et al., 1968) and Nevada (Shmidlin, 1981), respectively. Smith et al. (1964) reports that MAST generally decreases more slowly than mean annual air temperature (MAAT) with increasing elevation due to increased solar radiation and snow cover at higher elevations. Franzmeier et al. (1969) found that local topographic position can cause low-lying areas which are shaded in the morning and evening to be cooler than adjacent high areas.

The gradient of MAST and elevation varies seasonally. Whittaker et al. (1968) found that mean summer soil temperatures in Arizona decreased at a rate of 12.6°C/1000 m compared to mean winter soil temperatures which decreased at a rate of 5.4°C/1000 m. Winter cold air drainage and summer desert heating are contributing factors.

Average monthly soil temperatures fluctuate about the annual mean according to a sine curve in mid-latitudes. The amplitude of the sine curve decreases with elevation (Smith et al., 1964).

Latitude affects the duration of solar radiation thereby affecting soil temperatures. Carter and Ciolkosz (1980) estimated an increase in MAST of 0.68°C/100 km decrease in north latitude in the central Appalachians from data collected over three years. Schmidlin (1981) measured a gradient of 0.6°C/100 km in Nevada and reported similar results in California.

Slope and Aspect

The variation in direct-beam solar radiation on surfaces of varying aspect and slope results in differential surface heating, day lengths and moisture characteristics (Shul'gin, 1957; Oke, 1978). The radiant flux incident upon a surface is dependent not only upon slope and aspect, but the solar zenith angle, thereby incorporating time and latitude as factors (Oke, 1978).

Shul'gin (1957) found that south-facing slopes have highest soil temperatures followed by east-facing and west-facing slopes. North-facing slopes are coolest. Temperatures increase on south-facing and east-facing slopes with increasing slope gradient but drop on north and west-facing slopes. Schmidlin (1981) found that north and northeast aspects are coolest on slopes greater than 15 percent. South facing slopes are warmest and west and northwest aspects are warmer than east aspects.

South-facing slopes have smaller seasonal fluctuations than north-facing slopes (Smith et al., 1964). Franzmeier et al. (1969) found that the temperature difference between north and south-facing slopes is greater in winter than in summer. Temperatures of grass covered surfaces on north and south facing slopes showed differences of 2.2°C in winter and 1.7°C in summer.

Aspect differences affect temperatures greater on steep slopes. Schmidlin found less than a 1°C difference in MAST between aspects on slopes less than 15% in Nevada. McDole and Fosberg (1974) found similar results in Idaho.

Moisture and Groundwater

The high specific heat of water reduces diurnal and seasonal soil temperature fluctuations (Oke, 1978; Marshall and Holmes, 1978). In Idaho Poorly drained soils showed relatively low MAST and seasonal temperature fluctuations when compared to well-drained sites at similar elevations (McDole and Fosberg, 1974). Schmidlin (1981) reported that naturally wet, poorly-drained soils from 15 sites in Nevada were 3°C cooler than well-drained sites in summer and 1°C cooler in winter. A comparison of irrigated and non-irrigated sites showed a difference of 5.6°C in MAST between bare soil and alfalfa covered plots. Part of the temperature difference was due to shading of the alfalfa. Maximum differences occur in summer months (up to 12°C) when irrigation is maximized. Leonard et al. (1971) found that irrigation waters increased soil temperatures at certain depths if there was a large initial difference between water and soil temperature. Little effect was found above a depth of 10 cm on an annual cycle although an extended period of high temperatures occurred below 10 cm due to relatively warm irrigation waters.

Cartwright (1968) found that the high specific heat of groundwater acts as an underground summer heat sink and winter heat source influencing soil temperatures. Aquifer thickness, transmissivity and thermal properties of the overburden determine the extent of surface

temperature influence of the groundwater. Groundwater recharge and discharge areas exhibit diagnostic temperature characteristics. In summer, recharge areas are relatively warm and discharge areas are relatively cold. Conditions are reversed during the winter.

Vegetation and Snow Cover

Vegetative cover acts to reflect and absorb incoming solar radiation and thereby reduces MAST. Munn et al. (1978) found that MAST declined moving from meadows through ecotone to forest sites in Montana. Annual soil temperature fluctuations also decreased. Differences in soil temperature between the three different vegetative cover types were greatest in summer because of uniform snow cover in winter.

Snow cover affects MAST and annual temperature fluctuations by acting as an insulator which preserves heat which otherwise would be lost to the atmosphere. MAST under snow covered sites are generally higher than bare soil areas (Rieger et al., 1973). Snow cover also has been found to reduce annual soil temperature fluctuations (Gray, 1968; Mueller, 1970).

Soil Temperature Regime Classification

The Soil Survey (Soil Survey Staff, 1975) has recognized the importance of soil temperature and has developed classification criteria which group soils according to their mean annual soil temperatures (MAST). These categories are used at the family level of Soil Taxonomy and are as follows:

Soil Temperature Regime	MAST
Pergellic	$\leq$ 0°C
*Frigid/Cryic	0-8°C
Mesic	8-15°C
Thermic	15-22°C
Hyperthermic	$\geq$ 22°C

* Mineral soils with no O horizons that are not saturated with water during some part of the summer with mean summer temperature (June, July, August) at less than 15°C are classified as cryic. If the mean summer soil temperature is greater than 15°C, then the soil is classified as frigid.

In Soil Taxonomy, secondary delineations separate soils based on annual temperature fluctuations. The prefix "iso" is added to a regime name if the difference between mean summer (June, July, August) and mean winter (December, January, February) soil temperature is less than 5°C.

Measurement of MAST

MAST can be accurately determined by measuring soil temperature at equally-spaced times throughout a yearly period at a level below the depth of diurnal temperature fluctuations, usually 50 cm (Smith, 1964). Carter and Ciolkosz (1980) found that at 25 cm and 50 cm depths averages of four equally-spaced measurements estimated MAST within 1°C. The average difference between MAST measured at 25 cm and 50 cm depths was 0.2°C. Weekly climatic fluctuations did not significantly affect MAST measured at 25 cm. Schmidlin (1981) found

similar results in Nevada for 101 sites. It was also found that two equally-spaced measurements at 50 cm estimated MAST within 1.0 to 1.3°C, depending upon the two months selected.

MAST can be determined with a single bore hole measurement if taken at a level below the depth of seasonal fluctuations. This depth is approximately 9 meters in the mid-latitudes (Smith et al., 1964). A simpler alternative is a single temperature measurement taken at a 9.0 - 18.0 meter depth in well water that has equilibrated with soil temperature. McDole and Fosberg (1974) compared MAST determined from monthly soil temperature readings taken at 0.6, 0.9, 1.2 and 1.5 meter depths with MAST measurements from well water in 75 cm increments from 6 to 9 meters. A total of 13 sites were sampled over a two-year period. Regardless of surface temperature at the time of sampling or the time of year, soil temperature profiles converged at a depth of 6 meters where they were within 1°C of the MAST derived from monthly soil temperature measurements taken at shallower depths.

Several least squares regression models have been developed equating MAST with geographic and topographic location. Carter and Ciolkosz (1980) developed MAST prediction equations based on latitude and elevation to determine the mesic/frigid boundary in the central Appalachians. Schmidlin (1981) regressed MAST against elevation, latitude and longitude for 96 sites distributed randomly throughout Nevada. Longitude was not significant indicating that MAST varies little in an east-west direction across Nevada. Standard errors of MAST estimates averaged 1.5°C.

Smith et al. (1964) indicate that MAST can be reasonably estimated by adding a constant of 1°C to the mean annual air temperature (MAAT) in much of the United States, but notes that the constant will vary depending on regional climate. Newhall (1980) prepared a MAST map of the U.S. using this technique on average MAAT for all 30 minute quadrangles. Carter and Ciolkosz (1980) found that MAST averaged 1.2°C higher than MAAT in the central Appalachians whereas Shmidlin (1981) determined that MAST averaged 3 to 6°C higher than MAAT in Nevada. Mueller (1970) determined that MAST varied up to 4°C less than MAAT in densely forested areas of the northern Rocky Mountains where more sparsely forested areas showed MAST 2.2°C higher than MAAT.

Soil temperature regimes are delineated by soil mappers in the field based on association with vegetative types in some regions where little temperature data exists (Lamars, 1982). This method is most useful when vegetative cover is climatically controlled and has not been recently disturbed.

Factors Affecting the Use of Thermal-Infrared Data for Surface Temperature Measurements

Remotely sensed thermal-infrared longwave radiation emitted or reflected from terrestrial surfaces is used extensively to measure temperature. Radiometers, which can be hand-held or mounted in aircraft or satellites, are sensitive to longwave radiation in the 8-14 micron range and are used for temperature measurements.

The energy flux (W) emitted from a blackbody is related to its surface temperature by:

$$W = \sigma T^4$$

(Oke, 1978)

where,

σ is the Stefan-Boltzmann constant, and

T is the object temperature in degrees Kelvin.

Terrestrial surfaces do not behave as blackbodies but, instead, absorb only a portion of the radiation incident upon them. The total outgoing longwave radiation from a surface can then be described as:

$$W = \varepsilon\sigma T^4 + (1 - \varepsilon)\ B^*$$

(Blad and Rosenberg, 1976)

where,

ε is the emissivity of the surface and,

B^* is the flux of longwave incoming sky radiation.

Longwave radiation measured by a radiometer is a combination of energy emitted as a function of surface temperature and emissivity and background sky radiation reflected from the surface. Atmospheric attenuation of radiation reduces the amount of outgoing longwave radiation reaching airborne and satellite mounted sensors. Therefore, knowledge of surface emissivity, background sky radiation and atmospheric attenuation are necessary to accurately measure terrestrial surface temperatures.

Emissivity

Emissivity or the "emitting ability" (Lillesand and Kiefer, 1979) of an object at a given temperature (T1) and wavelength (λ) is defined by the following relationship:

$$E(\lambda) = \frac{\text{Radiant Emittance from an Object at T1}}{\text{Radiant Emittance from a Blackbody at T1}}$$

Most radiometers focus on the 8-14 micron wavelength interval. At this interval, emissivity is relatively constant for given material types (Lillesand and Kiefer, 1979). Emissivity peaks on most materials at 9.7 microns.

Radiometers will underestimate surface temperatures if emissivity is falsely assumed to be 1.0. Emissivity varies with wavelength and must be known for the specific wavelength interval sensed by the radiometer (Taylor, 1979). Most terrestrial surfaces have emissivities between 0.8 and 0.99. Vegetated surfaces generally range in emissivity from 0.9 to 0.99 (Oke, 1978). Values have been measured for specific agricultural crops such as sorghum, soybean, millet (Heilman et al., 1976), cotton (Bartholic et al., 1972), alfalfa and corn (Blad and Rosenberg, 1976). Most soils have emissivities ranging from 0.9 to 0.98. Desert soils are generally low, ranging from 0.84 to 0.90 (Oke, 1978).

Emissivity varies as a function of material type. Compositional mapping of geologic materials is possible since soils, minerals and rock exhibit characteristic emittance curves in the 8-14 micron interval (Vincent, 1975; Buettner and Kern, 1965). Silicate rocks

exhibit diagnostic emittance minima at discrete wavelengths due to interatomic oscillations which can be used for discrimination purposes (Vincent, 1975). Silicate rich soils show low emissivities in the 8-14 micron wavelength interval, with most silicate influence occurring near 10 microns (Watson, 1975). Buettner and Kern (1965) indicated that emissivities of silicate containing surfaces are generally below 0.95. Taylor (1979) found that soils high in quartz appeared to be 5-6°C cooler than organic soils of identical true temperature when measured with a radiometer due to emissivity differences.

Emissivity increases with increasing moisture content. Emissivity progressively decreased from 0.94 at a volumetric moisture content of 8.4% to 0.88 at a moisture content of 0.7% for a plainfield sand in the 8-13 micron interval (Fuchs and Tanner, 1968). Buettner and Kern (1968) measured emissivity of 0.936 for a wet coarse quartz sand and 0.916 for the same sand when dry. Fuchs and Tanner (1968) showed that emissivity varies on a diurnal cycle due to slight surface moisture changes associated with condensation at night and evaporation during the day.

Fuchs and Tanner (1968) found that emissivity is a surface phenomenon independent of subsurface soil characteristics. When a thin dry sand layer covered the surface of soils differing in moisture content emissivity was constant regardless of the moisture content below the surface.

Temperature fluctuations commonly experienced by terrestrial surfaces result in emissivity fluctuations (Watson, 1975). Buettner

and Kern (1975) found a small dependence on temperature of emissivity for several rock types. Quartz (agate) varied from 0.694 at 253°K to 0.664 at 313°K.

Numerous field methods to measure emissivity have been developed (Lorenz, 1966; Buettner and Kern, 1965; Bartholic et al., 1972). Applications using satellite acquired data over large geographic areas generally use estimates of emissivity based on knowledge of surface characteristics.

Longwave Sky Radiation

Kirchoff's Law states that longwave radiation absorbed by a surface equals that which is emitted, at a given wavelength (Oke, 1979; Campbell, 1977). Therefore, the $(1-\varepsilon)B^*$ term in the previously discussed outgoing longwave radiation equation is the portion of longwave sky radiation that is sensed by a radiometer.

Lorenz (1966) comprehensively discusses the effects of sky radiation on temperatures measured by radiometers over surfaces varying in emissivity. Sky radiation is most significant when dealing with surfaces that have low emissivities which reflect a greater portion of the incoming sky radiation causing radiometers to overestimate surface temperatures.

Sky radiation flux varies depending on atmospheric temperature and atmospheric emissivity. Fuchs and Tanner (1966) estimated errors in temperature measurements of 0.4°C on clear days and 0.6°C on hazy days. Conaway and Van Bavel (1967) estimated errors of 1.0°C for soils with high emissivities of 0.98 and attributed the cause to localized air pollution which increased atmospheric emissivity. Fuchs

and Tanner (1966), Soer (1980) and Conaway and Van Bavel (1967) discuss methods for measurement and estimation of incoming sky radiation.

Atmospheric Attenuation

Atmospheric attenuation of longwave outgoing surface radiation by water vapor, gases and aerosols is discussed by Oke (1978). Minimum interference occurs in a 10-12 micron "atmospheric window" for outgoing longwave radiation. Within the window, the primary absorbing agent in a clear atmosphere is water vapor (Platt and Troup, 1973; Cogan and Willand, 1976). Byrne et al., (1979) found that errors in temperatures measured by radiometers of up to 3°C could be attributed to water vapor under clear sky conditions. Platt and Troup (1973) stated that carbon dioxide accounted for 3.0% of the total absorption of terrestrial outgoing longwave radiation and found that radiometric measurements from aircraft underestimated sea surface temperatures by 2.6'C above the tradewind inversion. Atmospheric attenuation above the inversion caused temperatures measured on board the Nimbus satellite to be 0.4°C less than the aircraft measurements. Lorenz (1966) stated that atmospheric attenuation of outgoing longwave radiation is negligible within 100 meters of the target. Stowe and Fleming (1980) and Egan and Shaw (1981) discuss the minor effects of aerosols on atmospheric attenuation.

Several techniques have been used to account for atmospheric attenuation. Atmospheric modelling techniques using radiosonde data are discussed by Cogan and Willand (1976) and Weis (1971). Dozier (1981) describes another technique where dual thermal channels in

different wavelengths can be used to correct radiometric temperatures for atmospheric attenuation. Heilman and Moore (1981) corrected radiometric temperatures using ground-measured temperatures of large water bodies recorded at the time of satellite overpass.

Vegetative Cover

Measurement of soil surface temperature is further complicated by vegetative cover. Temperatures sensed by radiometric scanners will be related to ground temperature, plant temperature and relative ground cover (Byrne et al., 1979). Fuchs and Tanner (1968) state that the emissivity of a single leaf is not representative of vegetative cover because of the multiple reflections that cover generates and they conclude that emissivity must be determined in situ. Hatfield (1979), Byrne et al. (1979) and Sutherland and Bartholic (1977) further discuss theory and problems associated with composite heterogeneous surface cover. Heilman and Moore (1980) developed empirical equations to estimate soil surface temperatures under crop canopies from radiometrically measured canopy temperatures. In their studies surface temperatures were expo ntially related to percent vegetative cover.

Applications Using Remotely Sensed Thermal-Infrared Data

Remote sensing has been used extensively to gather surface temperature data over large geographic regions quickly and repeatedly. Applications have used surface temperatures gathered from a single date or from multiple dates.

Bartholic et al. (1972) measured canopy temperatures using aerial thermal scanners in the 8-14 micron wavelength interval to map differences in water stress in cotton. In this study, plant canopy temperature differences up to 6°C were recorded between extreme cases. Millard et al. (1978) found that radiometrically measured wheat canopy temperatures measured half past solar noon correlated well with pre-sunrise plant water tension, a parameter directly related to plant growth and development. These results suggested the potential use of this method in irrigation scheduling and crop yield predictions. In addition, Millard et al. (1978) used canopy temperatures to calculate "stress degree days" (Idso et al., 1975) for calculating crop water requirements. Thermal-infrared thermometry also has been used to delineate plants suffering from disease stress (Pinter et al., 1979).

Numerous investigators have calculated evapotranspiration from crop canopy temperatures using remotely sensed thermal-infrared data (Bartholic et al., 1972; Heilman et al., 1976; Soer, 1980; Carlson et al., 1981). Many techniques reported involve predictive models based on energy balance processing at the boundary layer. Idso et al., (1977) measured evaporation from bare soil.

Remotely sensed thermal-infrared data has been used in soil moisture and hydrologic investigations. Idso et al. (1975) found that the thermal inertia concept could be useful for determining near surface soil moisture using diurnal surface temperature measurements. Diurnal temperature differences of Avondale loam correlated highly with soil water content. However, the relationship was dependent on soil type. Reginato et al. (1975) and Schmugge (1978) reported

similar findings. Carlson and Boland (1978) developed a mathematical atmospheric boundary layer model simulating surface energy processes to predict soil moisture content that is independent of soil type. The model was used with diurnal thermal-infrared data from the Heat Capacity Mapping Mission (HCMM) satellite to predict surface moisture heat flux and thermal inertia over a watershed (Kocin, 1979) and an urban area (Dodd, 1979). Heilman and Moore (1982) found that HCMM thermal-infrared canopy temperatures did not correlate directly with surface moisture. Canopy temperatures and percent cover were used to estimate soil surface temperatures using empirical relationships. These surface temperature estimates correlated high with soil moisture.

Cartwright (1968) used aircraft thermal-infrared data to measure surface temperatures of glacial till, alluvium and other unconsolidated deposits for groundwater exploration. The high specific heat of water acts as an underground heat sink during summer and a heat source during winter dampening surface temperature fluctuations. Myers and Moore (1974) detected shallow aquifers using thermal-infrared aircaft data in glacial deposits. Aquifers less than 30 meters below the surface (to aquifer bottom) and 2-25 meters thick were detected in South Dakota. Diurnal and annual temperature fluctuations, thermal conductivity of the flow media, variations in groundwater flux and spatial variation in groundwater temperature all combine to influence surface temperatures. Huntley (1977) used multi-temporal diurnal surface temperature measurements to estimate changes in groundwater depth. Other applications of thermal-infrared data in groundwater

hydrology include mapping of recharge and discharge areas (Worcester et al., 1979), geothermal areas (McLerran and Morgan, 1961), gaining and losing streams (Harvey et al., 1977), spring location (Whiting, 1976) and bank seepage (Thompson, 1977).

Vincent (1975) discusses the use of thermal-infrared multispectral scanner data for discrimination of geologic materials. He reports that compositional mapping of silicate rock is especially promising because of emittance minima diagnostically characteristic of different silicates. Watson (1975) comprehensively reviewed thermal inertia mapping of geologic materials and reported that thermal inertia correlates almost linearly with densities of most dry rocks. Minerals and rocks high in silica (quartz, rhyolite, granite) have relatively higher thermal inertias than expected based on density alone. The opposite is true for materials such as olivine, basalt and gabbro which are low in silica and have relatively low thermal inertias. Thermal inertia mapping is primarily confined to arid and semi-arid regions with good geologic exposure. Numerous thermal inertia models have been discussed in the literature (Price, 1980; Kahle et al., 1976; Rosema, 1978; Carlson et al., 1981; Pratt and Ellyett, 1979).

Schneider et al. (1979) discuss the use of thermal-infrared data in geomorphological applications. Nighttime imagery was used to map drainage patterns and landforms in North and South Dakota. Delineated features included escarpments and recessional moraines. North-facing slopes were 1.5°C warmer than south-facing slopes. Vincent et al. (1981) suggest that HCMM thermal-infrared data may be useful for mapping soil infiltration rates in Michigan.

Combinations of Remotely Sensed Data

Many combinations of digital data sets involve the use of multi-temporal data of the same type. Turner (1979) used anniversary Landsat data from two consecutive years to differentiate gypsy moth defoliated forest from areas not defoliated but with similar spectral signatures (e.g., near bare soil). Anomalies such as forested areas cleared between dates remain a problem. Mimms (1982) digitally combined two Landsat data sets collected at times corresponding to maximum and minimum vegetative cove in east-central Utah. Channel ratios and principal components from the combined data set were evaluated as potential aids to soil mapping. Enhancements from the combined data set were judged to be superior products for soil mapping compared to enhancements from either of the individual Landsat data sets. Schrier (1982) performed principal components analysis on two separate Landsat data sets prior to digital combination in order to determine which of the original channels contributed most to the total variance. Band 5 and Band 7 were found to contain the most useful and independent information from both data sets and were digitally combined. The resulting data set contained the majority of the original information of the two data sets but with half of the data, therefore, improving processing efficiency. Cluster analysis was performed on the reuslting data set to map terrain mobility for rescue efforts in northern Canada. Eyton (1983) described techniques for multi-temporal analysis of digital data sets using photographic color composites. Data sets from three dates were assigned subtractive

primary colors and when overlaid produced composites showing different colors where change occurred and gray tones where no change occurred.

Hutchinson (1982) evaluated techniques for combining ancillary data such as Digital Terrain Elevation (DTE) with Landsat data. Each technique for classification improvement had advantages unique to particular situations that would determine choice. DTE data was found to be useful in numerical models to display landform relief patterns. Algorithms based on four-color hillshading can produce colorful and realistic relief maps (Dutton, 1982). Hendersen and Digloria (1982) evaluated DTE data for soil mapping applications and concluded that DTE data are accurate but expensive. In addition, slope class and aspect maps generated from DTE data were found to provide useful interpretative information for production soil mapping. Stone and Estes (1981) found that DTE data may provide information useful for county-level landcover classification procedures.

Turner (1979) combined Landsat and DTE data to augment spectral data with topographic data to improve classification of gypsy moth defoliation in Pennsylvania. DTE eliminated all indications of defoliation on lower slopes and valley bottoms since defoliation occurred almost entirely on upper slopes. Turner concluded that it would be easier to spatially register both data sets through a common base map rather than directly to each other because of the difficulty in locating common control points. Justice and Wharton (1980) used DTE to quantify and reduce topographic effects on Landsat data. Williams and Ingram (1981) found that aspect channels produced from DTE data did little to reduce confusion between spatially similar forest canopy conditions.

Eyton (1979) combined multi-temporal radar and Landsat data for crop classification in Eudora, Kansas. Radar data significantly improved classification especially in the early part of the growing season. Crop classification using combined data sets showed improvement over either of the individual data types.

Landsat, aeromagnet and DTE data were combined in New Mexico for geologic mapping studies (Fischer et al., 1978). In the study, high intensity magnetic anomalies associated with near surface magnetic bodies were delineated in playas. Overlay with Landsat data showed that the alignment of the playas corresponded to regional tectonic trends.

Lougeay (1982) found that thermal data obtained from Landsat-3 contained topographic texture information lacking in visible and near-infrared Landsat bands. The thermal-infrared data were useful in alpine areas with much surface relief and homogeneous covers where reflectance is high, thereby saturating solar sensitive detectors (e.g., snow).

Price (1981) assessed the contribution of Landsat-3 thermal data for general land use classification in New York state. Price concluded that thermal data is dependent upon surface factors such as slope, altitude, and surface energy balances which may not influence the spectral behavior of reflectance channels. Because of the varying physical properties of thermal data, its usefulness is subject to ambiguities and potential errors.

Heat Capacity Mapping Mission (HCMM) thermal-infrared data have been combined with Landsat data. The multi-channel data set can be used for surface temperature measurements and associates land use and topographic information (Commission of the European Communities Joint Research Centre, 1980).

PART I

Introduction

Temperature is an important soil property that largely controls agricultural productivity and genetic soil development. Biological, chemical and physical processes affecting seed germination, seedling mortality, plant growth rates, root growth and species adaptability are influenced by soil temperature (Richards, et al., 1962). Each plant species has individual temperature requirements. Some Antarctic microscopic plants grow only at temperatures below 7°C, while some tropical plant seeds need temperatures above 24°C to germinate (Smith, 1964). Synthesis and decomposition of organic substances and activity of microorganisms and the entire soil fauna depends on soil temperature. The geographic distribution of soils is controlled by temperature (Shul'gin, 1965).

Soils are classified into temperature regimes based on their respective mean annual soil temperatures (MAST) and are field-mapped as part of the National Cooperative Soil Survey (Soil Survey Staff, 1975). Temperature regime boundaries coincide with vegetational boundaries. For example, the limits between the Cotton Belt and the Corn Belt, and the Cotton Belt and the Winter Wheat Belt correspond with soil temperature regime boundaries (Smith, 1982).

Direct measurements of MAST are impractical for routine soil field-mapping so several methods are used to estimate MAST. A constant added to mean annual air temperature closely approximates MAST within local geographic areas (Smith, 1964). Empirical models

(Schmidlin, 1982; Carter and Ciolkosz, 1980) predict MAST based primarily on elevation and latitude. Others infer MAST from vegetative cover (Lammars, 1982).

The Heat Capacity Mapping Mission (HCMM) satellite offers a unique opportunity to measure surface temperatures repeatedly over both diurnal and annual cycles. Soil surface temperatures indicate physical, chemical and biological properties of a soil. Remotely sensed surface temperature can be used to estimate soil thermal inertia and moisture content (Carlson and Boland, 1978; Kale, 1976) as well as depth to shallow groundwater (Heilman and Moore, 1982).

Objectives

The specific objectives of this study are to:

1) measure apparent soil surface temperatures in desert areas and evaluate relationships between surface temperature variability and surface physiography using HCMM thermal-infrared data;
2) digitally overlay and cartographically correct multi-temporal HCMM data sets;
3) evaluate the feasibility of using HCMM and ancillary data to measure soil surface and plant canopy temperatures and to thereby delineate and map soils into their respective soil temperature regimes.

Study Site

The study site is located in Grand and San Juan Counties in east-central Utah (Figure 1). The area lies within 38°20' - 39°07' north latitude and 109°10' - 110°05' west longitude and consists

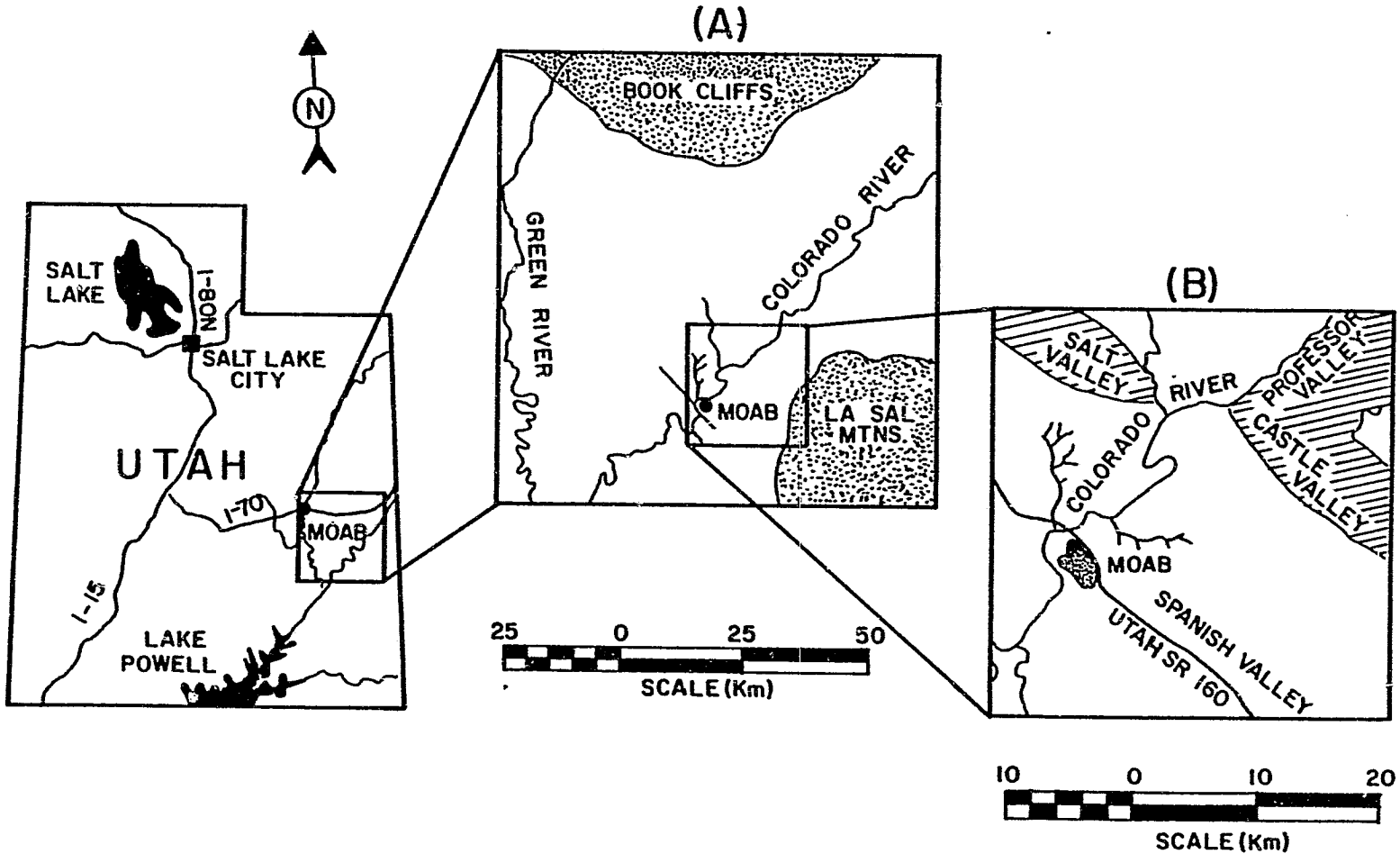

Figure 1. Location map of Utah study sites — (A) Part I study site and (B) Part II study site

of 925,400 hectares (2,287,000 acres). The site is bounded by the Book Cliffs to the north and the La Sal Mountains to the southeast (Figure 2). The Green River forms a western boundary and joins the Colorado River which flows southwesterly across the area. The town of Moab, Utah, is near the center of the study area. Plate 1 shows detailed features described throughout this report.

Geology and Topography

The study site lies in the Canyonlands Section of the Colorado Plateau Physiographic Province, which covers almost the entire eastern half of Utah. Approximately horizontal bedrock, generally high elevations, and numerous deep, rugged canyons characterize the province. Active erosion along steep edges of plateaus create retreating escarpments. Elevations range from 1180 meters in Moab to over 3810 meters at the summit of Mt. Peale in the La Sal Mountains with most areas lying between 1220 and 1830 meters (Plate 1).

The general physiographic structure consists of broad, flat parallel folds of sandstone and shale of primarily Tertiary, Cretaceous, Juriassic and Triassic age. Shale deposits are confined to a fringe at the base of the Book Cliffs. Folds are oriented northwestward and dip less than ten degrees. A stepwise succession of plateaus mantled with glacial till rises southeastward toward the La Sal Mountains where bedrock dips radially outward at angles of 10-15 degrees (Figure 3). The mountains are underlain by resistant igneous rock which have intruded into Triassic and Juriassic sandstones. Quaternary alluvial and eolian deposits cover valley floors which encircle the La Sal Mountains and the Book Cliffs.

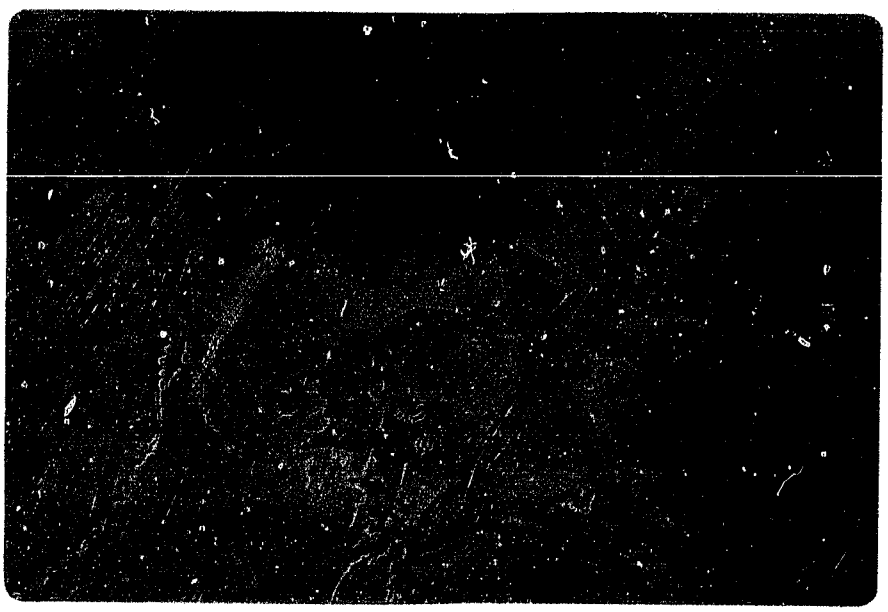

Figure 2. Landsat color composite of Part I study area and vicinity

Figure 3. Landscape view looking east across dissected red sandstone plateaus towards the La Sal Mountains from Arches National Park

The deeply incised Colorado River flows southwest to join the Green River which flows along the western border of the study site. Accelerated erosion near the confluence of the two rivers, has widened the canyons considerably producing scenic areas such as Canyonlands National Park.

Several unique "salt valleys" (Fisher Valley, Castle Valley, Salt Valley, Spanish Valley) have dropped grabben floors that formed when anticlinal arches were broken by faults normal to the folds. Theories suggest that thick Paradox Basin salt deposits beneath each valley were subjected to extreme pressures from overlying sedimentary deposits. The pressure from the overlying sediments forced salts to flow out from beneath the grabben floors. Salt flow was enhanced as water from deeply incising rivers dissolved the thick deposits upon contact. Salt movement left voids which promoted further settling. A distinct salt plug occurs in Castle Valley (Richmond, 1962).

The Colorado River enters Spanish Valley through a large portal with walls 300 meters in height and flows perpendicular across the grabben valley floor and exits through another large portal. The crossing of major axes of folds and grabbens indicate superposition of the Colorado River from ancestral material long since removed (Richmond 1962). Quaternary deposits of alluvial and eolian deposits mantle the Salt Valley floors. Recent alluvium occurs along the Colorado with eolian deposits filling pockets in surrounding plateaus.

The lacolithic La Sal Mountains are divided into three major groups of peaks called the north, middle and south mountain groups. Each is surrounded by a series of steep segmented hogbacks of

sandstone rock separated by troughs of less resistant shale. Summit uplands are commonly covered with blocky residual or colluvial material although bedrock nears the surface in some locations. Extensive alpine glacial activity carved numerous characteristic landforms. High peaks contain cirques, hanging valleys, moraines and rock glaciers (Figure 4). Youthful steep-walled valleys dissect the La Sal Mountains.

Climate

Topographic diversity within the study site produces considerable local climatic variability, primarily related to elevation. Three major climatic zones can be distinguished. Canyons and plateaus bordering the Colorado are arid with mean annual precipitation less than 22 cm. Higher plateaus and mountain foothills are semi-arid and have a mean annual precipitation between 22-38 cm. Higher mountainous regions in the La Sal Mountains are dry-sub humid with mean annual precipitation between 22-63 cm.

Precipitation

Generally, there are three types of storm systems responsible for precipitation in Utah (Wilson et al., 1975). They are: 1) winter storm fronts moving from the west or northwest during October through May, 2) cold lows which form during October and late April through May that drift across Utah producing gentle rains and snow, and 3) summer thunderstorms resulting from moist air flow from the Gulf of Mexico. The La Sal Mountains act as a barrier to moist southeasterly air masses creating a rainshadow over the study site. Therefore, the western side of the La Sals is drier than the eastern side.

Figure 4. Landscape view of Mt. Peale in the La Sal Mountains showing a cirque and hanging valley formed by alpine glaciers.

Precipitation records show wide variability in monthly accumulations in any particular year, although average monthly accumulations show much less variability. This is primarily due to the sporadic mode of precipitation associated with summer thunderstorms. The range in average monthly precipitation is less than 2.5 cm with June being the driest month.

The rainy season occurs from July through October, although average monthly precipitation during this period is generally less than 2.5 cm. The dry period occurs generally from May to late July.

Wide variation in monthly precipitation due to summer thunderstorms results in flash flooding in sparsely vegetated low-lying areas and canyons resulting in rapid erosion. Large wash areas formed in Mancos shale deposits are located near the base of the Book Cliffs and extend across the entire study site. Vegetation in the mountains reduces flooding and surficial deposits absorb most of the precipitation with gulleys occurring only on steep local slopes. Occasional rains of one to two days duration may occur in the mountains during severe storms. Overcast conditions on the high plateaus and mountains often accompany these storms.

The snowy season occurs from September through March with greatest accumulations in December and January in the canyons and low plateaus. Snow continues into March in the high plateau and mountains. Average annual snowfall at Moab is 15 cm. Rapid melting occurs within a few hours to a few days after each snowfall. Average annual snowfall at La Sal is 147 cm. Snow cover may last for several

continuous weeks. High mountain basins may receive over three meters of snow and remain snow-covered throughout the summer in sheltered locations.

Temperature

Elevation, latitude and local topography combine to influence air temperatures. Mean annual air temperature ranges between 10-15°C in canyons and low plateaus. Fringing foothills and high plateaus have mean annual air temperatures between 5-10°C while high mountain regions have mean annual air temperatures of -1 to 5°C.

The mean annual air temperature varies with latitude at similar elevations. Utah lies within 37° and 42° north latitude with the southern region being approximately 5°C warmer than northern parts of the state (Wilson, et al., 1975). Within the study site, Moab (1190 meters, 38° 36' N. Lat.) is 2.7° C warmer than Green River (1240 meters, 39° 00' N. Lat.).

Temperature inversions occur in most valleys during winter months. During the night, cool air flows down valley slopes and collects on basin floors due to temperature differences created by daytime surface heating. The surface of the inversion occurs generally 150-450 meters above the basin or valley floor. Temperature differences between the top and bottom of the inversion average 5-10°C during the winter (Wilson et al., 1975).

Cold air drainage into valleys greatly affects agricultural management. Freeze-free seasons average between 160-180 days near the top of the inversion and only 80-90 days in the valley bottoms.

Generally, the freeze-free season decreases by 20 days for each 300 meters of elevation above the inversion in the southern portion of the state (Wilson et al., 1975).

Temperature inversions, as well as low surface moisture contribute to extreme diurnal temperature variations common to semi-arid areas. Diurnal air temperature fluctuations at Moab, typical of low-lying areas, are commonly 22°C and occasionally exceed 33°C (Richmond, 1962). Summer daytime temperatures often exceed 37°C at Moab with a record of 44°C. Corresponding nighttime temperatures may drop to 4°C. Winter daytime temperatures are as high as 15°C and may drop below freezing for several consecutive nights.

Diurnal temperature fluctuations diminish in high plateaus and mountains due to increased vegetation and moisture. Maximum and minimum temperatures drop progressively with increasing elevations. Summer temperature maximums in the mountains generally fall below 21°C while nighttime temperatures rarely fall below freezing. Seasonal fluctuations are about equal to those at lower elevations.

Winds

Average wind speeds range between 11-19 kph in lower valleys, and increase with elevation to 24-32 kph near the tops of the mountains. Active cold fronts or thunderstorms occasionally produce preceding wind gusts exceeding 145 kph (Wilson et al., 1975). Silt particles are lifted hundreds of meters into the air in Spanish Valley and, at times, color the snow red in the high basins. Regional wind direction near the surface is generally northeasterly. Orientation of major valleys tend to channel the wind.

Vegetation

Elevational changes of over 2700 meters from the desert canyons (1200 meters) to the peaks of the La Sal Mountains (3900 meters) produce distinct zonal vegetational bands largely related to temperature and altitude. Climatic effects of aspect produce fluctuating boundaries (Figure 5). Extensive information on the physiography of the La Sal Mountains and bordering desert and plateau is thoroughly presented by Richmond (1975) and is the source of most of the material to follow.

Two major ecological zones comprise the area. They are: 1) the Rocky Mountain Forest Complex, and 2) the Great Basin Desert Ecological Formation. The Rocky Mountain Forest Complex is further subdivided by decreasing elevation into: a) the alpine zone, b) the subalpine zone, 3) the montane zone, and d) the foothills zone. Transition zones generally mark the indiscrete boundaries of each vegetative belt which may vary up to 300 meters in elevation depending on aspect.

The alpine zone or alpine tundra association occurs above the timberline at 3350 meters on north facing slopes and 3500 meters on warmer south facing slopes. The surfaces of these often steep slopes are covered with barren rock fragments, frost-rubble and rock glaciers. Characteristic species of several tundra associations are found, such as cushion plants, cinquefoils, and various sedges and grasses. The absence of Dryas and Salix, common to alpine tundra of the Rocky Mountains, indicates a more arid climate.

The subalpine zone extends from the timberline down to 3500 meters on south facing slopes and to 2440 meters on north facing slopes. This zone has been called the spruce-fir belt, Subalpine

Figure 5. Typical vegetation sequence in the La Sal Mountains. Landscape view of the La Sal Mountains showing a climatically controlled vegetational sequence associated with aspect and elevational differences.

Forest and Hudsonian Life Zone (Elmore, 1976). Thick shrub of Englemann's spruce climax with less abundant subalpine fir. Some Douglas-fir is intermixed at lower levels. Vegetation is gnarled and twisted at the upper levels of the zone.

The Montane zone, sometimes called the Canadian Life Zone, extends down to 3290 meters on south slopes and to 2072 meters on north slopes in distinct tongues. The typical climax forest of Douglas-fir and ponderosa pine found throughout the Rocky Mountains is replaced by belts of thick stands of aspen separated by meadows of grasses and herbs. Aspen is normally subclimax in the Montane zone but the breadth and abundance around the La Sal Mountains suggest climatic control (Richmond, 1962).

The Foothills zone is further divided into four zones. They are the: 1) scrub-oak, mountain mahogany climax, 2) ponderosa pine climax, 3) pinyon-juniper climax, and 4) sagebrush-grass climax and are ordered from high to low elevations. The scrub-oak, mountain mahogany climax zone is characterized by thick stands of gambel oak intermixed with brush and grasses.

Ponderosa pine occurs only on the eastern slope of the La Sal Mountains due to increased rainfall. The scrub-oak/mountain mahogany and ponderosa pine belts are commonly combined and called the Transition Life Zone roughly extending from 1980 to 2750 meters depending on aspect.

The pinyon-juniper belt or Upper Sonoran Zone ranges from 1675 to 2600 meters on south slope and 1525 to 2280 meters on north slopes. A transition from mixed stands of pinyon and juniper towards mostly

juniper occurs towards lower elevations. Plateaus, mesas, alluvial fans and cuestas are landforms common to this belt.

The sagebrush-grass climax occurs below the pinyon-juniper belt and occurs primarily in pockets of eolian deposits. It lacks plants associated with saline soils.

The Great Basin Desert Ecological Formation ranges from 1200 to 2100 meters and makes up the majority of the site. Sagebrush less than one meter in height with sparse intermixed grass is common. Blackbrush is found in more arid climates such as Castle Valley, Salt Valley and the Canyonlands. Cottonwoods and willows are found along floodplains and intermittent streams in deep, narrow canyons. On low terraces where alluvium contains salts such as gypsum, sagebrush is often replaced by greasewood or by shadscale. Description of species common to the site are discussed by Richmond (1962) and Elmore (1975).

Soils

Extensive topographic variability across the study site controls localized soil temperature and moisture characteristics. Most soils have mesic mean annual soil temperatures (MAST) with transition to frigid, cryic and pergellic regimes towards higher elevations. Thermic temperatures occur in drier soils on canyon and valley floors generally below 1370 meters. Soil temperatures are influenced by large aspect differences found on steep (north and south-facing) canyon walls. The influence of aspect on soil temperature is illustrated by 300-450 meters differences in vegetational zone boundaries on north and south-facing slopes.

Most soils are classified into the Aridic soil moisture regime with some Xeric, Udic and Ustic soils found at higher elevations. Low-lying areas generally receive less than 25 cm of precipitation per year. Deep sandy deposits retain little available water at shallow depths. General soils maps and soil descriptions were provided by the Soil Conservation Service for the area and are found in Appendix B.

Soil parent material is predominantly residual, colluvial, eolian and alluvial deposits formed from sandstone and shale. Soils formed in shale are confined mainly to a region located at the base of the Book Cliffs north of Salt Valley where the soft highly erodable Mancos shale forms extensively dissected washes. Deep alluvial deposits of sandstone and some shale line valley floors. Eolian deposits of sandstone and shale material form deep pockets throughout the area wherever protection from wind is provided. Rock outcrops are extensive, especially along actively eroding escarpments of mesas and benches. Deep glacial till, outwash deposits and frost rubble formed from diorite are remnants of past glacial activity.

Most soils are classified into the Entisol soil order and show minimal profile development. Soils range from shallow to deep and are well-drained. Low precipitation, low vegetative cover, steep slopes and windy conditions combine to minimize profile development. Extensive areas classified as Aridisols are formed in the soft Mancos shale. Transitions toward higher moisture and lower temperatures in the mountains and high plateaus create deep Mollisols under thick aspen forest cover. Some Alfisols are also found in these areas.

The minerology of these soils is classified primarily as mixed, although some Mollisols are montmorillonitic and calcareous. Some arid soils also have petrocalcic horizons.

HCMM Satellite and Data Characteristics

The Heat Capacity Mapping Mission (HCMM) was the first of a series of Application Explorer Missions involving the placement of satellites in special orbits designed to collect unique types of surface information. Project motivation stemmed from feasibility studies attempting to measure thermal inertia (the ability of a material to resist temperature change) by using thermal-infrared data to measure maximum and minimum diurnal surface temperatures.

The satellite was launched 26 April 1978 by a Scout launch vehicle into a sun-synchronous circular orbit inclined 97.6° retrograde to the equator and collected data for over two years. The satellite's original altitude of 620 km was lowered to 540 km on 21 February 1980.

The sun-synchronous orbit allowed coverage of the entire Earth's surface between 85° north and south latitudes every 16 days. The entire area received diurnal (approximately 12 hours) coverage with the exception of areas between 15 and 35 degrees latitude (north and south). There, only 36 hour coverage was possible. The nominal ascending equatorial cossing time of 2:00 PM produced north middle latitude (40 degrees) crossing times of 1:30 PM and 2:30 AM.

The HCMM satellite contained a Heat Capacity Mapping Radiometer (HCMR) that was a modified Surface Composition Mapping Radiometer (SCMR) flown on Nimbus 5. The spacecraft contained two distinct

modules. An instrument module contained the HCMR assembly and a base module contained data handling power, communications command and altitude control systems.

The HCMR two-channel radiometer collected both visible/near-infrared (0.45-1.1 micrometers) and thermal-infrared (10.5-12.5 micrometers) data. The visible/near-infrared band corresponded to a broadband equivalent of the Landsat MSS and had a nominal pixel resolution of 500 x 500 km at a 620 km altitude. The thermal-infrared band had a nominal pixel resolution of 600 x 600 meter at a 620 km altitude with a Noise Equivalent Temperature Difference (NETD) of 0.3° Kelvin at 280° Kelvin. The useable range was from 260° to 340° Kelvin.

Data processing by NASA produced a resolution of 481.5 meters with square pixels. Registration between bands was within 0.2 pixels. Extensive satellite, radiometric and data processing information is contained in the HCMM User's Guide (NASA, 1980).

Each HCMM data set is available in either computer-compatible tape (CCT) digital format or black-and-white contrast-stretched positive and negative hardcopy and transparent film products. Single scenes within an orbit swath path or entire swaths are available in either raw format or registered to a Hotine Oblique Mercator (HOM) projection. Digital data is organized band sequentially with pixel values represented by 8-bit binary values scaled from 0-255.

Project Data

Three general types of data were used throughout this analysis consisting of digital HCMM data, photographic data and map data. The HCMM data consisted of the following five dates:

DATE	SCENE #2 NUMBER
12 MAY 78	AA0016-20370
16 AUG 78	AA0112-20260
19 OCT 78	AA0176-20190
13 JUL 79	AA0443-19490
4 SEP 79	AA0496-19140

Computer-compatible tapes (CCT) of HCMM three-channel digital data sets were obtained for each date. Thermal-infrared data plus daytime visible contained daytime and nighttime near-infrared data. Contrast-stretched imagery accompanied each digital image.

Black-and-white 1:24000 stereo-pairs were used for detailed terrain analysis and ground-truthing in some areas. Orthophotoquads (1:24000) were used in the same fashion.

Topographic maps (1:24000 and 1:250000) were used extensively for image interpretation and geographic reference (Plate 1). The 1:250000 map of the Moab quadrangle served as a base map for cartographic correction purposes. General soils maps (1:250000) of the Canyonlands and Grand County soil survey areas (Appendix B) covered the study site. A 1:250000 scale geologic map of southeastern Utah (Hintz and Stokes, 1964) provided sufficient detail for the region.

Procedure

Procedural Concepts

The basic concepts of the procedure used to estimate mean annual soil temperatures (MAST) and annual surface temperature amplitude (AMP) using HCMM data are graphically represented in Figure 6. The annual fluctuations of surface temperature approximate a sine curve symmetric about the mean annual soil temperature. The annual soil

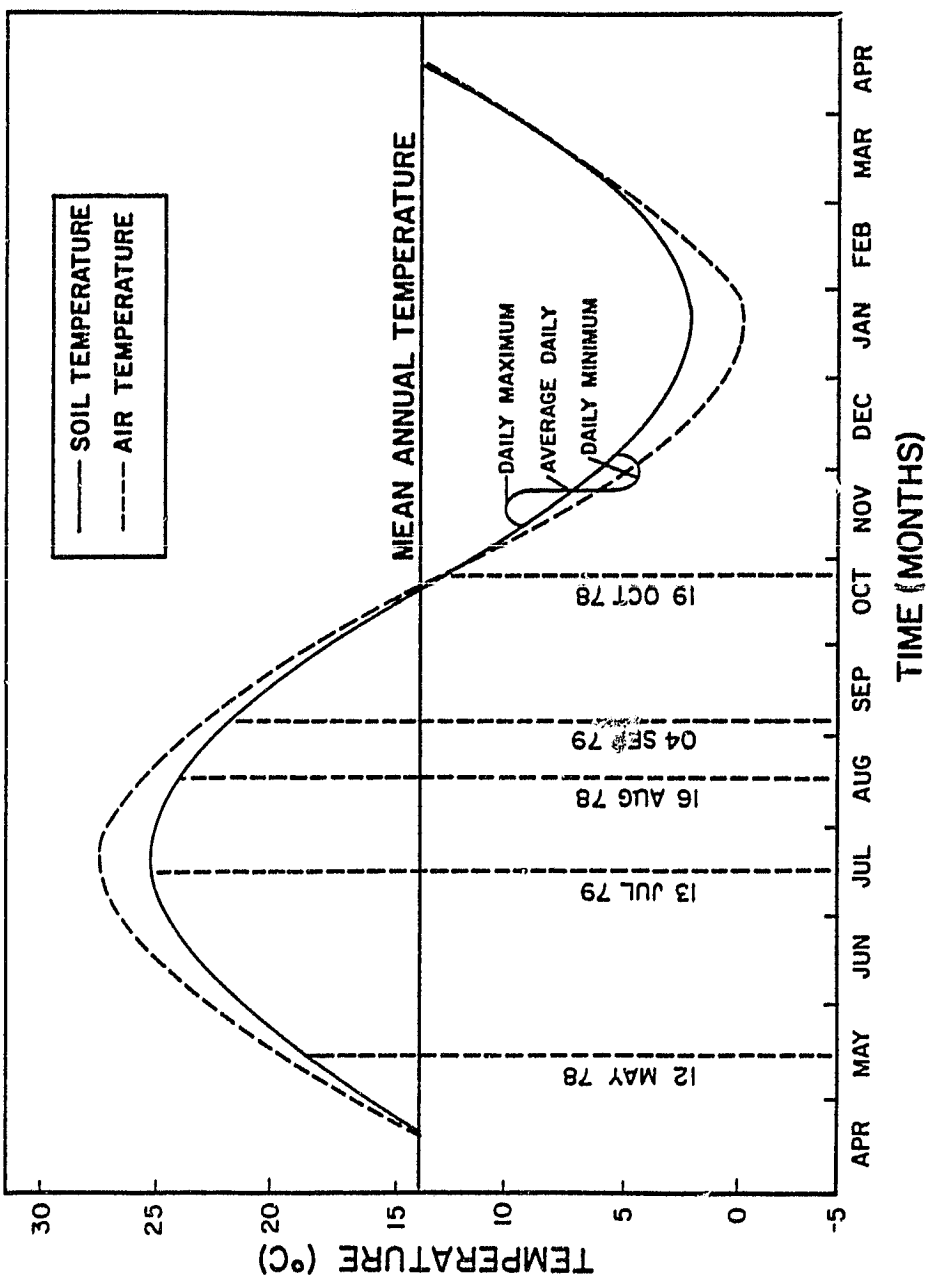

Figure 6. Theoretical soil surface and air temperature annual sine curves showing dates of HCMM data sets

temperature sine curve is in phase with the annual air temperature sine curve, although their amplitudes may be different. For any day throughout a yearly period, the corresponding temperature along the annual sine curve represents the average temperature for that particular day. Therefore, the annual sine curve does not represent diurnal temperature which also fluctuate about a daily mean.

HCMM multi-temporal surface temperature measurements provide the ability to "fit" an annual sine curve for a particular location. For a given date, HCMM daytime and nighttime temperatures correspond closely with times of maximum and minimum daily surface temperatures. Since daily temperatures fluctuate symmetrically about the daily average, HCMM daytime and nighttime temperatures can be averaged to estimate average daily temperatures.

The annual variability of average daily temperature can be determined by analyzing several HCMM data sets distributed throughout a yearly period. These multi-temporal average daily temperatures can be used to fit a sine curve describing annual surface temperature fluctuations. The annual sine curve can then be used to estimate MAST and AMP for a given location. Figure 6 shows the actual distribution of HCMM dates used in this study.

Data Pre-Processing

Data Selection

Five multi-temporal HCMM data sets obtained from NASA - GSF in Greenbelt, MD each consisted of computer-compatible tapes (CCT) and contrast-enhanced film positive hardcopy and transparent imagery.

Each data set contained daytime visible (DAY-VIS), daytime thermal-infrared (DAY-IR) and nighttime thermal-infrared (NIGHT-IR) channels in band sequential format. Binary grey-level values scaled from 0-255 represented each HCMM pixel. Each elongated data set contained an entire 8-12 minute overpass up to 3,000 km long with a 716 km swath width, thereby providing extensive aerial coverage. Spatial registration of the three channels for each date was performed by NASA prior to shipment.

Several criteria were established for the selection of quality data. The HCMM image catalog on microfiche narrowed the selection to overpass dates with diurnal coverage, ratings of "GOOD" radiometric quality and less than 30 percent cloud cover. Hardcopy square format film-positive imagery acquired for each scene insured minimal snow and cloud coverage over the study site and also located the site in reference to the edges of the swath path where radiometric and geometric quality of diurnal image rectification diminishes (NASA 1980).

Precipitation data (NOAA, 1978; NOAA, 1979) obtained from eight weather stations distributed throughout the study site insured that no significant periods of precipitation had occurred immediately prior to times of data collection. Evaporative cooling causes overall reduction in temperatures and diminishes spatial temperature variability. Temporary cooling of surface temperatures is conceptually a deviation from the theoretical sine curve describing the annual average surface temperature response.

Ideally, an even distribution throughout the year with numerous dates to adequately represent the cyclic phenomenon being estimated

was desired. However, only five dates met the criteria out of approximately 35 examined. The selected dates defined a six-month period from May to October primarily representing times of above average surface temperatures. Selection of less than ideal data was considered, but lengthy acquisition periods were too great for the project duration.

Study Site Subsetting

The ORSER software system (Turner et al., 1982), based on band-interleaved by line data formats, was used for bulk data processing. Data for the study site was selected frome ach HCMM band-sequential channel and reformatted to provide ORSER system compatibility and to eliminate costs associated with processing unnecessary data outside the study site. To achieve this, the SUBSET program, already capable of handling several data formats, was modified with the addition of a subroutine called HCMMOP. The new program was named SUBSET.HCMM and will be added to the ORSER library. SUBSET.HCMM accepts single channel HCMM data as input and outputs, as an ORSER format tape, a selected subset based on user supplied (scan line and element) coordinates. "Transition-within-image" HCMM data sets, where single channel data sequentially spans two tapes, was accommodated in single program runs.

DAY-VIS, DAY-IR and NIGHT-IR channels were subset onto separate ORSER format tapes for each of the five dates creating 15 separate data sets. The subsetted area contained the study site (200 x 200 pixels) plus bordering buffer zones necessary for future image registration, thereby enlarging the region to approximately 600 x 600

pixels. Measurements from hardcopy film positive imagery provided scan line and element coordinates.

Cartographic Correction

Remote sensing applications often require the overlay of digital image products onto a given map projection for geographic reference purposes or mutual spatial registration of several digital image products. Satellite altitude, attitude and sensor variability create complex spatial distortion within relatively small segments of a swath path.

To correct for such distortion, it is necesary to digitally stretch or transform an image such that it conforms spatially to a base image or map using an empirical technique known as "rubber-sheet stretching." The initial step involves production of contrast-stretched imagery to maximize contrast and enhance the appearance of control points. Histograms output by HISTRAN program are used to divide the frequency distribution of pixel values into equal frequency intervals or classes. Classes are assigned grey level values equally distributed from 0 (Black) to 255 (White) to maximize contrast between classes on grey level plots. Grey level plots are produced using the NMAPV program at a selected scale on the Versatec electrostatic plotter.

Control points, such as topographic breaks, bends in rivers, stream confluences and lakes, are identified on both the "original" and "corrected" space imagery. Matching control points are digitized and the coordinate pairs are stored in permanent disc files. Discrepancies between matching coordinate pairs for each control point provide the basis for determining the transformation model necessary

to accurately stretch the image in "original" space, such that it geometrically conforms to the image in "corrected" space. The transformation model consists of four least squares regression equations whose order depends on the complexity of the necessary stretch. The four equations are defined as:

F1 defines "original" space element coordinate (X) in terms of "corrected" space coordinates (CX,CY).

F2 defines "original" space scan line coordinates (Y) in terms of "corrected" space coordinates (CX,CY).

F3 defines "corrected" space element coordinates (CX) in terms of "original" space coordinates (X,Y).

F4 defines "corrected" space scan line coordinates (CY) in terms of "original" space coordinates (X,Y).

Therefore, F1 and F2 are functions defining "original" space coordinates in terms of "corrected" space, whereas F3 and F4 define "corrected" space coordinates in terms of "original" space.

Transformation models are developed using EZLS program (Myers, 1980) in the ORSER system or commonly available statistical regression programs with stepwise capabilities, such as SAS (Helwig, 1978). Several models of varying complexity and accuracy are developed for each set of control points. Residual errors at each control point and multiple correlation coefficients are used to determine statistical "fit" of the model.

Appropriate model selection also requires spatial analysis of the selected model. The WARP (Appendix C) program was written to allow preview of the spatial warp or stretch of the "original" space data set after transformation to "corrected" space. Coordinate pairs of

"original" space pixels defining a uniform sampling interval are converted to their locations in "corrected" space using functions F3 and F4. Pixel locations are connected with lines forming a graphical representation of the "warp" caused by the selected model. Output can be directed either to a Houston Instruments four-color plotter or a Versatec electrostatic plotter. Control points used to develop the model are plotted as well. Preview of plots from polynomial transformation models is useful for evaluating the abundance and distribution of control points and thereby, model suitability. Models which are statistically accurate at control point locations may be creating unusual and erroneous distortions in areas with few control points.

SUBGM.HCMM program, which is a modified version of the ORSER SUBGM program, digitally transforms the "original" space data set to conform spatially with the "corrected" space data set. The modification is such that the coordinate system of the "original" space data set corresponds directly with that of the "corrected" space data set after transformation. This simplifies subsequent needs to subset common blocks from a registered pair of images. Resampling options such as nearest-neighbor or cubic-convolution are available.

Manual verification completes the cartographic correction process. Contrast-enhanced grey level Versatec plots are generated for the data sets undergoing registration and overlaid on a light table. The complete cartographic correction procedure is often repeated several times before obtaining suitable results with accuracy dependent upon good control point selection and distribution, as well as somewhat subjective model selection.

Registration of HCMM Day/Night Pairs

Registration accuracy of diurnal thermal-infrared imagery for the five HCMM data sets obtained from NASA was evaluated by overlaying contrast enhanced DAY-IR and NIGHT-IR electrostatic plots on a light table. Data sets with misregistration errors greater than 2.0 pixels were re-registered. Control points (4-6) were selected, digitized and input to SAS statistical programs to calculate linear transformation functions necessary to transform the NIGHT-IR data to conform spatially with the DAY-IR data. Primary control points were bends in the Colorado and Green Rivers and topographic breaks along steep escarpments. NIGHT-IR imagery delineated few discernible surface features, thereby limiting control point selection. SUBGM.HCMM transformed the NIGHT-IR data set, followed by accuracy assessment. Cubic convolution resampling retained the linear relationship between adjacent pixels.

Geometrically registered DAY-IR and NIGHT-IR data sets were merged onto individual ORSER format tapes for each of the five dates using MERGE program, thereby creating five two-channel data sets. Congregation of the data as such provides more efficient multi-channel numerical computations as well as allowing future spatial transformations to be performed in single program executions, for each given date.

Registration of Multi-Temporal HCMM Data Sets

Analysis of temperature variability through the period encompassing the five HCMM dates required mutual spatial registration of the five DAY-IR/NIGHT-IR merged data sets. The 19 OCT 78 image was

selected as a base image, to which the remaining four dates were registered, primarily because of numerous obvious control points on this image and large mutual overlap with the other four images.

Imagery from DAY-VIS data, already registered to merged DAY/NIGHT data, was used for control point selection for each date primarily because of user familiarity with surface responses in visible and near-infrared wavelengths. Control points (20 to 30) consisting of river bends, small lakes and topographic features were digitized for each of the four registrations. Control point coordinates were input into SAS programs which generated linear transformation functions.

Control points with large residual errors were re-evaluated on the imagery and eliminated if unreliable. SUBGM.HCMM used the linear functions to transform merged DAY/NIGHT pairs from four dates to conform spatially with the 19 OCT 78 data set. Cubic convolution techniques were used to resample the data sets. Registered DAY/NIGHT pairs were output to five separate tapes, DAY-IR imagery from each date was generated on a Versatec plotter and overlaid using a light table to verify registration accuracy of the five dates.

Average Daily Temperatures

Surface temperature variability on an annual cycle is best examined using average daily temperatures (ADT) values at each pixel location rather than daytime or nighttime temperatures which are subject to much greater variability. OSTADT program was developed and used to calculate ADT data sets for each of the five dates. Input consisted of daytime (DAY-IR) and nighttime (NIGHT-IR) temperature binary pixel values scaled from 0-255. A lookup table, generated

using a conversion equation provided by NASA (NASA, 1980), converted DAY-IR and NIGHT-IR pixel values to apparent temperatures which were averaged and then converted back to binary values. The five ADT data sets were merged using MERGE program creating a five-channel data set.

Heat Flow Equation

One dimensional vertical heat flow in a soil is described by the following differential equation (Merva, 1975):

$$\frac{d^2T}{dZ^2} = \frac{1}{\alpha} \frac{dT}{d\tau}$$

where: T = Temperature

Z = Depth below the surface

α = Thermal diffusivity

τ = Time

The model has several important assumptions. Firstly, no temperature gradient exists in the horizontal directions. Heat flow between horizontally adjacent regions is negligible. Secondly, no heat is lost or gained as a result of moisture changes, chemical reactions or biological respiration. Also, the soil mass is considered homogeneous and isotropic with infinite depth.

Solution of the differential equation by Fourier series expansion yields the following expression which describes the first harmonic of the Fourier series:

$$T(Z,\tau) = Tmast - Ae^{-(\pi/365)^{1/2} \cdot Z} \cos \frac{2\pi}{365} \cdot \tau - (\pi/365 \cdot \alpha) \cdot Z)$$

where: $T(Z,\tau)$ = temperature at depth Z and time τ.

Tmast = mean annual soil temperature

A = annual amplitude of annual sine curve at surface

α = thermal diffusivity

The periodic nature of the primary energy source of solar radiation suggest a sinusoidal periodic annual response of soil temperature. Annual fluctuations are represented by the magnitude of the curve's amplitude over the 365 day cycle. Time is measured in days from the date of minimum annual temperature.

The amplitude is greatest at the soil surface and decreases exponentially with depth as a function of the thermal diffusivity of the soil layer. Soils with high thermal diffusivity allow rapid penetration of heat to greater depths, thereby distributing the heat over a larger volume. These soils, therefore, exhibit relatively uniform annual and diurnal temperature fluctuations. Soils with low diffusivity, however, concentrate heat in surface layers producing large temperature fluctuation with rapid dampening of fluctuations with depth.

Soil diffusivity creates a phase lag of the temperature wave as depth increases. The greater the diffusivity, the smaller the phase lag as temperatures at lower depths rapidly respond to energy changes at the surface.

Solution of the heat flow equation of the soil surface ($Z = \emptyset$) yields the following:

$$T(\emptyset,\tau) = Tmast - A \cos(2\pi/365 \cdot \tau)$$

This equation simply describes a sinusoidal annual surface temperature curve as a function of time measured in days. Thermal diffusivity variability is contained within the amplitude term, such that soils with high diffusivities have low surface amplitudes.

Calculation of MAST and AMP

The heat flow equation solved at the soil surface describes a straight line if $T(\emptyset,\tau)$ is considered to be a dependent variable affected by change in the independent variable $\cos(\frac{2\pi}{365}.\tau)$. Tmast then becomes the intercept with the amplitude (A) being the slope. Therefore, repeated observations of surface temperature at known times, as measured from the date of minimum annual temperature in days, allows least squares regression techniques to estimate the mean annual soil temperature and amplitude as well as confidence statistics for each estimated value.

Average daily temperature data sets represent surface temperatures distributed through the annual cycle, but the overpass date for each data set gives no indication of time, $\cos(\frac{2\pi}{365}.\tau)$ as measured from the data of minimum annual surface temperature. A sine curve was fit to 30 years of air temperature data collected at the Moab, Utah weather station in the center of the study site. The annual air temperature and soil surface temperature cycles were synchronized with the assumption that phase shifts on an annual basis are negligible.

OSTFIN program was developed to accept multi-temporal average daily surface temperature data sets plus their associated collection times relative to an annual temperature cycle and to calculate the

mean annual soil temperatures as well as amplitude for each pixel location. The five ADT data sets were input to OSTFIN thereby producing MAST and AMP data sets using least squares linear regression techniques. Since the predicted MAST and AMP values are actually regression coefficients, their standard deviations were also calculated to give some indication of the "goodness of fit" of the average daily temperatures to a theoretical annual sine curve for each pixel location.

OSTFIN program outputs MAST and AMP channels, plus their respective standard deviations (STDMAST, STDAMP), onto a single ORSER format tape with binary pixel values directly indicating degrees centigrade. This format is, therefore, compatible with all ORSER image processing and statistical analysis software necessary to allow subsequent evaluation of relationships between estimed values and surface terrain features.

Registration of HCMM to Base Map

Density-sliced grey level plots of HCMM, MAST and AMP data sets were produced to examine their spatial distributions and correlations with surface features. It was difficult to determine exact geographic locations due to the lack of recognizable features. Registration was performed to overlay HCMM, MAST and AMP data sets onto a USGS 1:250,000 topographic base map of the Moab quadrangle (Plate 1).

Control points (37) were selected from DAY-IR imagery and the topographic base map. A coordinate system was assigned to the base map such that 40 units of scan lines and elements occurred per 2.54 cm. The Versatec plotter has a resolution of 0.01277 cm or 200 lines

per 2.54 cm. A line and element repetition factor of 5.0 on Versatec grey level plots, therefore, corresponded accurately to the scale of topographic base map.

Control point coordinates were input into EZLS program that produced a third order polynomial transformation model. SUBGM.HCMM program transformed the HCMM data sets to match the base map projection. Electrostatic grey level plots were overlaid onto the base map to evaluate registration accuracy.

Color Monitor Displays

Several individual images were selected for color display in order to enhance contrast between grey level classes. Class delimiters were selected from channel histograms and entered into NMAP program. Rather than producing a lineprinter map, however, an ORSER compressed map was output to disc. The compressed map was then converted into a format suitable for the Ramtek graphic display system using RAMTEK program (Sykes, M.S. thesis in progress). A Conrac color monitor with a 512 x 512 pixel resolution displayed each 200 x 200 pixel image. Options within the RAMTEK program allowed display of titles and legends on each image.

Each class was represented by an individual color. The Conrac's three primary color guns (RED, GREEN, BLUE) each permit 15 intensity levels which are interactively controlled from a Tektronix graphic terminal. Display of the spatial distribution of individual classes greatly improves interpretability. Effort was made to standardize colors representing transitions from high to low temperatures. However, variability in the number of classes displayed on each image made complete standardization impossible.

All images were photographed from a tripod using a Nikon camera with a Micro Auto Nikor lens and Ektachrome 64 color positive slide film. Positive color prints were produced for each image.

Results and Discussion

Cartographic Correction

HCMM DAY/NIGHT Pairs

Five registered DAY/NIGHT pairs obtained from NASA were evaluated for accuracy. Considerable misregistration was evident in three of the five data sets (Table 1). Accuracy was measured by digitizing common control points on DAY-IR and NIGHT-IR imagery for each date and calculating the euclidean distance discrepancy between matching coordinates. Other investigators (Watson, 1980) have reported misregistration on the order of five pixels. NASA provides no accuracy index for assessment. The magnitude of misregistration error will depend upon the proximity of the study site to the margins of the original swath path. Registration quality is scene dependent and affected by the number of control points.

Table 1. Registration assessment statistics of NASA DAY/NIGHT pairs

DATE	CONTROL POINTS	MEAN ERROR (Pixels)	ERROR RANGE (Pixels)
4 SEP 79	5	3.66	0.4 - 5.5
13 JUL 79	6	3.85	2.0 - 5.3
19 OCT 78	4	15.48	14.2 - 17.9

WARP Application

WARP program aids model selection when polynomial transformation models are applicable during cartographic correction. WARP produces preview plots graphically displaying the spatial distortion of an "original" space data set that would occur using a selected transformation model. Output is directed to either the Houston Instruments or Versatec plotter.

WARP accomplishes several feats. Firstly, WARP quickly evaluates format correctness of COEF cards that are input to SUBGM program to indicate the transformation model coefficients. Secondly, the quality of the control points relative to the selected model can be evaluated by looking for unusual non-linear distortion between control points. Thirdly, proper distribution of control points throughout the image can be improved by delineating regions where unusual distortion is occurring due to lack of control points. Lastly, large errors in control point coordinate digitization can be illustrated by unusual distortion in a particular area.

The following example illustrates the use of WARP during the registration of HCMM data to the 1:250000 topographic base map. Ideal control points (26) were selected primarily along the Colorado River as indicated by their linear orientation on Figure 7. An "initial" third-order transformation model was selected with standard errors of 0.47 elements and 1.60 scan lines. Although the quantity of control points was adequate and the residual error acceptable, WARP plots indicated several problems. Areas containing abundant control points appeared rather uniformly stretched. Regions with none or few control

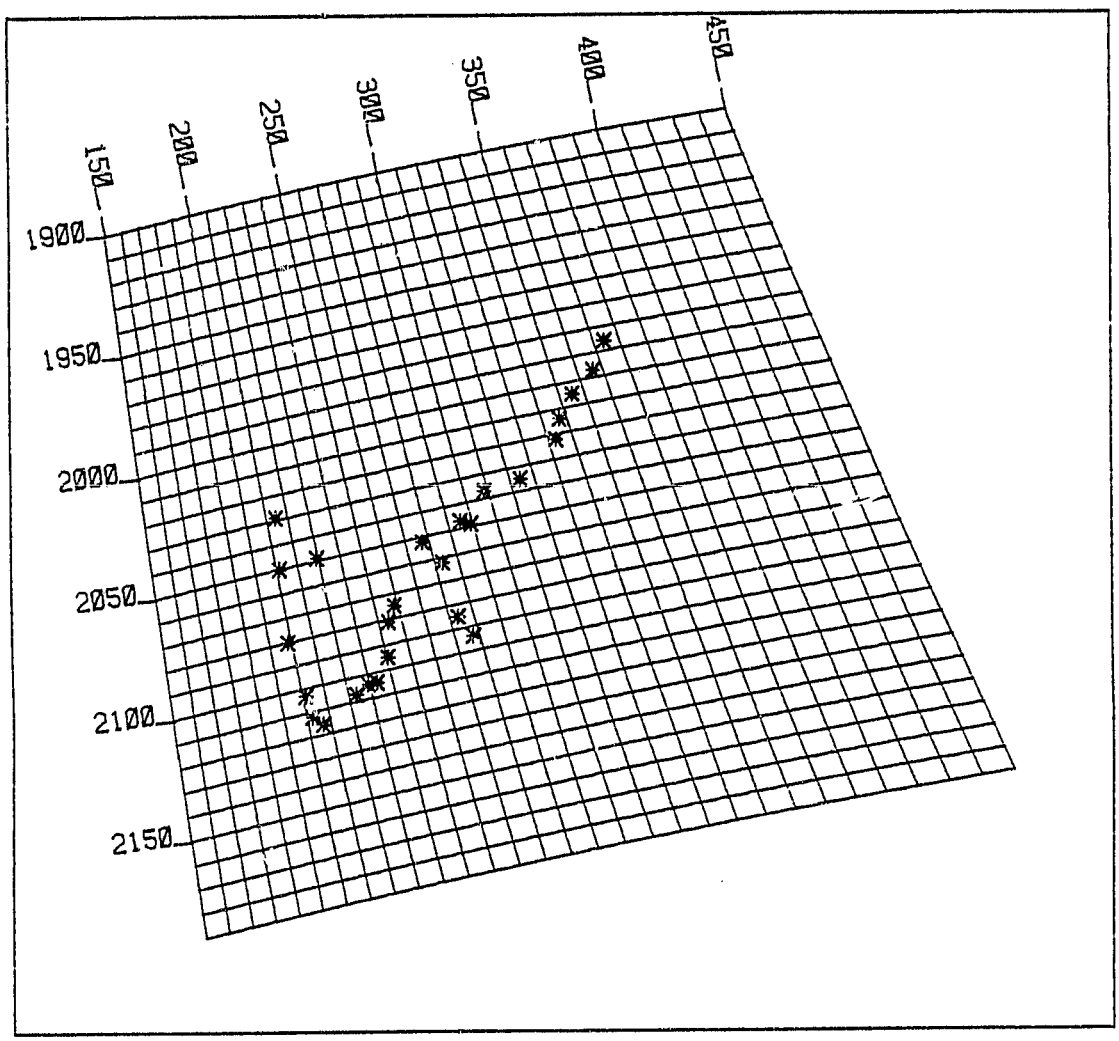

Figure 7. WARP plot illustrating image distortion which will result from using the "initial" transformation model that was developed from an inadequate selection of control points.

points, in the upper left and lower right regions of the plot were unusually distorted. The transformation polynomial was unrestricted in these regions. Versatec plots (Figure 8) reveal actual image distortion after actually transforming the data set using SUBGM program. Subsequent enlargement and overlay onto the topographic base map showed reasonable registration accuracy within areas with many control points but extreme misregistration error elsewhere.

In order to restrict the transformation polynomial throughout the image and reduce abnormal distortion, additional control points were selected. Although the new control points were considered to be less accurate than the original group, they served to confine the polynomial of the "final" model in previously unrestricted regions. WARP plots (Figure 9) clearly reveal more uniform stretch throughout the entire data set. Enlargement and overlay of Versatec plots (Figure 10) of the actual transformed data set onto the base map revealed good fit.

Analysis of residual error about the control points alone is an inadequate measure of model adequacy when using polynomials during rubber-sheet stretching. The distribution of control points is equally as important as the abundance. The WARP program will be added to the ORSER software system.

Daytime Temperatures

Temperatures discussed in subsequent sections were derived using conversion equations provided by NASA (1980) and are not absolute surface temperatures. These values have not been adjusted to compensate for surface emissivities, atmospheric attenuation, sky

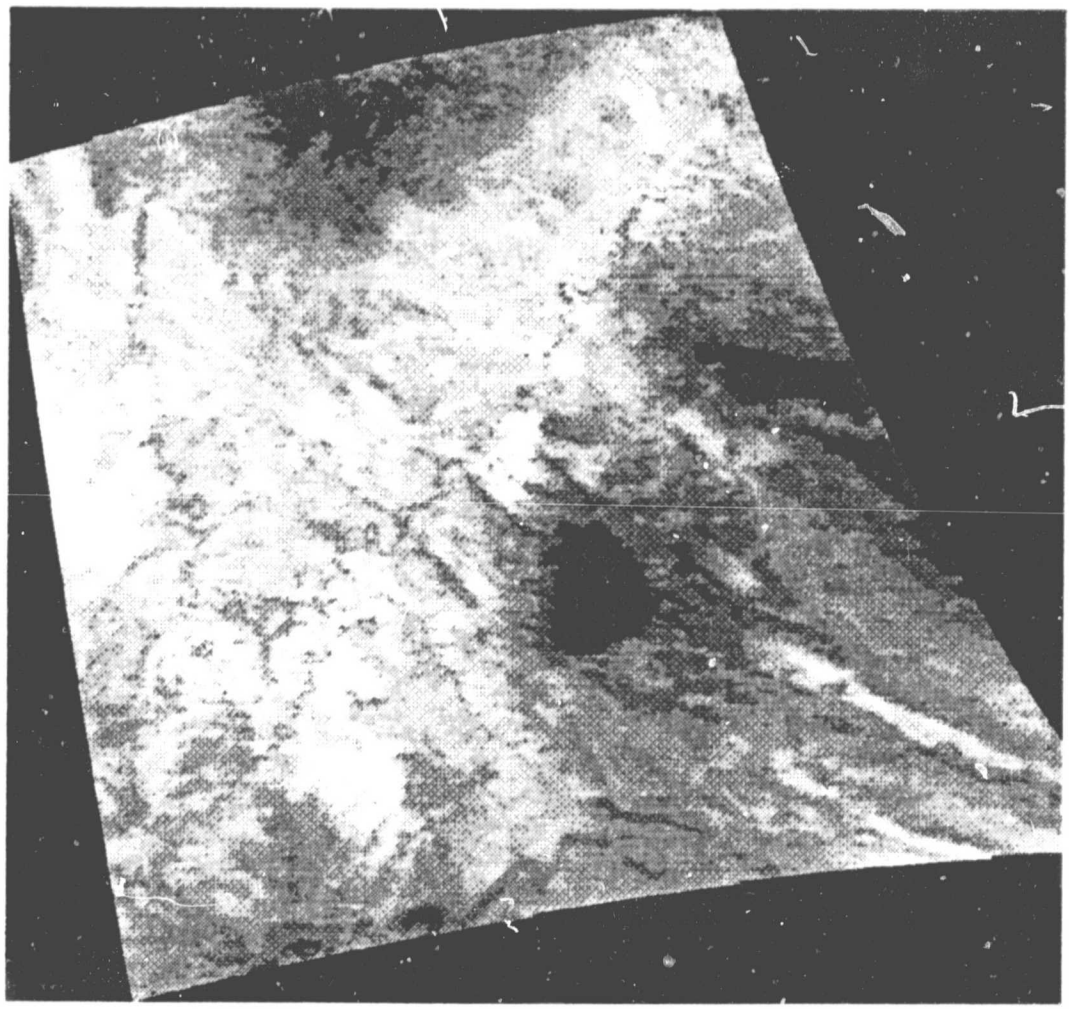

Figure 8. Contrast-enhanced grey level image of the transformed data set that was produced using the "initial" transformation model.

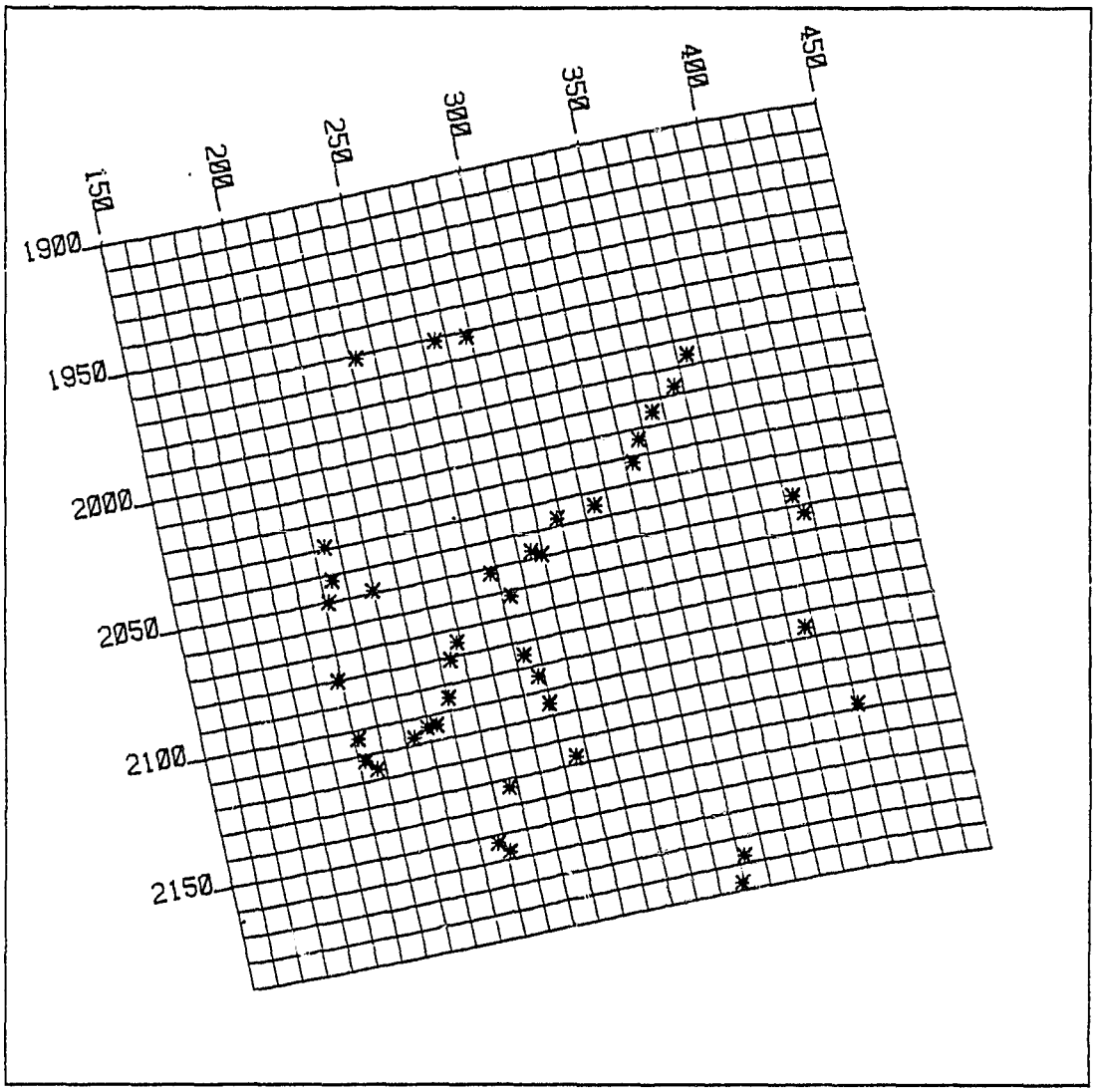

Figure 9. WARP plot illustrating the image distortion which results from using the "final" transformation model that was developed from an adequate selection of control points.

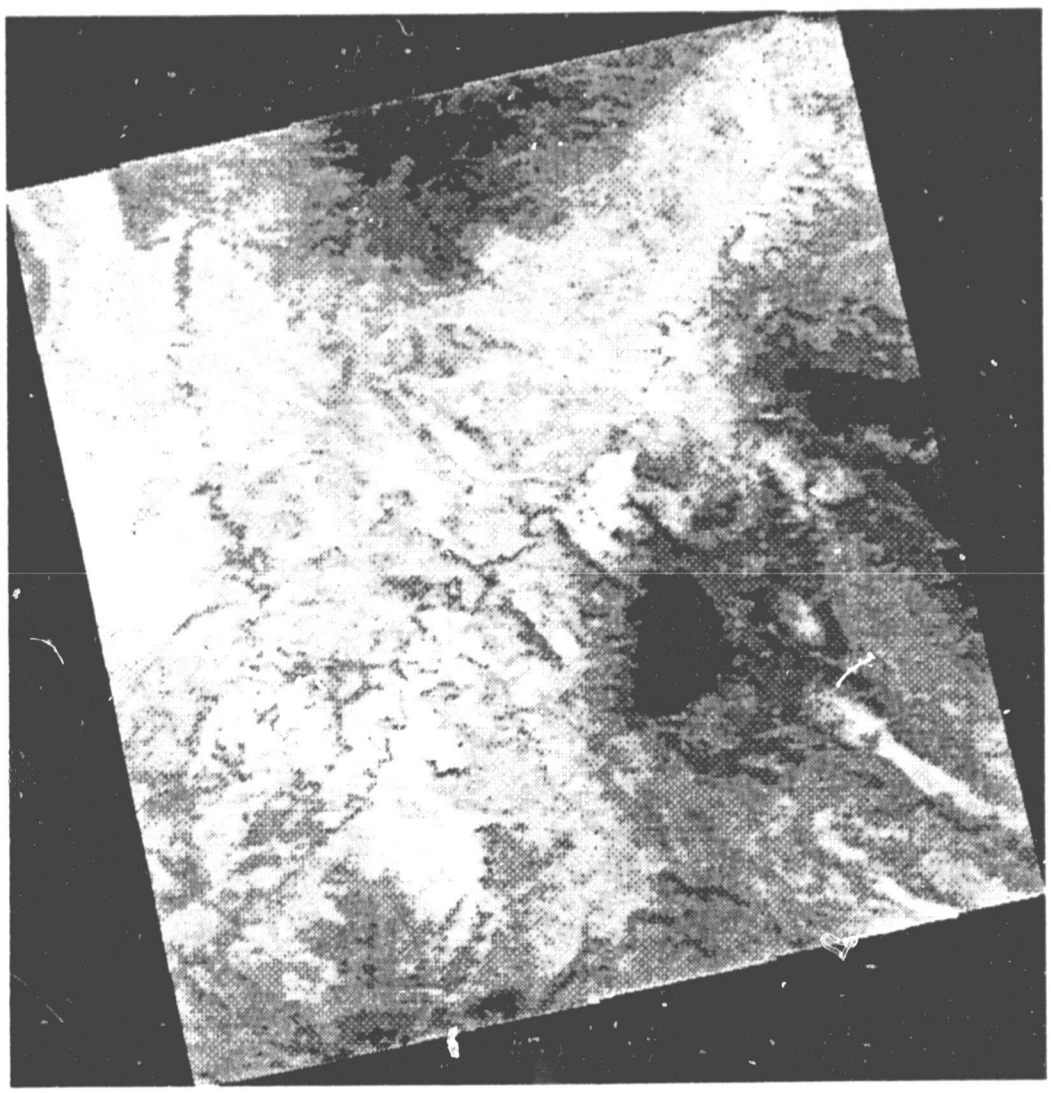

Figure 10. Contrast-enhanced grey level image of the transformed data set that was produced using the "final" transformation model.

radiation or HCMR sensor calibration variability. Although the temperatures are not absolute, they do show relative temperature differences among surface features.

Spatial temperature relationships among surface features was relatively constant on the five daytime temperature data sets. The following description specifically refers to the 19 OCT 78 scene (Figure 11) which typifies the type of information available on each date.

Surface temperature extremes ranged from -13°C to 29.8°C. Cloud coverage over the La Sal Mountain peaks produced the extremely low temperatures. Maximum temperatures occur on nearly bare, heavily dissected shale soils in an area known as Pinto Wash located directly south of the town of Cisco.

Most temperatures fall between 10°C and 26°C. Temperatures over the entire data set are approximately normally distributed, with a mean of 21.6°C and a standard deviation of 6°C. The standard deviation is somewhat inflated due to low cloud cover temperatures over the La Sal Mountains. The predominant trend shows decreasing temperatures with increases in elevation. Warmest temperatures (26-29°C) are found primarily in low-lying areas between 1200 and 1525 meters, such as the deep, complexly-incised Canyonlands region. The floors of Salt and Professor Valleys show equally high temperatures. Large bodies of heavily dissected soils formed in soft marine shale along the base of the Book Cliffs are well delineated. A tongue of high temperatures extending southeastward along the western edge of

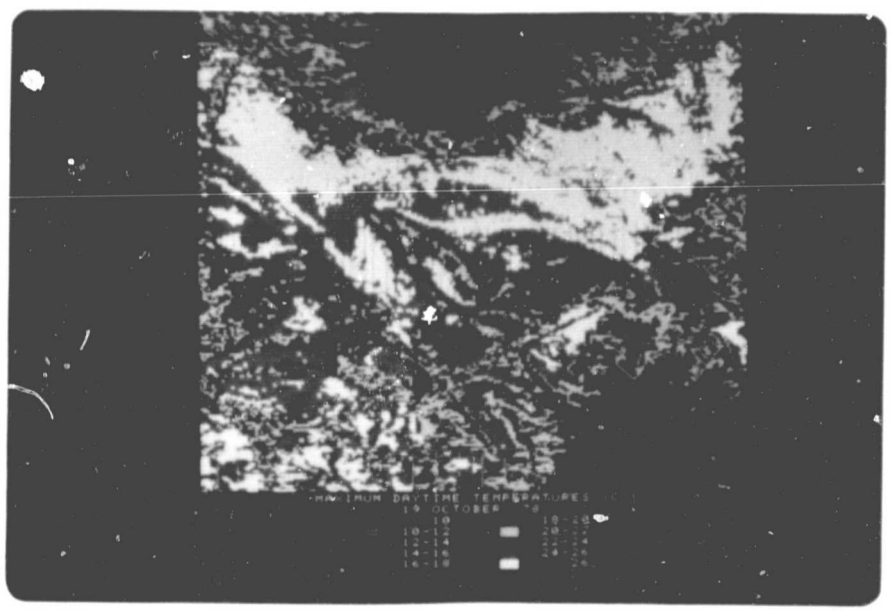

Figure 11. HCMM daytime temperature image (19 October 1978)

Salt Valley outlines clearly the southern extent of the marine shale deposits. This zone contrasts sharply with mesas along the fringes of the Book Cliffs. Vegetation is sparse in these warm regions and is dominated by sagebrush and blackbrush, both good indicators of warm temperatures.

Plateaus and mesas bordering the Colorado and Green River canyons are slightly cooler with temperatures ranging from 22-26°C. In these areas, elevations are between 1525 and 1830 meters.

Deeply incised narrow canyons forming the drainage network of the Green and Colorado Rivers are well-delineated with temperatures between 20-22°C. Although low in elevation (1350-1550 meters), increased shading, moisture and vegetative cover cause temperatures to be approximately four degrees lower than bordering plateaus at elevations over 1900 meters.

Mesas and plateaus surrounding the La Sal Mountains are outlined clearly, with temperatures between 14 and 18°C depending on elevation. Steep, high escarpments result in large temperature change over short horizontal distances with temperature gradients increasing toward the summit of the La Sal Mountains and Book Cliffs.

Although elevation clearly controls overall temperature distribution, secondary factors such as aspect, moisture, vegetative cover and surface material density, are illustrated as well. Steep northeast facing slopes along Castle Valley and Spanish Valley show temperatures of 14-16°C compared to 20-22°C temperatures on the tops of neighboring flat-lying plateaus. Similar aspect effects occur

along escarpments of Adobe and Fisher Mesas in Castle Valley and throughout the complex aspect changes throughout the Canyonlands region.

Effects of increased moisture on surface temperatures are evident in Spanish Valley. Several large ponds, some of which are uranium tailing ponds, just north of Moab, show temperatures of 12-14°C compared to 24°C temperatures common to dry soil and rock surfaces at similar elevations. Spray-irrigated ranches south of Moab and in Professor Valley are 2-4°C cooler than surrounding dry soils.

The Colorado River is 2-4°C cooler than surrounding soil and rock surfaces at similar elevations in Professor Valley. Temperature differences between the river and soils are buffered somewhat. Because of the narrow width of the river (approximately 50 meters), the 600-meter resolution HCMR sensor averages portions of the river and its banks.

Material density differences among surface materials appears to be effecting temperatures in several locations. Deep, sandy soils in the center of Salt Valley show temperatures greater than 26°C. Klondike Bluff and Devils Garden border Salt Valley about 60-90 meters higher in elevation and consist partially of complex arrangements of fractured bedrock producing 30 meter high vertical fins. Temperatures of these areas drop to 20-22°C overall with some places as cool as 18-20°C. Elevational differences are not great enough to account for such large temperatures differences. Lower thermal conductivity of the sandy soils compared to the dense bedrock exposures may be causing the difference noted. Low thermal conductivity of deep, dry, sandy soils concentrate heat energy in a thin surface layer, producing high

surface temperatures. Dense bedrock, on the other hand, conducts incident heat to deeper layers producing lower surface temperatures. The geometry of the vertical bedrock fins in Devils Garden may also contribute to the relatively cool temperatures. The fins create much shadowing and serve to radiate heat from a larger surface area. Temperature differences are probably not due to emissivity differences between the red sandstone and red sandy soils. Hubner (1981) measured emissivity of red sandstone rock and red sandy soils of sandstone origin similar to those near Salt Valley. He gathered samples near Moab and showed the rock to have a higher emissivity in the 10.5-12.5 micron wavelength interval which would cause the rock to appear warmer on thermal imagery than the soil if both were at the same absolute temperature. Therefore, the temperature differences between the rock and soil in and around Salt Valley may be even greater than depicted on the imagery.

Somewhat similar effects occur on several structural benches where deep, well-drained, residual and eolian deposits derived mainly from sandstone are 4°C warmer than surrounding sandstone bedrock exposures at similar elevations. One such area called Big Flat located on a bench west of Moab across the Colorado River is over 300 meters higher than valley bottoms with similar temperatures. Other such areas identified on the USGS base map are Behind the Rock, Arths Pasture, Grange Pasture, and Hatch Point. Vegetation is primarily big sagebrush, snakeweed, blue grama, and blackbrush on the residual and eolian deposits, compared to sparsely scattered pinyon and juniper trees on the bedrock exposures.

The effect of albedo on surface temperatures is apparently expressed in daytime thermal imagery. Absorptivity measurements (Hubner, 1981) of two contrasting parent materials were made for the 0.4 to 1.1 micron wavelength interval. Absorptivity of grey shale soils from near Klondike Flat was 27% higher than red sandstone-derived soils near Moab Sand Flats. The grey shale region is clearly delineated on the daytime imagery as the large, relatively hot white area south of the Book Cliffs, that forms sharp, discrete boundaries with cooler sandstone material. High absorptivity may be contributing to the relatively high temperatures.

Table 2 summarizes the DAY-IR data sets for all five dates. Similar ranges of temperatures (30-32°C) are found in the SEPT, AUG, and MAY scenes. The unusually low temperatures in JUL and OCT result from cloud cover.

Standard deviations are remarkably constant with no apparent relationship between mean temperature and variance. The slightly inflated variance of the JUL and OCT scenes are due to cloud cover which was greatest in the OCT scene.

Table 2. Summary statistics for five HCMM daytime temperature data sets

DATE	MEAN TEMP (°C)	STANDARD DEVIATION (°C)	MINIMUM (°C)	MAXIMUM (°C)
12 MAY 78	26.7	5.5	4.8	37.8
13 JUL 79	40.4	5.6	-0.7	50.0
16 AUG 78	33.7	4.7	12.8	42.4
4 SEP 79	35.2	4.9	12.0	44.0
19 OCT 78	21.6	6.0	-13.0	29.8

Nighttime Temperatures

Nighttime temperatures (NIGHT-IR) of the 19 October 78 scene (Figure 12) varied less than the daytime temperatures, ranging from -13°C to 7.4°C. Minimum temperatures were associated with cloud cover over the town of Green River while maximum temperatures occurred in the center of the Canyonlands (White). Most temperatures ranged from -8°C to 6°C. Reduced temperature variability compared to the DAY-IR image reduced topographic detail considerably as is apparent in Figure 12. The time of overpass of the HCMM satellite does not correspond exactly with minimum nighttime temperature. Data collected by Gay and Hartment (1981) near Moab for two days in May showed that minimum nighttime temperature occur near sunrise (6:00 a.m.). The difference of surface temperatures between 2:30 a.m. and 6:00 a.m. for the two days were less than 2°C.

The inverse relationship between surface temperature and elevation is weaker in the NIGHT-IR image than in the DAY-IR image. Temperature inversions occur in some parts of the image with a ceiling at approximately 2150 meters based on overlays onto a topographic base map. Above the inversion, a temperature lapse occurs. The most striking inversion occurs over the region underlain by soft marine shale deposits along the base of the Book Cliffs (Blue). Elevations vary between 1340-1460 meters with temperatures of 0-2°C. The thermal boundary delineating this relatively cool region is very discrete. The same region had distinctly warm daytime temperatures. Low thermal conductivity of such sparsely vegetated soils tend to produce low nighttime temperatures but cold air drainage from the Book Cliffs might also be a contributing factor. Cold air drainage commonly

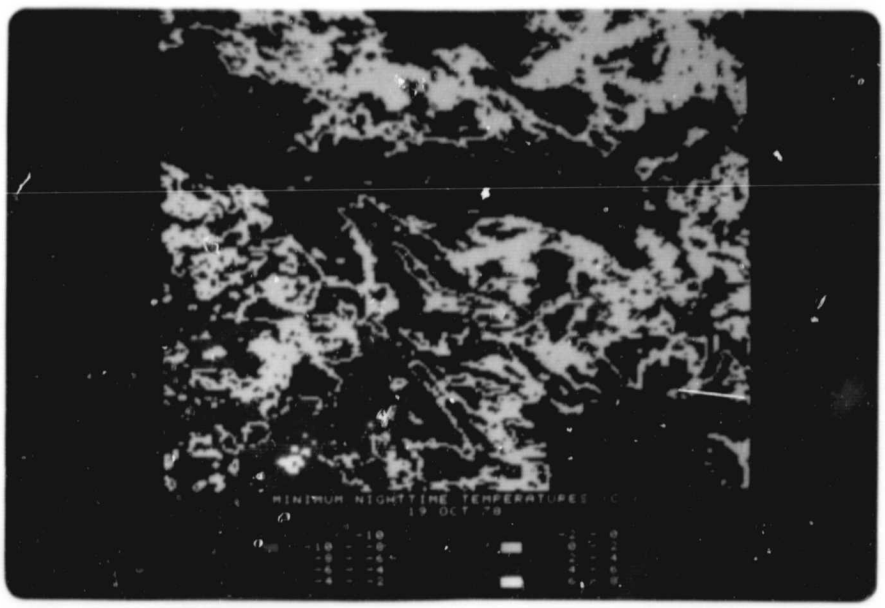

Figure 12. HCMM nighttime temperature image (19 October 1978)

occurs in basins and valleys throughout Utah with the tops of temperature inversion reaching 150-450 meters above the valley floor (Wilson et al., 1975).

Less drastic temperature inversions occur in valleys and canyons around the La Sal Mountains. Professor Valley, Spanish Valley, and Castle Valley show temperatures 2°C cooler than higher bordering plateaus.

The Canyonlands region remains warmest at night, almost 4°C warmer than surrounding plateaus and borders, although the Canyonlands have similar daytime temperatures as other valleys at the same elevation. Increased moisture in these areas may help minimize diurnal temperature fluctuations.

Some evidence in the DAY-IR imagery suggested that temperature differences between dry, sandy soils and adjacent bedrock may have been caused by differences in material density. The explanation is supported by several observations at night. For example, deep sandy soils covering the floor of Salt Valley show temperatures 2-4°C cooler than the adjacent bedrock outcrops of Devils Garden and Klondike Bluffs. In the DAY-IR imagery of the same area, the valley sands were warmer than the bordering bedrock. The large diurnal temperature difference of the valley soils compared to the surrounding dense rock material supports the idea that the temperature variability between the valley floor and bordering walls is due to density differences which, in turn, cause thermal conductivity differences.

Large deep, sandy eolian and alluvial deposits, such as Arths Pasture, Big Flat, Behind the Rock, and Grays Pasture are 2-4°C cooler

than bordering rock outcrop and shallow sands. The explanation again suggests density differences affecting thermal conductivity.

Diurnal surface temperature fluctuations, such as those previously discussed, reflect largely the thermal inertia of rocks or soils. Thermal inertia (P) can be described by the following expression:

$$P = (KC)^{1/2}$$

where: K = thermal conductivity

C = volumetric heat capacity

Thermal inertia measures the ability of a material to resist temperature change. External factors, such as solar radiation, air temperature, relative humidity, clouds and wind, constitute the driving force affecting diurnal temperature fluctuations which are resisted by thermal inertia. Therefore, materials with high thermal conductivities or heat capacities have high thermal inertia and exhibit smaller diurnal temperature fluctuations than materials with low thermal conductivities and heat capacities.

The previously discussed differences in diurnal temperature fluctuations between rock and sand probably indicates difference in thermal inertia.

The Colorado River, although barely detectable in some areas, is generally about 2°C warmer than adjacent surfaces. Small narrow stream-incised canyons are less detectable than they were in the DAY-IR imagery.

Interestingly, wet fluvial soils and ponds in Moab Valley are over 6°C cooler than adjacent soils. Moist soils and water bodies

typically are relatively warm during the night when compared to adjacent dry soils because of a larger specific heat capacity. These areas, however, are cool during the day and night which suggests that the source of water may be from deep wells.

Summary statistics of nighttime temperatures for all five dates appear in Table 3. Nighttime surface temperature variability based on standard deviations is very similar for all five dates and is considerably less than corresponding daytime data sets. The range of nighttime temperature values is less than the range of daytime temperatures.

Table 3. Summary statistics for five HCMM nighttime temperature data sets

DATE	MEAN TEMP (°C)	STANDARD DEVIATION (°C)	MINIMUM (°C)	MAXIMUM (°C)
12 MAY 78	1.7	2.8	-12.5	7.7
13 JUL 79	11.3	2.9	-1.1	17.6
16 AUG 78	6.6	2.2	-3.5	13.1
4 SEP 79	8.1	2.9	-2.3	14.5
19 OCT 78	0.1	3.1	-13.0	7.4

Correlations between daytime temperatures and nighttime temperature for each date appear in Table 4. With the exception of MAY, correlations are very low between daytime and nighttime temperatures. The slight positive correlation probably results from the inverse relationship of both daytime and nighttime temperatures with elevation. Low correlation indirectly indicates extreme variability in diurnal temperature fluctuations throughout the site. Low thermal conductivities and or cold air drainage contribute to large daily temperature fluctuations.

Table 4. Correlation of DAY-IR and NIGHT-IR data set for five dates

DATE	CORRELATION (r)
12 MAY 78	0.74
13 JUL 79	0.47
16 AUG 78	0.37
4 SEP 79	0.24
19 OCT 78	0.25

Summary statistics of day/night data sets indicate greater variability of mean daytime temperatures than nighttime temperatures throughout the period of coverage. Mean daytime temperatures were regressed against mean nighttime temperatures for four of the dates. The OCT scene was not included due to cloud cover. As expected, a strong linear relationship exists (R^2 = 0.996), but the difference between mean day and night temperatures on any given date increases as mean daytime temperatures increase. For every 1 degree increase in mean daytime temperature there is only a 0.7 degree increase in mean nighttime temperature.

Average Daily Temperatures

Spatial variability of average daily temperatures (ADT) (Figure 13 and Figure 14) is primarily controlled by topography with distinct contouring evident around the Book Cliffs and La Sal Mountains. Narrow river canyons are about 2°C cooler than bordering plateaus. Aspect effects are preserved from the original data set with temperatures on steep northeast facing escarpments along Spanish and Castle Valleys about 2-4°C cooler than adjacent flat surfaces.

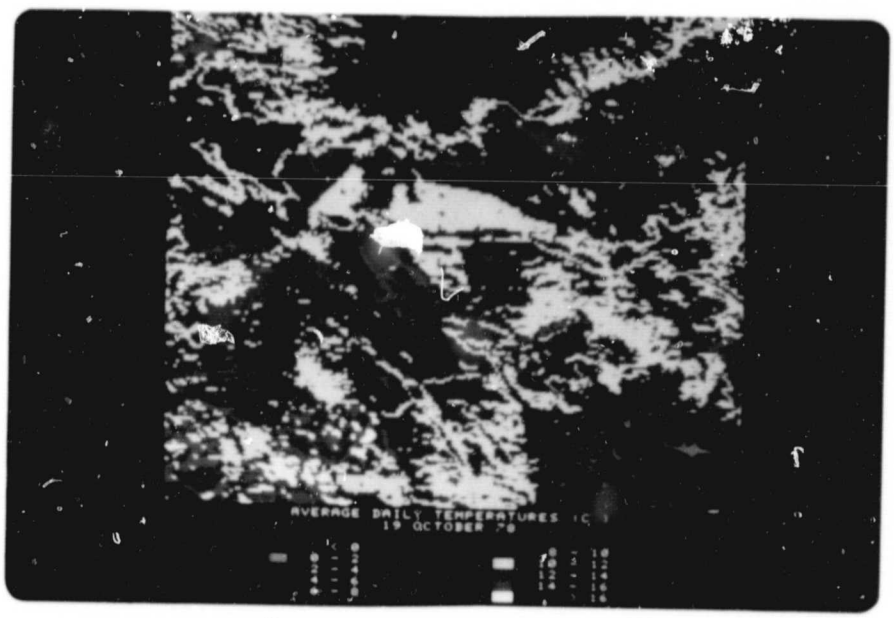

Figure 13. Average daily temperature image (19 October 1978)

ORIGINAL PAGE
COLOR PHOTOGRAPH

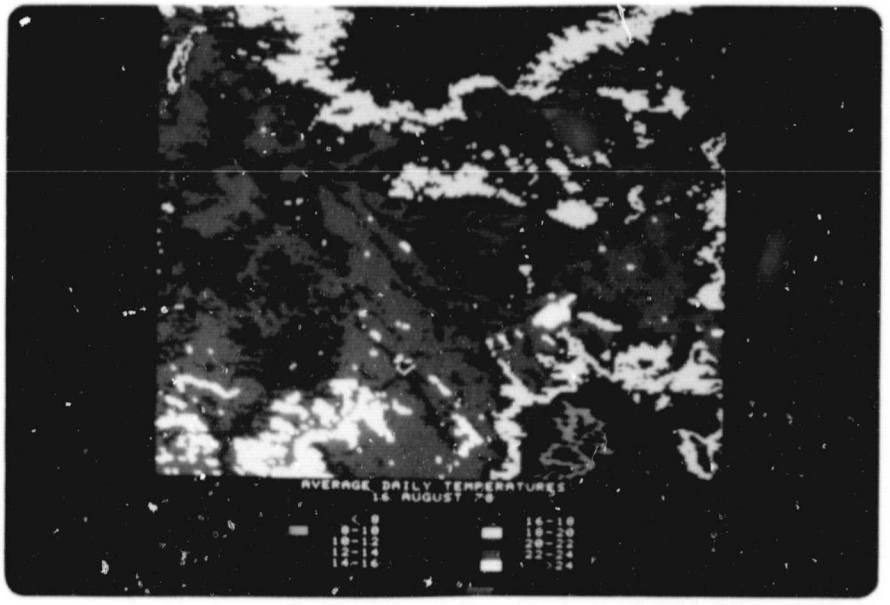

Figure 14. Average daily temperature (ADT) image (16 August 1978)

The large temperature differences (6-8°C) between adjacent surfaces of deep sand and bedrock that were prominent in daytime and nighttime images are reduced (0-2°C) in ADT imagery. The bedrock boundaries of Salt Valley known as Klondike Bluffs and Devils Garden are barely differentiated from the valley floor. Material density differences are probably producing large diurnal temperature fluctuations with less effect on diurnal averages. Other areas previously discussed, such as Big Flat, Behind the Rock, and Grays Pasture, show similar results.

The town of Green River with irrigated floodplain soils is 6-8°C cooler than the surrounding dry desert on the AUGUST ADT image. Moab Valley also shows distinctly cool temperatures.

The transition from marine shale derived soils, at the base of the Book Cliffs, to sandstone-derived soils is quite distinct in the 19 OCT 78 ADT imagery. Marine shale soils are about 2°C cooler than surrounding areas at similar elevation due to unusually cool nighttime temperatures.

Summary statistics (Table 5) for ADT data sets reveal consistent overall ADT variability throughout the five dates. Standard deviations are approximately midway between daytime and nighttime data sets previously reported. Correlations (Table 6) are very high between four ADT data sets. The reduced correlation of the October data sets with the other four is probably due to cloud cover producing unusually cold temperatures over some areas. High correlations suggest that relative spatial temperature relationships are consistent throughout the dates of coverage and will probably produce similar relationships among mean annual soil temperatures predictions.

Table 5. Summary statistics for five average daily temperature data sets

DATE	MEAN TEMP (°C)	STANDARD DEVIATION (°C)	MINIMUM (°C)	MAXIMUM (°C)
12 MAY 78	14.2	3.8	-8.1	21.2
13 JUL 79	25.9	3.6	4.7	32.8
16 AUG 78	20.0	3.1	6.2	27.3
4 SEP 79	21.6	3.1	5.9	27.9
19 OCT 78	10.8	3.7	-10.8	17.9

Table 6. Correlation matrix for five average daily temperature data sets

	MAY	JUL	AUG	SEP	OCT
MAY	1.00				
JUL	.93	1.00			
AUG	.93	.91	1.00		
SEP	.92	.93	.92	1.00	
OCT	.76	.80	.79	.79	1.00

Mean Annual Soil Temperatures

Calculated mean annual soil temperatures (MAST) range from -11°C to 17°C (Figure 15). Extremely cold temperatures (less than 0°C) over the high peaks of the La Sal Mountains should be ignored due to repetitive snow and cloud coverage. Maximum temperatures are found in the Canyonlands near the confluence of the Green River and Colorado River. Most surfaces temperatures range from 0°C to 16°C.

An inverse relationship with elevation is apparent in the MAST color image divided into 2°C intervals. Warmest temperatures (greater than 16°C) coincide with the deep, wide, complexly incised canyons of the Green and Colorado Rivers with a few small areas on valley floors. Associated soils are primarily well-drained and formed from residual

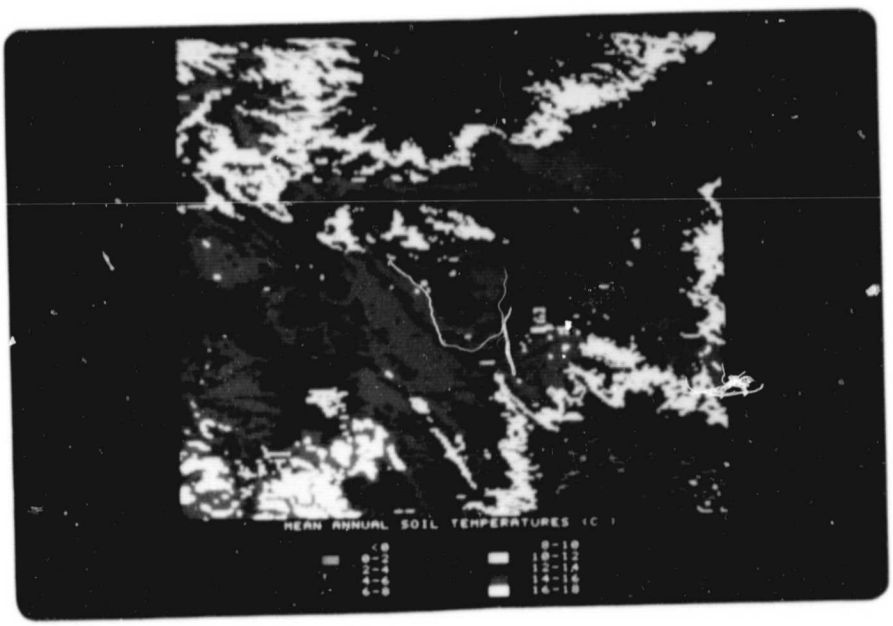

Figure 15. Mean annual soil temperature image (MAST)

or alluvial red sandstone. Depth varies from shallow to deep and often bedrock is exposed on steep slopes of the canyons and escarpments. Figure 16 looks eastward across the Canyonlands region towards Moab. Elevations range from 1220 meters at river level to approximately 1370 meters.

Most of the study area, shown as red and light red on Figure 15, is in the 12-16°C interval with an upper elevation of approximately 1830 meters. Temperatures decline another two degrees progressing from 1830 to 2130 meters atop Adobe and Fisher Mesas which border the La Sal Mountains and appear as yellow. Similar contours encircle the Book Cliffs. Slopes steepen in the La Sal Mountain from 2130-2440 meters indicated by narrower temperature contour bands (green) compared to wider bands on the more gradual incline of the Book Cliffs.

Elevations previously mentioned were gathered from MAST grey level electrostatic plots registered and overlaid onto a 1:250000 USGS topographic base map. Qualitative comparisons were made of temperature and elevation contours from Professor Valley (Figure 17) upward into the La Sal Mountains. The Book Cliffs region is north of the Moab quadrangle base map and was not evaluated. MAST decreased approximately 1°C for every 150 meters of elevational increase. Schmidlin (1981) reported an average MAST reduction of 1°C every 156 meters of elevation in Nevada where well-drained, bare, nearly-level soils of mainly mesic and thermic soil temperature regimes were analyzed from over 156 sites. Carter and Ciolkosz (1980) reported 1°C

ORIGINAL PAGE
COLOR PHOTOGRAPH

Figure 16. Deeply incised Colorado River canyons in Canyonlands National Park near Moab, Utah.

Figure 17. Landscape view of the La Sal Mountains and bordering mesas as seen from Professor Valley.

reductions in MAST every 313 meters increase of elevation in Pennsylvania, Maryland and West Virginia on mesic and frigid soils.

Effects of aspect on MAST is evident along steep, northeastern facing escarpments along Castle Valley and Spanish Valley. Temperatures there are approximately 2°C cooler than adjacent flat surfaces at similar elevations. Schmidlin (1981) estimated that MAST values, on the average, are reduced 1.9°C on northeastern aspects with slopes greater than 15%. Misregistration of multi-temporal data sets could cause similar temperature anomalies in regions of drastic topographic change. However, registration accuracy was thoroughly evaluated throughout the procedure and aspect effects were evident in imagery prior to registration.

Some of the MAST variability reflects surface moisture characteristics as evidenced in Spanish Valley where values range from 10°C to 14°C. Large uranium mining tailing ponds at the Colorado River portal exhibit minimum temperatures of 10-12°C as do irrigated agricultural fields south of Moab. Surrounding unirrigated soils are approximately 2°C warmer. Similar effects are seen over irrigated ranchland in Green River, Utah in the northeastern corners of the MAST imagery where irrigated farmland appears to be 4-6°C colder than surrounding desert. Cloud cover over the Green River area in the 19 October 78 scene contributes to the large temperature difference. A single irrigated ranch delineated in Professor Valley is 2°C cooler than surrounding dry soils. Schmidlin (1981) reported 5°C reductions in MAST over irrigated cropland in Nevada.

Narrow, steep-walled canyons of the Colorado River and its intermittent tributaries contrast with surrounding flat-lying plateaus

because of cool canyon temperatures. Although 150-300 meters lower in elevation, increased shading, moisture and vegetation combine to lower temperatures.

Surfaces bordering the Colorado River are consistently 2°C warmer than the river. However, both the river and bordering surfaces increase 2°C in the Canyonlands region where overall temperatures are 2°C higher than other areas at the same elevation.

A pattern of relatively cool temperatures coincides closely with soils derived from marine shale deposits along the base of the Book Cliffs. This same region showed unusually low nighttime temperatures for all five dates as previously discussed. Cold air drainage possibly contributes to the overall low temperatures.

Daytime and nighttime imagery consistently showed up to 9°C temperature difference between sandy soils in Salt Valley and bedrock outcrops on the bordering Devils Garden and Klondike Bluffs area. It was suggested that the temperature differences may be due to differing densities of the rock and soil. MAST imagery shows little variability across the valley with the exception of the northeastern facing wall south of Klondike Bluffs which is 2°C cooler than the valley floor.

MASTs were divided into classes corresponding to USDA mean annual soil temperature regimes (Figure 18). The pergellic areas (black) in the La Sal Mountains are caused by frequent cloud cover and should be ignored. The vast majority of the study site is mesic (red) bordered by thermic (white) regimes in the canyons and valleys and frigid or cryic (blue) regions in the mountains. The transition from thermic to mesic occurs at approximately 1500 meters whereas the mesic/frigid boundary occurs at about 2440 meters.

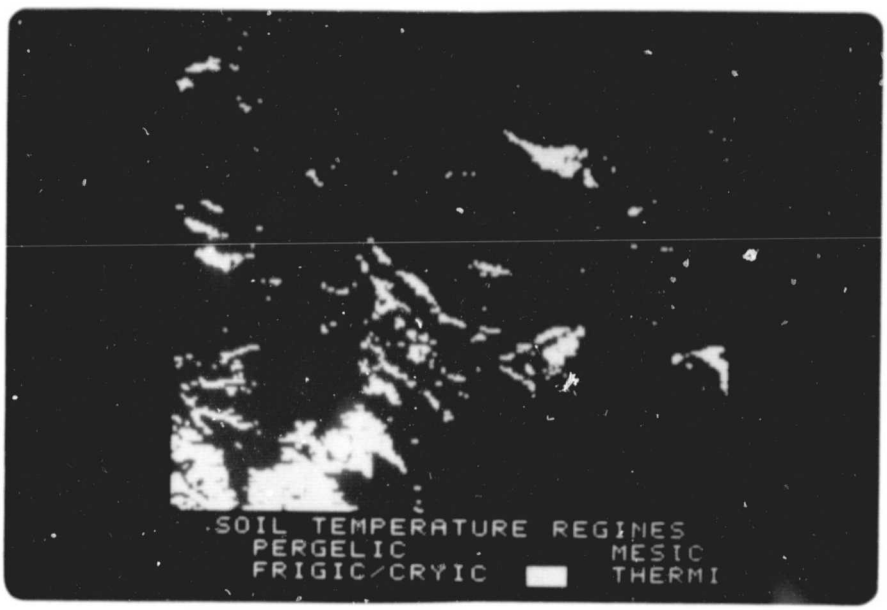

Figure 18. USDA mean annual soil temperature regime image

C-2

Mean annual air temperatures (MAAT) are often used to estimate mean annual soil temperatures (MAST) by simply adding 1°C to the MAAT. (Soil Survey Staff, 1975). Smith (1964) showed that the difference between MAST and MAAT may be greater in arid regions. This conclusion is supported by the work of Schmidlin (1981) who suggested differences of 3-6°C. MAAT values from weather stations at Moab (13.8°C) and Thompson (11.7°C) were lower than calculated MAST values of 14-16°C for each location.

The MASTs presented are not intended to be absolute values because of the obvious error incorporated in the DAY-IR and NIGHT-IR data sets used to calculate them. The MAST values do indicate relative differences between surface features. MAST imagery may be useful to show localized temperature variability within a relatively small region which would be useful especially when used in conjunction with regional indicators of MAST, such as MAAT.

Soil Survey personnel from the Soil Conservation Service, who were working in the study site qualitatively evaluated the spatial distribution of MAST estimates. They indicated that the imagery agreed very well with the patterns observed in the field during field mapping. Areas which they suspected of having thermic temperature regimes but were not mapped as such due to scaling considerations were delineated on the MAST imagery. They indicated that MAST imagery would be quite useful as a tool during the initial stages of a soil survey effort to delineate regions with unusual temperatures. The imagery could be used to direct more detailed field observations.

Annual Amplitudes

Calculated surface temperature annual amplitudes (AMP) ranged from 2°C to 31°C with most values confined to the 12-16°C range (Figure 19). Cloud and snow over the La Sal Mountains and the town of Green River show maximum amplitudes and are white on the AMP color image. The average amplitude is 13.36°C for the entire data set with a standard deviation of 2.17°C. The annual air temperature amplitude at Moab (13.3°C) corresponds closely with the calculated annual surface temperature amplitudes (12-14°C).

Reduced variability of the AMP predicted values compared to MAST data (standard deviation = 3.81) is reflected in a narrow range of predicted values and, therefore, less detailed discrimination of surface features. A weakly defined inverse relationsnip with elevation is evident on Figure 19 with largest amplitudes, seen as red (14-16°C) and white (greater than 16°C), closely associated with canyons, valley floors and dissected shale wash areas. Lower amplitudes, designated by blue (12-14°C), appear to correlate with higher plateaus, benches and mesas bordering valleys and canyons. Lowest amplitudes, shown in black (less than 12°C), primarily occur over the Book Cliffs and La Sal Mountains.

Soils derived from marine shale deposits along the base of the Book Cliffs have lower amplitudes than surrounding areas at similar elevations. Cold air drainage from the Book Cliffs is possibly dampening annual fluctuations as well as daily fluctuations.

Reduced annual temperature amplitudes caused by irrigation and soil moisture (Smith, 1964) are abundantly evident because of the heterogenerity of AMP values. Overlay of AMP and MAST imagery

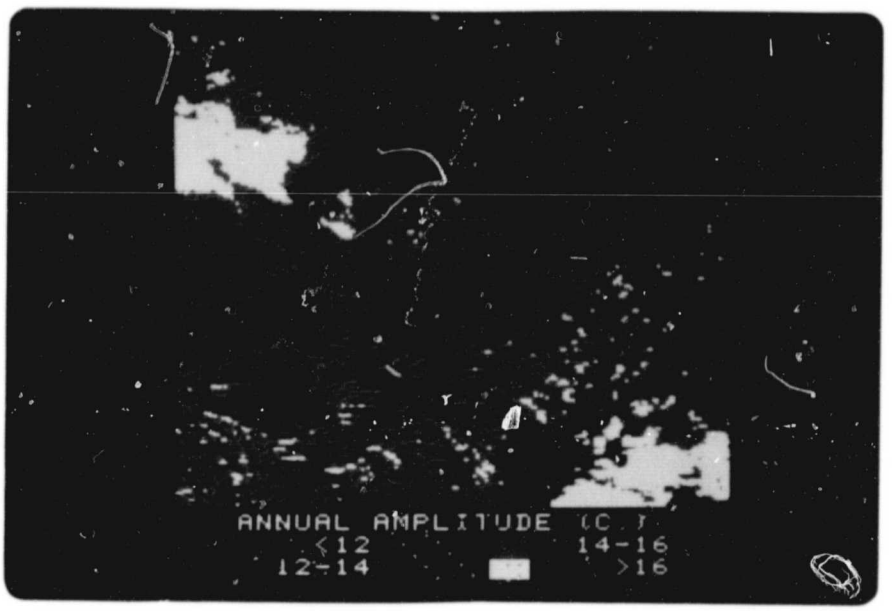

Figure 19. Annual surface temperature amplitude (AMP) image

apparently delineated one such irrigated ranch in Spanish Valley with relatively low MAST and AMP values. Large settling ponds in Moab Valley have amplitudes over 4°C lower than surrounding dry soils reflecting the high specific heat of water.

Standard deviations of predicted MAST (STDMAST) and AMP (STDAMP) values indicate the statistical accuracy of the estimates. STDMAST and STDAMP indicate how well the five ADT values for each pixel fit a theoretical sine curve.

STDMAST values (Figure 20) which range from 1°C to 5°C with most pixels falling in the 2-3°C range. Few distinct patterns related to surface characteristics are evident. Such large standard deviations suggest the need for additional HCMM overpasses to improve to statistical reliability of the MAST estimates.

Standard deviations of predicted annual surface temperature amplitudes (STDAMP) (Figure 21) range from 1°C to 5°C with most values falling in the 2-4°C range. Highest values occur at high elevations in the Book Cliffs and La Sal Mountains while lowest values occur in low-lying valleys and canyons. Such large values indicate a lack of statistical confidence in AMP predicted values, although a larger sample size would certainly increase the confidence.

Table 7 shows the correlation matrix for AMP, MAST, STDMAST and STDAMP data sets. The only significant relationship appears between STDAMP and STDMAST. No significant relationship exists between MAST

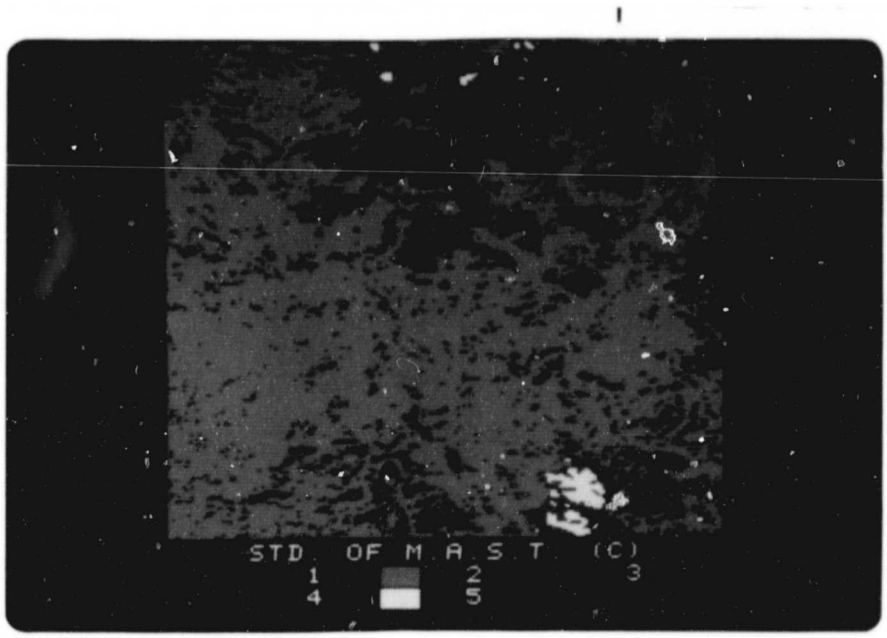

Figure 20. Standard deviation of MAST (STDMAST) image

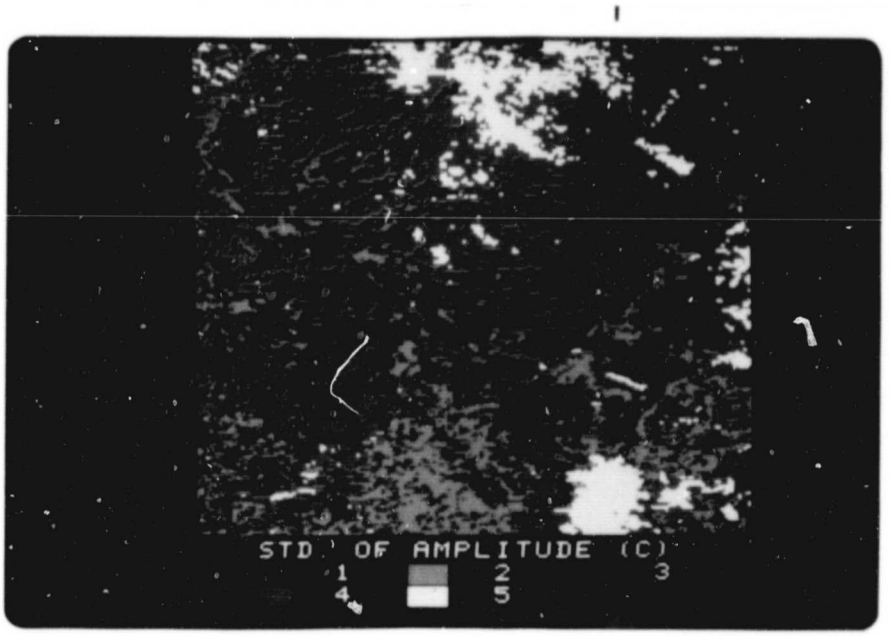

Figure 21. Standard deviation of AMP (STDAMP) image

and AMP indicating that no apparent relationship exists between the magnitude of AMP and MAST values, and the accuracy of the estimates.

The large correlation between STDAMP and STDMAST is reasonable since AMP and MAST are regression coefficients. Any variability in the AMP (slope) estimate will result in corresponding variability in the MAST (intercept) estimate.

Table 7. Correlation matrix of AMP, MAST, STDAMP, and STDMAST data sets

	AMP	MAST	STDAMP	STDMAST
AMP	1.00			
MAST	-0.44	1.00		
STDAMP	-0.05	-0.41	1.00	
STDMAST	-0.05	-0.40	0.87	1.00

Summary and Conclusions

HCMM thermal-infrared data were used to measure and display the relative distribution of surface and plant canopy temperatures in semi-arid east-central Utah. Daytime and nighttime surface temperature images were generated for five dates and qualitatively evaluated to determine the usefulness of diurnal HCMM thermal-infrared data for surface terrain analysis. Temperature contour maps were displayed on the Versatec electrostatic plotter or a color monitor.

HCMM data were used as input in a numerical model to estimate mean annual soil temperature (MAST) and annual surface temperature amplitude (AMP). The model uses average daily surface temperatures gathered throughout an annual cycle to fit a sine curve which describes the theoretical annual surface temperature response. HCMM daytime and nighttime surface temperatures data were used to estimate average daily surface temperatures.

Five multi-temporal HCMM data sets were used to test the model. Cloud and snow cover and poor radiometric data quality severely limited the selection of HCMM data sets. Statistical confidence estimates were generated to evaluate the accuracy of the estimated MAST and AMP values.

Spatial registration and digital combination of the five HCMM data sets was performed prior to utilization in the model. Techniques were evaluated to accurately register multi-temporal HCMM data sets to each other and HCMM data sets to topographic base maps for geographic reference. WARP program was developed to aid registration using "rubber sheet stretching" techniques.

Firstly, surface temperatures determined using conversion equations provided by NASA do not represent absolute temperatures. Factors such as surface emissivity, atmospheric attenuation, background sky radiation, and partial vegetative cover combine to make the task of absolute surface temperatures calculation very difficult, if not impossible. The problems are intensified over diverse terrain. Even with sophisticated models to correct for these environmental factors, calibration accuracy of the HCMR sensor is questionable. Most of these factors, however, affect an individual HCMM data set as a whole, thereby preserving relative temperature differences throughout an area. This is true providing that there are no large differences in surface emissivity. Throughout homogenous desert areas with sparse vegetative cover and uniform moisture distribution this is a reasonable assumption.

HCMM daytime temperatures correlate primarily with local topography. Elevational gradients show distinct inverse relationships with temperature. Sharp topographic breaks along actively eroding plateaus and mesas can be used to outline geologic and geomorphologic boundaries. Northeast-facing slopes appear cooler than south or southeastern slopes. Additional temperature patterns in HCMM daytime temperature imagery correspond to differences in surface moisture and rock and soil densities.

Qualitative interpretation of HCMM surface temperature measurements over a region provides useful information regarding localized environmental conditions which are important in soil genetic development. HCMM imagery also can quantify local effects as conceptually realized, such as the temperature difference between north and south slopes.

HCMM daytime thermal-infrared imagery reveals many surface characteristics, such as intricately incised drainage network and escarpments, not detectable on HCMM nighttime imagery. Surface temperature variability is significantly lower in nighttime data sets compared to daytime thereby producing diminished image contrast and reduced topographic detail.

Although not quantitatively addressed in this exercise, HCMM diurnal surface temperature data could be used to delineate soil and rock material based on diurnal temperature fluctuations. Rocks and soils differing in density and moisture content may be differentiated based on diurnal temperature fluctuations. Temperature fluctuations at the surface are largely controlled by thermal inertia or the

ability of a material to resist temperature change. Thermal inertia mapping of bare soils offers a promising new method to map soil and rock characteristics.

Mean annual soil temperature (MAST) and annual surface temperatures amplitude (AMP) estimates are not absolute values because of the inherent error within the original HCMM diurnal data sets used as input into the model. However, relative temperature differences are preserved such that the spatial distribution of MAST and AMP values can be mapped.

Indeed, MAST estimates correlate highly with elevational gradients and aspects which are important factors affecting annual soil temperature within a local region. MAST reduction associated with surface moisture or irrigation can be delineated.

MAST estimates obtained using HCMM data might best be used in conjunction with ancillary data or "tiepoint" data which offer some indication of absolute MAST values. For example, mean annual air temperature (MAAT) could be used to determine regional estimates of absolute MAST values, whereas HCMM estimates of MAST could be used to delineate more localized variability within a geographic region. Standard techniques used to estimate MAST cannot account for the localized surface temperature variability expressed by HCMM data.

MAST imagery can provide information useful in the early stages of a soil mapping effort. Unusually warm or cool areas could be used to indicate areas where more detailed mapping and investigation should be directed. Variability in surface temperatures certainly indicates

different environments experienced by soil and rock surfaces from which physical properties can be inferred as well as their relationship to soil genetic development.

Spatial overlay and digital combination of multi-temporal HCMM data sets can be achieved with sufficient accuracy to allow analysis of diurnal or annual surface temperature variability. Linear transformation models are adequate to register HCMM DAY/NIGHT pairs and multi-date data sets. HCMM DAY/NIGHT "registered pairs" provided by NASA show large misregistration errors and may need to be re-registered for detailed surface terrain analysis, especially in areas with large topographic variability.

Polynomial transformation equations or "rubber sheet stretching" may be necessary to register HCMM data sets to 1:250000 topographic base maps. WARP program reduces the subjectivity of transformation model selection. WARP quickly provides the user with an inexpensive preview plot that graphically shows how and where one image is distorted to conform spatially with another. WARP plots can be used to evaluate control point accuracy and distribution and subsequent transformation model selection.

"Rubber sheet stretching" acturacy remains largely a function of the ability of an operator to accurately locate and digitize control points. Location and digitization of control points directly from Versatec electrostatic plots is fast, accurate and provides conveniently sized image which may serve multiple purposes.

PART II

Introduction

The Soil Conservation Service (SCS) has a goal of mapping all soils in the United States by the 1990s. Only about half of the U.S. land area has been mapped, with large portions of the unmapped regions lying in vast, remote semi-arid and arid regions.

Much attention, therefore, is focused on the use of remotely sensed Landsat MSS data as a tool to facilitate the mapping process (Imhoff and Petersen, 1980). Multi-temporal Landsat coverage over the same location provides more information than any single data (Mimms, 1982).

Landsat data is limited since it can only delineate surfaces with differing reflectances in the visible and near-infrared wavelengths. Landsat data when combined with other data types such as radar (Eyton, 1979) and elevation (Turner, 1979), provides increased surface terrain information.

HCMM thermal-infrared data offers unique surface terrain information not contained within Landsat or Digital Terrain Elevation data (DTE). Combination of Landsat, HCMM and DTE may prove highly beneficial in surface terrain analysis (Figure 22).

Objectives

The specific objectives of this study are to:

1) geometrically rectify Landsat, Heat Capacity Mapping Mission (HCMM) and Digital Terrain Elevation (DTE) data to a common base map projection and digitally combine the cartographically registered data sets; and

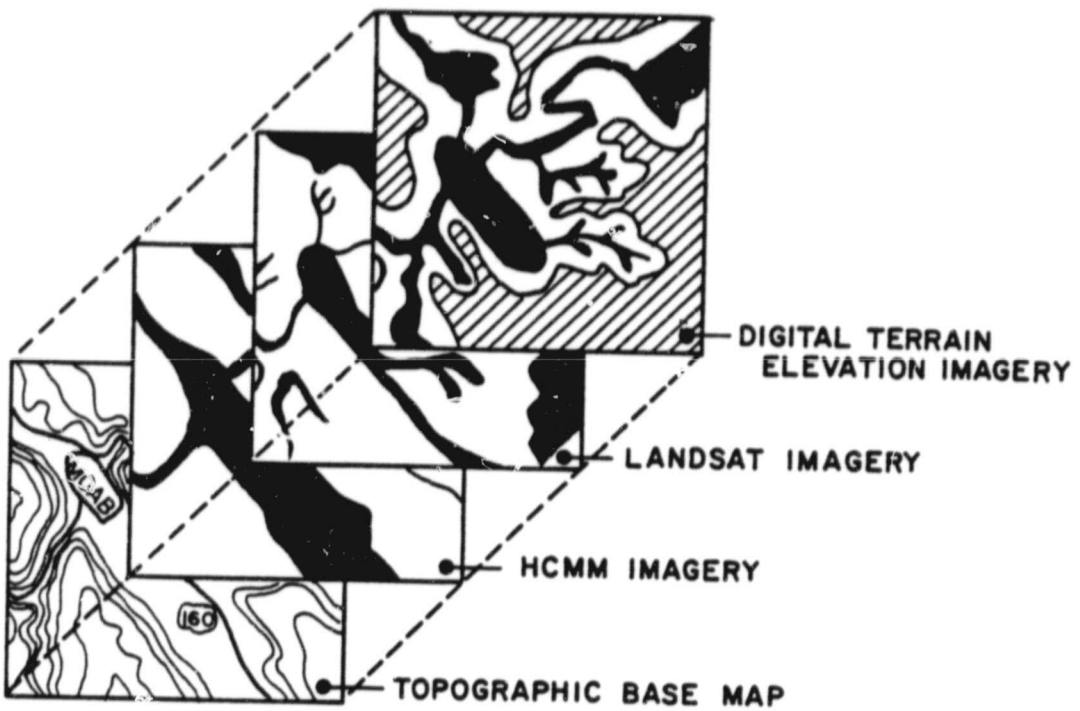

Figure 22. Diagram illustrating the conceptual overlay of HCMM, Landsat and DTE data sets

2) measure correlations between Landsat, HCMM and DTE data and compare the informational content of Landsat data alone with combined Landsat, HCMM and DTE data for surface terrain analysis in arid and semi-arid regions.

Study Site

The Moab study area is located in Grand County in east-central Utah (Figure 1) and lies within 38°30' - 38°45' north latitude and 109°15' - 109°37'30" west longitude. The Moab site is centered within the region described in Part I and consists of approximately 82,300 hectares (203,200 acres). Plate 1 illustrates the site in detail and references areas mentioned in subsequent discussions. Detailed descriptions of site characteristics are contained in Part I.

Project Data

HCMM, Landsat and Digital Terrain Elevation (DTE) digital data sets, map data and photographic data were used in the analysis. HCMM data consisted of a five-channel 12 MAY 78 (#AA0016-20370) scene containing the following channels.

- Daytime Visible (DAY-VIS) — broadband visible and near-infrared
- Daytime Temperatures (DAY-IR) — daily maximum temperature
- Nighttime Temperatures (NIGHT-IR) — daily minimum temperatures
- Temperature Difference (TEMP-DIFF) — diurnal temperature difference
- Apparent Thermal Inertia (ATI) — measure of the ability of a material to resist temperature change

ATI data is calculated from the following expression:

$$ATI = c(1-a)/(T)$$

where: c is a scaling factor

a is apparent albedo (determined from DAY-VIS)

T is diurnal temperature difference (TEMP-DIFF)

Landsat-2 data consisted of a four-channel 13 May 76 scene (#2477-17142). Digital Terrain Elevation (DTE) data consisted of elevation values corresponding to the 1:250000 USGS Moab topographic quadrangle. The sampling grid of DTE represents 60.9 meters on the ground.

Ancillary data such as geologic maps, soils maps, black and white aerial photographs, and orthophotoquads were also used primarily for ground-truth. A 1:250000 USGS Moab quadrangle was used as a common base map to register the Landsat, HCMM and DTE digital data sets.

Procedures

Reformatting

Preprocessing involved the selection and acquisition of HCMM, Landsat and Digital Terrain Elevation (DTE) digital data sets followed by reformatting of the raw data into ORSER band-interleaved-by-line (BIL) format. Each of the three data types were eventually output to 6250 BPI magnetic tapes with 8-bit binary (0-255) pixel representation.

Landsat

A false color composite of the 13 MAY 76 Landsat scene overlaid with a calibrated grid determined scan line and element coordinates defining the study site whose area spanned two files of the data tape. SUBSET program was executed twice to format the data from each file onto a separate ORSER format tape. SPAN program joined the two portions of the study site onto a single file.

The 13 May 76 Landsat scene corresponds to the date of maximum vegetative cover in the area. The vegetation is sparse in most areas except the higher elevation forested regions. Two prior studies successfully used this Landsat scene (Mimms, 1982; Imhoff and Petersen, 1980) to evaluate the feasibility of using Landsat data as an aid to soil mapping in desert regions.

Heat Capacity Mapping Mission (HCMM) Data

The 12 MAY 78 HCMM data set used in Part I was selected primarily because its overpass data closely matched the 13 MAY 76 Landsat scene. One of the goals was to evaluate statistical relationships between Landsat and HCMM data. Therefore, similar surface conditions at the times of data collection will avoid confusion associated with changes in vegetative cover.

Scan line and element coordinates delineating the study site were obtained from contrast-stretched hardcopy DAY-IR imagery. SUBSET.HCMM program reformatted data covering the selected study area for each of the five HCMM channels.

The five HCMM channels were then merged onto a single ORSER format tape creating a five channel (BIL) data set using MERGE

program. Merging allowed for future cartographic corrective transformation equations to be applied to all five channels at once rather than individually.

Digital Terrain Elevation (DTE) Data

USGS Digital Terrain Elevation (DTE) data was obtained from the National Cartographic Information Center (NCIC) in Reston, Virginia. Gridded elevation values in feet corresponded to the entire western half of the 1:250000 scale USGS Moab topographic quadrangle. RFMTDTT program reformatted the entire data set and scaled the binary pixel values (0-255) such that they represented elevations ranging from 1158 to 3657 meters. This range was derived from minimum and maximum elevations within the study site obtained from the Moab topographic map. Scan lines on raw DTE data sets are oriented south to north and begin at the western border of the topographic map.

Cartographic Correction

Spatial registration of Landsat, HCMM and DTE digital data was necessary to analyze statistical relationships between the three data types. Each data type was first rectified with a USGS 1:250000 scale topographic map of the Moab quadrangle, which was selected as a base map. The map was assigned an origin in its northwestern corner with each axis scaled such that 40 units or pixels occurred per inch. Therefore, any data set when enlarged five times would overlay exactly onto the base map since resolution of the Versatec plotter equals 0.0127 cm. Each data set, once rectified with the base map, was therefore, mutually registered with the other digital data sets. Data

sets were not directly registered to each other because of the inability to locate many good common control points on contrast enhanced imagery, a common problem with data of dissimilar scale and properties. The topographic base map provided numerous control points common to all data types and served as a good base for geographic reference for subsequent image interpretation. Cartographic correction procedures described in Part 1 were followed in each registration.

Landsat

Rectification of the Landsat data to the topographic base map involved a two stage procedure. Geometric distortions common to all Landsat MSS raw data sets were first removed using numerical modelling techniques. Empirical rubber sheet stretching then precisely transformed the data to conform accurately with the base map.

Several types of geometric distortion are contained within raw Landsat data (Turner et al., 1982). Scale differential results from spatial overlap of pixels along each scan line producing a non-square pixel that can be represented by a 56 meter x 79 meter rectangle. Eastward rotation of the earth beneath the satellite skews the image about five miles from square at the bottom of a scene, forming a parallelagram. Orbital alignment characteristics produce data oriented approximately 13° clockwise from north. Geometric correction models designed to remove these known distortions were applied to the 4-channel Landsat data set using matrix transformations available in SUBGM program. Output was directed to magnetic tape from which contrast-stretched grey level images were produced.

Control points (28) were selected and digitized from the Landsat imagery and base map. Streams and river bends were primary control point features. EZLS program generated third order transformation functions that were entered into SUBGM.HCMM to transform the data set. WARP program showed non-linear distortion primarily along vertical columns of pixel and general overall rotation of the data set. Grey level plots of the transformed data set produced on the Versatec plotter with a scale factor of 5.0 conformed accurately to the topographic base map.

Heat Capacity Mapping Mission (HCMM)

Transformation equations discussed in Part 1 to rectify HCMM data set to a 1:250000 base map were applied to the 12 MAY 78 five channel data set using SUBGM.HCMM program. Temperature dependence among spatially local pixel groups prompted the use of cubic convolution resampling techniques. Cubic convolution, therefore, assumes that the temperature at a given pixel location is influenced by the temperatures of neighboring pixels. Enlarged Versatec grey level plots of the transformed data set overlaid accurately onto the topographic base map.

Digital Terrain Elevation (DTE)

The orientation of a DTE data sets varies randomly about north even though produced from north oriented USGS topographic maps. Misalignment of the topographic source map during the digitization procedure causes the rotation. The four corners of the topographic base map defining the data set and their corresponding location on Versatec grey level plots of the DTE data were digitized. SAS

programs developed linear (rotation and scaling) transformation functions that were used in SUBGM.HCMM program to transform the DTE data set. An alternative procedure would have been to measure the angle of rotation directly from grey level plots of the entire data set, since the source map boundaries are clearly delineated against a background of pixels assigned a grey level of black. Neither method, however, involved location of surface terrain control points.

Principal Components Analysis (PCA)

Principal components analysis (PCA) is a linear orthogonal transformation that when applied to an n-dimensional data set produces another n-dimensional data set with totally independent axes and components. The total variance contained in the original set of axes is retained on the new components; therefore, there is no loss of information (Merembeck and Borden, 1978).

The first principal component explains as much of the original total variance or information that can be explained on a single axis. The second component, orthogonal to the first, explains as much of the remaining unexplained variance that can be explained on a single axis, and so on until all of the original variance is explained.

There are several advantages to principal components analysis that are applicable to this project. Basic statistical parameters such as channel variance, channel means and correlations are generated that are useful for channel informational comparisons.

PCA can be used to reduce the dimensionality of the original data set. For example, over 97 percent of the total variance in an 8-channel Landsat data set may be preserved on the first three PCA

axes (Mimms, 1982). Processing and production cost can be signifi cantly reduced without losing interpretable information. The ability to explain 95-98 percent of the original variance on the first three components also is suitable for the production of three-layer color composites where each component is assigned a subtractive primary color (Eyton, 1982).

Statistics known as loadings are output from PCA and reveal correlations of the original channels with each principal component axis. Component loadings yield data quantifying the redundancy of information contained on the original channels as well as the relative importance of the original channels (Merembeck and Borden, 1978).

The specific PCA procedure began with MERGE program which combined the individual Landsat, HCMM and DTE data sets into one 10-channel data set. Since the data sets resided on three separate magnetic tapes, it was a two-step process. The Landsat (channels 1-4) were first combined with the DTE data (channel 5) forming a 5-channel data set which was subsequently merged with the HCMM data set (channels 6-10).

STATS program was used to standardize the data set such that each channel had the same mean and variance. This eliminated any bias due to channel scaling.

Several PCA transformations were performed using different channel combinations. In each case, STATS program generated the transformation matrix. HISTRAN program used the matrix to determine the possible range of data values associated with each resulting principal component axis prior to the actual transformation. Scaling and translation parameters were calculated based on the range such

that each output component would be scaled from 0-255. SUBTRAN program used the transformation matrix plus the scaling and translation parameters to transform the data set to principal components space.

Color Composites

Photographic color composites graphically displayed the combined information contained on the first three high order axes of each principal components transformation. The color composite allowed qualitative comparison of the total surface terrain information contained within each of the original combined data sets through color photographic enhancement.

The multi-stage technique takes information contained within a digital data set and by the use of subtractive primary color mixing theory (Eyton, 1982), produces photographic color products. Enlarged (200%) Versatec electrostatic contrast-enhanced grey level plots were generated for each of the three high-order or major principal components axes. Each image was photographically reduced and developed onto Kodalith ortho-film using a large format copy camera to generate black and white film negatives. The film negatives were then overlaid onto cyan, magenta, and yellow negative acting 3M Color Key in a vacuum frame and exposed to a strong ultraviolet light source in a platemaker. The light sensitive Color Key emulsion was hardened wherever the negative was clear. Color Key Hand Developer removed the emulsion from areas not exposed to light revealing a color toned positive of the original electrostatic grey level plot. The three subtractive primary color films were overlayed and registered.

Each color composite was overlaid on a light table and photographed using Ektachrome 160 tungsten film. Photographing the light transmitted through the color composite improved contrast between colors.

Results and Discussion

Landsat

Correlations between all four Landsat bands are extremely high indicating much redundancy between channels (Table 8). Individual Landsat band grey-level maps showed remarkedly similar patterns. Bare, sandstone-derived soils and sandstone bedrock consistently reflected higher in all bands compared to vegetation. Spatial signatures of bare soils and bedrock were derived from cluster analysis using CLUS program. Curves of mean pixel response over four Landsat bands showed parallel signatures discriminated only by overall magnitude differences over all channels. Spectral responses resemble "iron affected" soils described by Stoner and Baumgardner (1981). Such soils typically have less than 2.0% organic matter content, less than 1% iron oxide content and good natural drainage, all typical of study site soils.

Principal components analysis (PCA) further illustrates informational redundancy in the Landsat data (Figure 23). The first principal component axis accounts for 94.04% of the total variance contained in the data set (Table 9). All four channels load highly on the first component (Table 10) producing an axis essentially measuring overall scene brightness. The remaining variance load mostly on the second and third principal component axes. Principal component three

Table 8. Correlation matrix of the 4-channel Landsat data set

	Landsat Band 1	Landsat Band 2	Landsat Band 3	Landsat Band 4
Landsat Band 1	1.00			
Landsat Band 2	0.93	1.00		
Landsat Band 3	0.91	0.96	1.00	
Landsat Band 4	0.84	0.90	0.97	1.00

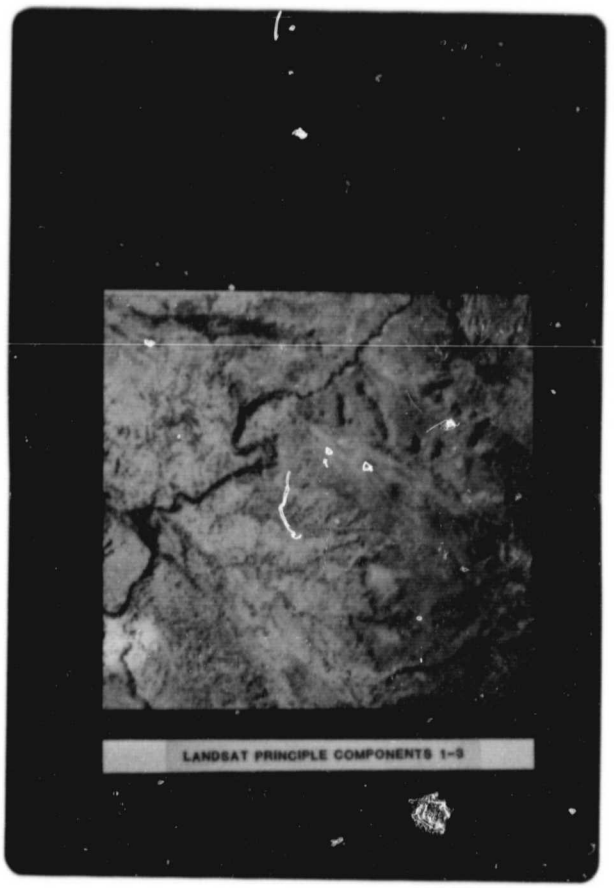

Figure 23. Contrast-stretched color composite produced from principal components 1-3 from the 4-channel Landsat data set.

Table 9. Eigenvalues and associated percentages for the principal components axes from the 4-channel Landsat data set

	Axes			
	1	2	3	4
Eigenvalue	3189.12	143.03	46.23	12.73
Percentages	94.04	4.22	1.36	0.38

Table 10. Correlation matrix of the individual channels of the Landsat data set and principal components axes

	Axes			
	1	2	3	4
Landsat Band 1	0.94	-0.29	0.16	0.01
Landsat Band 2	0.98	-0.13	-0.16	0.04
Landsat Band 3	0.99	0.08	-0.03	-0.10
Landsat Band 4	0.96	0.27	0.07	0.05

delineates residual soils in Professor Valley (yellow) derived from Cutler formation sandstone which is the oldest geologic deposit found in the area. Irrigated fluvial sandstone and shale deposits are delineated in Castle Valley and Spanish Valley as well as eolian sands in Fisher Valley. Topographic variability is generally well defined. Narrow tributary canyons of the Colorado River and mesa boundaries in the La Sal Mountains are separable.

Landsat and DTE

The correlation matrix for a five channel data set consisting of four Landsat channels and a Digital Terrain Elevation (DTE) channel appears in Table 11. Correlations between DTE data and each of the four Landsat bands are negative because scene brightness tends to increase at lower elevations due to decreasing vegetative cover. None of the four Landsat bands alone explains more than 20% of the variance contained within the DTE band suggesting that the DTE channel contains topographic information unique to any individual Landsat band. Elevation contours (152 meters) on Figure 24 illustrates the magnitude of topographic variability over the study site as well as DTE pixel resolution. A digitizing error in the original DTE data causes the vertical line observed just east of Moab.

Principal components analysis (PCA) further evaluates statistical relationships between Landsat and DTE data sets. The first high order principal component axis explains 78.28% of the total variance in the original five channels (Table 12). The axis represents overall image brightness with all four Landsat bands loading highly (Table 13). Contrast enhanced images of this axis show trends almost identical to

Table 11. Correlation matrix of the 5-channel combined Landsat/DTE data set

	Landsat Band 1	Landsat Band 2	Landsat Band 3	Landsat Band 4	DTE
Landsat Band 1	1.00				
Landsat Band 2	0.93	1.00			
Landsat Band 3	0.91	0.96	1.00		
Landsat Band 4	0.84	0.90	0.97	1.00	
DTE	-0.29	-0.46	-0.42	-0.40	1.00

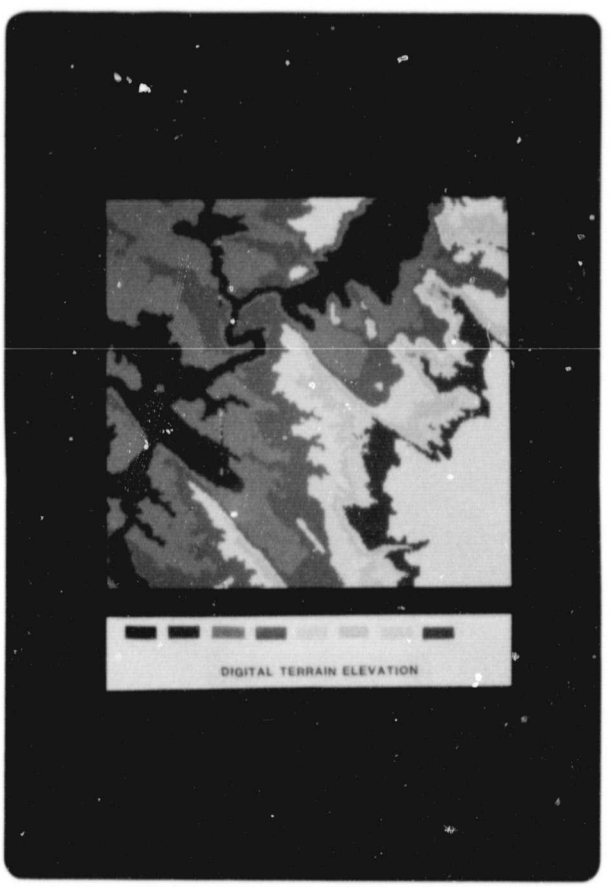

Figure 24. Contour map (150 meter intervals) produced from Digital Terrain Elevation (DTE) data

Table 12. Eigenvalues and associated percentages for the principal components axes from the combined Landsat/DTE data set

	Axes				
	1	2	3	4	5
Eigenvalue	3399.33	753.84	141.09	35.38	12.68
Percentage	78.28	17.36	3.25	0.81	0.29

Table 13. Correlation matrix of the individual channels of the combined Landsat/DTE data set and principal components axes

	Axes				
	1	2	3	4	5
Landsat Band 1	0.92	-0.25	-0.27	0.14	0.00
Landsat Band 2	0.98	-0.07	-0.14	-0.14	0.04
Landsat Band 3	0.98	-0.12	0.08	-0.03	-0.10
Landsat Band 4	0.95	-0.12	0.27	0.05	0.05
DTE	-0.53	-0.85	0.02	-0.02	0.00

the first PCA axis of the four-channel Landsat data set. The second PCA explains 17.36% of the original total variance and is highly correlated with elevational data. Over 64% of the variance contained in the DTE data set is represented on this axis. Contrast enhanced imagery of this axis delineates escarpments of mesas and plateaus surrounding Spanish and Castle Valleys which are not clearly distinguished in Landsat imagery. The third PCA accounts for 3.25% of the total original variance representing a contrast between visible (green, red) and near-infrared Landsat bands. The unusually high near-infrared reflectance of bare soils in this study area discounts the typical interpretaton that such a contrast measures vegetation. Contrast enhanced imagery of this axis highlights shaded areas common to the extensive network of canyons and steeply sloping west facing slopes along edges of mesas.

A color composite (Figure 25) made from the first three high order PCA axes displays 98.9% of the total variance contained in the original combined Landsat and DTE five channel data set. The enhanced delineation of plateau and mesa escarpments is a striking improvement over the four channel Landsat color composite (Figure 24). The southeastern valley walls of Spanish and Castle Valleys, although over 300 meters above the valley floors, were not clearly delineated using Landsat data alone (Figure 23). The improved topographic clarity offered by DTE certainly aids soils interpretation of image products because of the important topographic component associated with soil formation.

Additional independent variance offered by DTE data reduces the total variance explained by the first three PCA axes from 99.62% in

Figure 25. Contrast-stretched color composite produced from principal components 1-3 from the combined Landsat/DTE Data Set.

the Landsat four-channel analysis, to 98.9% in the combined analysis. Some information will, therefore, be lost using color composites generated from the first three high-order axes. In this case, Cutler Formation sandstone-derived soils in Professor Valley, which were defined on PCA axis number 3 of the 4-channel Landsat data, are less distinct.

HCMM

Table 14 shows the correlation matrix for the entire five channel HCMM data set. The DAY-VIS (Figure 26) channel is not highly correlated with any of the other four HCMM channels. Topographic variability over the study site is probably masking any subtle relationships. The blocky appearance of the DAY-VIS image is due to resampling using nearest-neighbor techniques rather than cubic convolution which was used for all other channels. Daytime temperatures (DAY-IR) are directly correlated with nighttime temperatures (NIGHT-IR), probably controlled by elevation as observed over larger areas in Part I. Comparisons of DAY-IR (Figure 27) and NIGHT-IR (Figure 28) contrast-enhanced color images illustrate strong elevational related temperature gradients from the peaks of the La Sal Mountains (black) down to valley floors. The Colorado River is relatively cool during the daytime and warm at night owing to the high specific heat capacity of water. Steep northeastern facing slopes on escarpments along Castle and Spanish Valleys are relatively cool compared to flat lying adjacent surfaces.

Daytime temperatures correlate even higher with diurnal temperature differences (TEMP-DIFF) as can be seen when Figures 27 and 29 are compared. Low thermal diffusivities of dry base desert soils result

Table 14. Correlation matrix of the 5-channel HCMM data set

	HCMM DAY-VIS	HCMM DAY-IR	HCMM NIGHT-IR	HCMM TEMP-DIFF	HCMM ATI
HCMM DAY-VIS	1.00				
HCMM DAY-IR	-0.16	1.00			
HCMM NIGHT-IR	-0.12	0.77	1.00		
HCMM TEMP-DIFF	-0.19	0.89	0.41	1.00	
HCMM ATI	0.16	-0.89	-0.53	-0.93	1.00

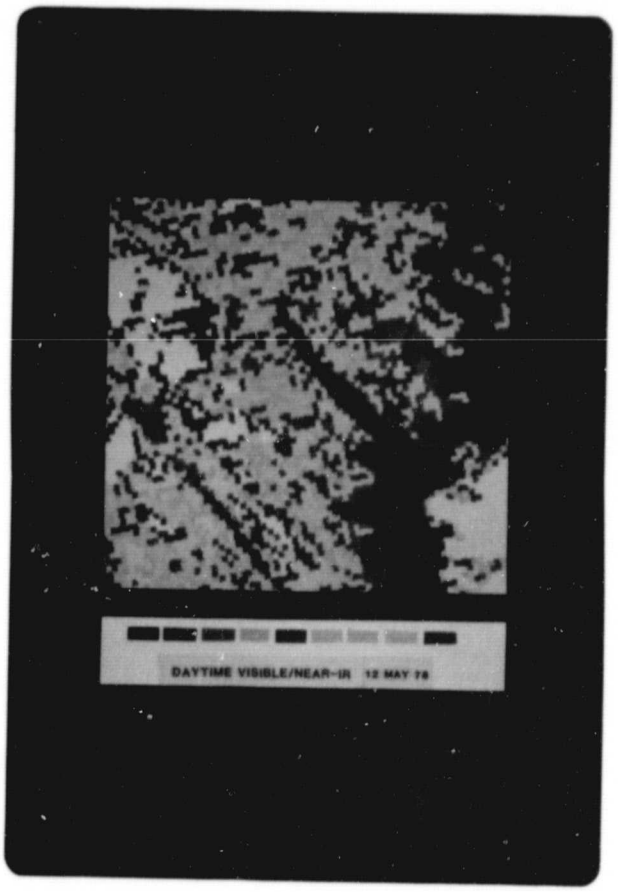

Figure 26. Contrast-stretched HCMM 12 May 1978 DAY-VIS image showing a gradient from minimum (Black) to maximum (White) surface reflectance.

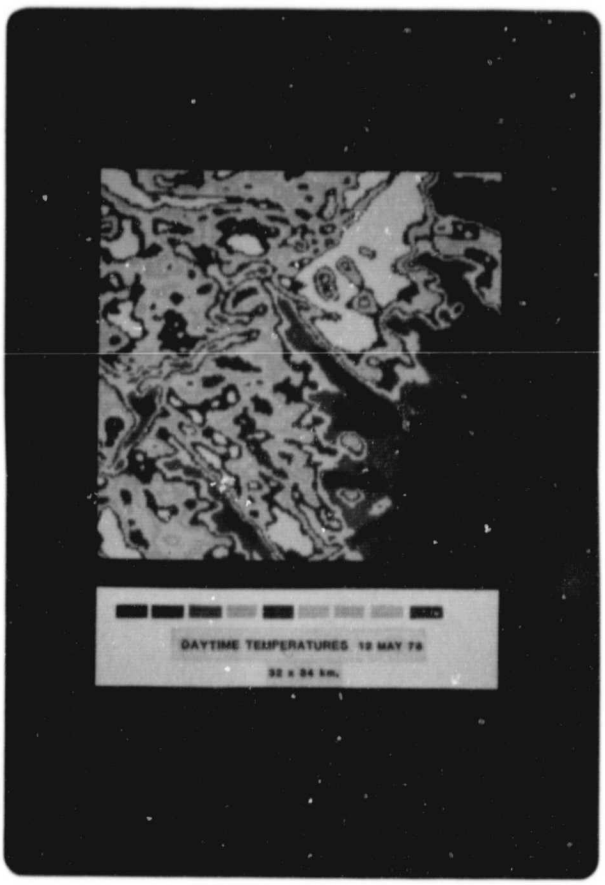

Figure 27. Contrast-stretched HCMM 12 May 1978 DAY-IR image showing a gradient from minimum (Black) to maximum (White) daytime surface temperatures.

Figure 28. Contrast-stretched HCMM 12 May 1978 NIGHT-IR image showing a gradient from minimum (Black) to maximum (White) nighttime surface temperatures.

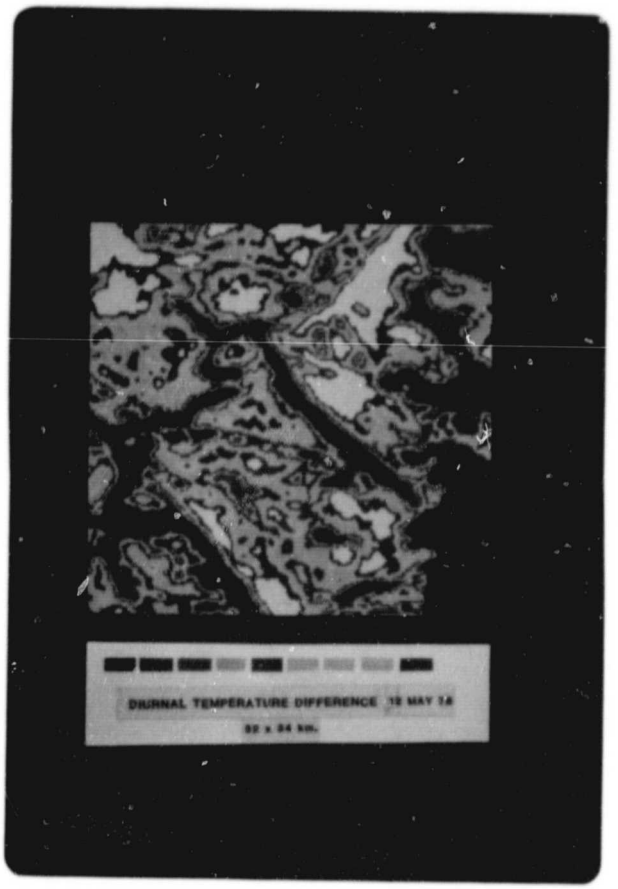

Figure 29. Contrast-stretched HCMM 12 May 1978 TEMP-DIFF image showing a gradient from minimum (Black) to maximum (White) diurnal temperature fluctuations.

in high daytime surface temperatures and proportionately low nighttime temperatures (Oke, 1978). Material density differences between bedrock and deep sandy soils are probable causes of TEMP-DIFF variability in lower elevations with the exception of streams rivers, and irrigated ranches. Increased moisture and vegetative cover dampens diurnal fluctuations at nigher elevations through increased evaporative cooling and higher thermal inertias. Northeastern facing slopes, which were relatively cool during the daytime, contrast strongly with adjacent level surfaces by exhibiting low diurnal temperature fluctuations compared to adjacent level surfaces.

Apparent thermal inertia (ATI) is inversely correlated highly with all but the DAY-VIS channel. Color imagery (Figure 30) of ATI shows patterns closely resembling those on DAY-IR, NIGHT-IR and TEMP-DIFF imagery but with an inverted color sequence. Apparent thermal inertia is lowest for the dry, deep sands valley between soils in Professor Valley and Spanish Valley which exhibited large diurnal temperature fluctuations. Waters and canyons of the Colorado River have high apparent thermal inertia values equalled only by northeast facing escarpments previously discussed along Castle and Spanish Valley.

Principal components analysis (Figure 31) was performed using the DAY-IR, NIGHT-IR, TEMP-DIFF and ATI HCMM channels. The first high order principal component axis (Table 15) accounts for 80.74% of the total original variance and is highly correlated with all four channels (Table 16). Individual grey level plots shows overall topographically controlled temperature gradients clearly delineating

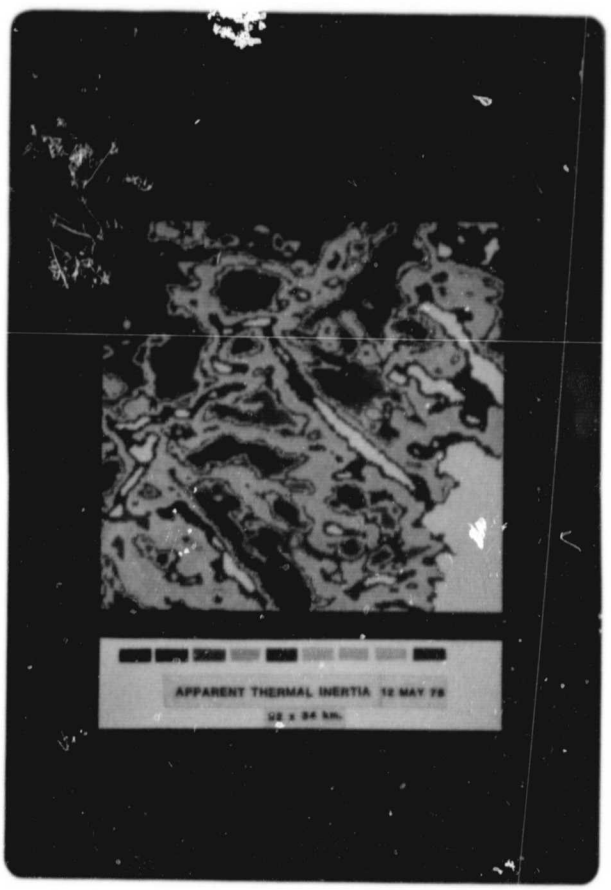

Figure 30. Contrast-stretched HCMM 12 May 1978 ATI image showing a gradient from minimum (Black) to maximum (White) apparent thermal inertia.

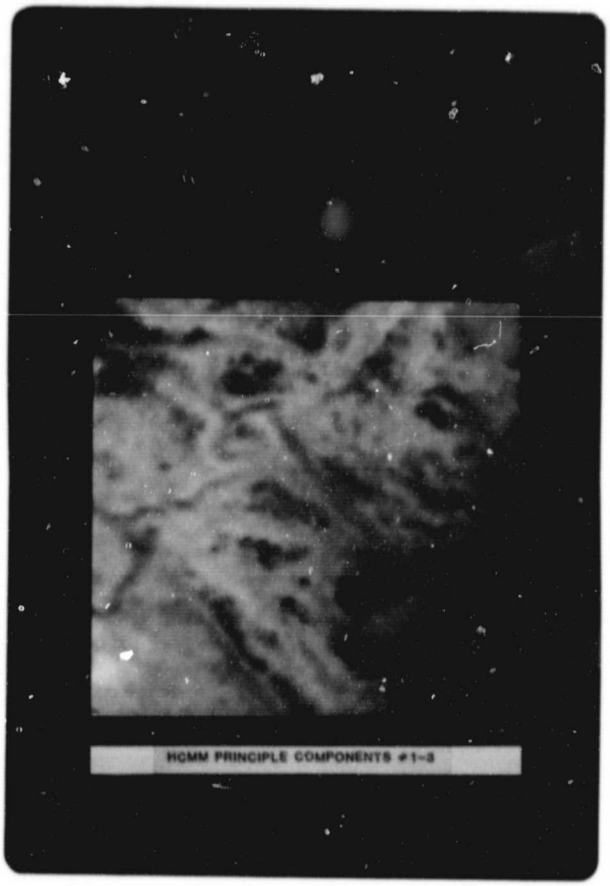

Figure 31. Contrast-stretched color composite produced from principal components 1-3 from the HCMM data set.

Table 15. Eigenvalues and associated percentages for the principal components axes from the HCMM data set

	Axes			
	1	2	3	4
Eigenvalue	2765.95	596.57	57.71	5.61
Percentage	80.74	17.41	1.68	0.16

Table 16. Correlation matrix of the individual channels of the HCMM data set and principal components axes

	Axes			
	1	2	3	4
HCMM DAY-IR	0.99	0.06	-0.10	-0.06
HCMM NIGHT-IR	0.74	0.67	0.02	0.03
HCMM TEMP-DIFF	0.91	-0.40	-0.10	0.05
HCMM ATI	-0.94	0.25	-0.23	0.01

cool northern aspects as well as typical elevation trends. Principal component number 2 explains 17.41% of the total variance. This axis apparently represents a contrast between original NIGHT-IR and TEMP-DIFF channels. The Colorado River, for example, which is warm at night with little diurnal temperature change, contrasts with Castle Valley which is cooler at night and exhibits large diurnal temperature variability. The third principal component explains only 1.68% of the total original variance and delineates areas with highest apparent thermal inertia.

Color composites (Figure 31) of the three high order principal component axes explain 99.84% of the total variance contained in the original four channel data set. General elevational trends are evident by contour bands surrounding the La Sal Mountains. Outlines of high plateau and mesa escarpments are clearly delineated. Southern aspects on Adobe Mesa and Fisher Mesa in Professor Valley highly contrast northerly aspects on the same two mesas as well as valley escarpments along Castle Valley. Southern aspects are relatively hot with high diurnal variability whereas northern aspects are relatively cool with little diurnal variability. Northerly aspects and the Colorado River canyon show similar responses. Delineations in Professor Valley and Spanish Valley are associated with relatively hot soils with large diurnal variability.

Landsat/HCMM

The correlation matrix for a nine-channel data set consisting of four Landsat bands and five HCMM bands appears in Table 17. The HCMM DAY-VIS channel, is sensitive to a range of wavelengths (10.5 - 12.5 microns) almost encompassing all four Landsat channels. It seems

Table 17. Correlation matrix of the combined 9-channel Landsat/HCMM data set

	Landsat Band 1	Landsat Band 2	Landsat Band 3	Landsat Band 4	HCMM DAY-VIS	HCMM DAY-IR	HCMM NIGHT-IR	HCMM TEMP DIFF	HCMM ATI
Landsat Band 1	1.00								
Landsat Band 2	0.93	1.00							
Landsat Band 3	0.91	0.96	1.00						
Landsat Band 4	0.84	0.90	0.97	1.00					
HCMM DAY-VIS	0.58	0.52	0.52	0.48	1.00				
HCMM DAY-IR	0.18	0.38	0.35	0.34	-0.16	1.00			
HCMM NIGHT-IR	0.28	0.43	0.39	0.36	-0.12	0.77	1.00		
HCMM TEMP-DIFF	0.05	0.22	0.21	0.22	-0.19	0.89	0.41	1.00	
HCMM ATI	-0.10	-0.27	-0.25	-0.27	0.16	-0.89	-0.53	-0.93	1.00

reasonable then that positive correlations are almost equal across all four Landsat bands. Each Landsat channel explains about 25% of the variance in the HCMM DAY-VIS channel although not implying that each portion of the explained variance is unique to each channel. Daytime and nighttime temperatures are moderately correlated with Landsat reflectance data especially in the red and near-infrared bands. The relationship probably reflects the overall elevational variability across the landscape. High temperature as well as bright surfaces are associated with lower landscape positions low soil moisture and sparse vegetation whereas both temperature and reflectance decrease proportionately with increasing elevation. The correlation of surface temperature with reflectance, therefore, does not reflect a cause and effect relationship in this particular situation.

Correlations between all four Landsat bands, diurnal temperature difference (TEMP-DIFF) and apparent thermal inertia (ATI) are low with less than 10% common variance in each case. Material density effects in low lying areas may be controlling diurnal temperature variability more so than albedo. The albedo would be correlated higher with diurnal temperature change if moisture was the controlling factor. In areas such as Moab Valley for example, moisture reduces diurnal temperature fluctuations as well as surface reflectance.

Principal components analysis (Table 18) of the nine-channel Landsat and HCMM combined data set loaded 92.14% of the total original variance on the first three axes. The reduction in total variance on the first three PCA axes compared to the 3 high order HCMM or Landsat PCA aces alone is evident by the lack of detail on the color composite (Figure 32).

Table 18. Eigenvalues and associated percentages for the principal components axes from the combined Landsat/HCMM data set

	Axes								
	1	2	3	4	6	7	8	9	10
Eigenvalue	4040.96	2370.73	608.20	359.89	129.99	58.80	33.26	11.89	5.03
Percentage	53.04	31.12	7.98	4.72	1.71	0.77	0.44	0.16	0.07

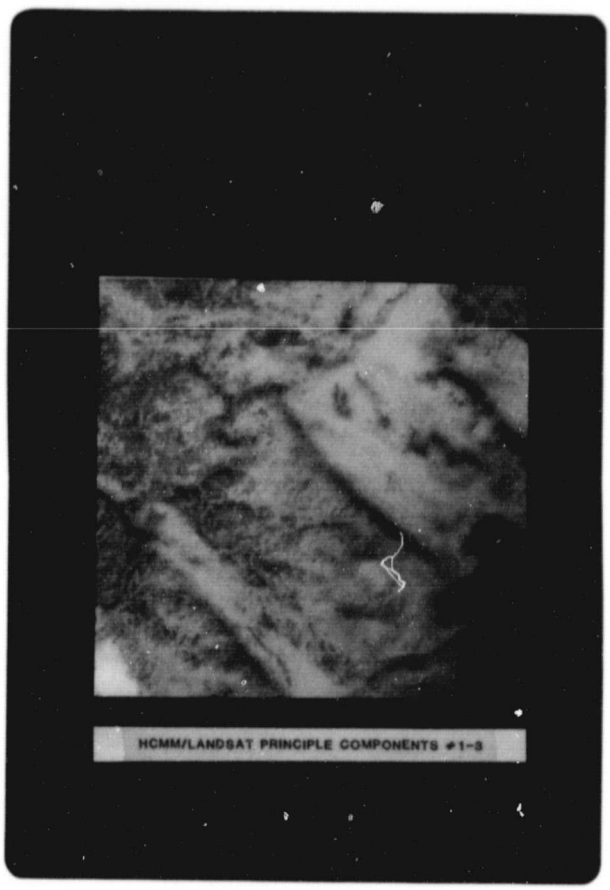

Figure 32. Contrast-stretched color composite produced from principal components 1-3 from the combined Landsat/HCMM data set.

Table 19. Correlation matrix of the individual channels of the combined Landsat/HCMM data set and principal component axes.

	Axes								
	1	2	3	4	5	6	7	8	9
Landsat Band 1	0.80	-0.51	-0.04	-0.08	-0.26	-0.05	0.14	-0.00	-0.00
Landsat Band 2	0.91	-0.34	-0.05	-0.06	-0.14	0.02	-0.13	-0.04	0.00
Landsat Band 3	0.91	-0.37	-0.01	-0.13	0.07	0.03	-0.03	0.09	0.00
Landsat Band 4	0.88	-0.34	0.01	-0.19	0.25	-0.02	0.05	-0.05	-0.00
HCMM DAY-VIS	0.38	-0.66	0.36	0.54	0.05	0.01	0.00	-0.00	0.00
HCMM DAY-IR	0.69	0.71	-0.01	0.11	-0.01	0.10	0.02	-0.00	-0.05
HCMM NIGHT-IR	0.63	0.43	-0.59	0.26	0.03	-0.02	0.01	0.00	0.03
HCMM TEMP DIFF	0.53	0.74	0.38	-0.06	-0.04	0.10	0.02	-0.00	0.04
HCMM ATI	-0.59	-0.73	-0.27	-0.01	-0.01	0.23	0.03	-0.01	0.01

The first high order PCA axis explains 53.04% of the total variance of the original nine channels. The four Landsat bands load highest with more moderate loadings by the five HCMM channels (Table 19). HCMM DAY-VIS channel is least correlated with the PCA axis. Contrast enhanced imagery of PCA axes number 1 shows overall mean pixel brightness gradients with good delineation of topographic changes along north facing slopes.

The second high order PCA axis accounts for 31.12% of the original total variance and represents a contrast between surface reflectance in the visible through near-infrared wavelength, and surface temperature magnitude and diurnal variability. Soils in Spanish Valley and Professor Valley show high daytime temperatures, large diurnal fluctuations and relatively moderate surface reflectance in the visible and near-infrared wavelengths. These areas are contrasted with the snow covered La Sal Mountains which are uniformly cold but are extremely reflective. Topographic content is high on this axis with considerable delineation of narrow canyons as well as aspect differences.

The third higher order PCA axis explains 7.98% of the total original variance. Component loadings suggest separation of surfaces which have relatively low reflectances and diurnal temperature fluctuations but relatively high nighttime temperatures. Contrast enhanced imagery clearly delineates the deep Colorado River canyon and steep sloped northeast facing slopes of valleys and mesas.

Landsat/HCMM/DTE

Four Landsat channels, five HCMM channels and one DTE channel were registered and merged thereby creating a 10-channel data set whose correlation matrix appear in Table 20. Correlations between and within Landsat and HCMM channels were previously discussed as well as relationships between Landsat and DTE. This section, therefore, concentrates on correlations between HCMM and DTE data channels.

DTE and surface brightness as measured by the HCMM DAY-VIS channel show extremely low correlation. Significant quantities of snow cover in the La Sal Mountains on the 12 May 78 scene (Figure 26) produce abnormally high reflectance at maximum elevations. This climatic anomaly somewhat masks an overall trend of brightness reduction in the HCMM DAY-VIS channel at higher elevations associated with increased vegetative cover.

Both DAY-IR and NIGHT-IR are highly correlated with DTE as expected over terrain with such large elevational gradients. However, approximately 20% of the variance in both the DAY-IR and NIGHT-IR data sets is unexplained by use of DTE alone. Other factors, such as moisture, aspects, slopes, density and irrigation combine to produce deviations from elevational lapse gradients. For example: 1) the Colorado River and tributary canyons at low elevations, as well as settling ponds in Moab Valley, are relatively cool during the day; 2) irrigated ranches in Professor Valley and Spanish Valley contrast with relatively hot surrounding surfaces; and 3) north-facing steep slopes and high material densities produce relatively cool daytime temperatures.

Table 20. Correlation matrix of the combined 10-channel Landsat/DTE/HCMM data set

	Landsat Band 1	Landsat Band 2	Landsat Band 3	Landsat Band 4	DTE	HCMM DAY-VIS	HCMM DAY-IR	HCMM NIGHT-IR	HCMM TEMP DIFF	HCMM ATI
Landsat Band 1	1.00									
Landsat Band 2	0.93	1.00								
Landsat Band 3	0.91	0.96	1.00							
Landsat Band 4	0.84	0.90	0.97	1.00						
DTE	-0.29	-0.46	-0.42	-0.40	1.00					
HCMM DAY-VIS	0.58	0.52	0.52	0.48	0.04	1.00				
HCMM DAY-IR	0.18	0.38	0.35	0.34	-0.91	-0.16	1.00			
HCMM NIGHT-IR	0.28	0.43	0.39	0.36	-0.89	-0.12	0.77	1.00		
HCMM TEMP-DIFF	0.05	0.22	0.21	0.22	-0.68	-0.19	0.89	0.41	1.00	
HCMM ATI	-0.10	-0.27	-0.25	-0.27	0.74	0.16	-0.89	-0.53	-0.93	1.00

TEMP-DIFF data are inversely correlated with DTE largely due to increased moisture and vegetative cover associated with higher elevations. The exceptions to this gradient are caused by the same factors causing deviations from the daytime temperature lapse rate. Factors which tend to minimize daytime surface temperatures also maximize nighttime temperatures thereby reducing daily fluctuations. Comparisons of daytime temperature (Figure 27) and diurnal temperature difference imagery (Figure 29) show very similar delineations and overall trends. Apparent thermal inertia (Figure 30) is largely a function of diurnal temperature variability and is highly correlated with elevation as well.

Principal components analysis (PCA) was performed on the 10-channel Landsat, HCMM and DTE merged data set with only 91.98% of the original total variance loading on the first three high order axes (Table 21). The first major axis accounted for 53.97% of the variance with all channels except the HCMM DAY-VIS loading highly (Table 22). Contrast stretched grey level plots of this axis are quite similar to the first axis of the 9-channel Landsat and HCMM data set and express an overall elevational gradient reflecting a transition towards increasingly higher reflectivity, daytime temperatures, nighttime temperatures and diurnal temperature variability with decreasing elevations. The trend coincides with and partially results from a climatic trend towards higher temperatures and reduced rainfall.

The second high order axis accounted for 30.25% of the original variance and closely resembles the second axis of the Landsat and HCMM nine-channel data set in the previous example. The axis appears to represent a contrast between surface reflectivity and temperature

Table 21. Eigenvalues and associated percentages for the principal components from the combined Landsat/DTE/HCMM data set

	1	2	3	4	5	6	7	8	9	10
Eigenvalue	4625.56	2592.07	664.74	402.04	130.06	61.02	45.06	32.52	11.86	5.02
Percentage	53.97	30.25	7.76	4.69	1.52	0.71	0.53	0.38	0.14	0.06

Table 22. Correlation matrix of the individual channels of the combined Landsat/DTE/HCMM data set and principal component axes.

	Axes									
	1	2	3	4	5	6	7	8	9	10
Landsat Band 1	0.69	-0.66	-0.02	0.09	0.26	-0.04	-0.06	0.13	-0.00	-0.00
Landsat Band 2	0.83	-0.52	-0.02	0.09	0.14	0.01	0.05	-0.13	-0.04	0.00
Landsat Band 3	0.81	-0.55	0.03	0.14	-0.07	0.03	0.01	-0.03	0.09	0.00
Landsat Band 4	0.79	-0.52	0.06	0.20	-0.25	-0.01	-0.02	0.04	-0.05	-0.00
DTE	-0.84	-0.42	0.24	0.17	0.01	-0.07	0.16	0.03	0.00	-0.00
HCMM DAY-VIS	0.25	-0.72	0.22	0.61	-0.04	-0.01	0.03	0.01	-0.00	0.00
HCMM DAY-IR	0.81	0.56	0.05	-0.05	0.01	0.07	0.08	0.03	-0.00	-0.05
HCMM NIGHT-IR	0.74	0.33	-0.57	-0.09	-0.03	-0.07	0.09	0.03	0.00	0.03
HCMM TEMP-DIFF	0.64	0.60	0.46	0.03	0.04	0.09	0.04	0.03	-0.00	0.04
HCMM ATI	-0.70	-0.58	-0.34	0.01	0.01	0.23	0.04	0.03	-0.01	0.01

magnitude and diurnal variability. In lower elevations, highly reflective soils with high surface temperatures and diurnal variability are contrasted sharply with soils having more moderate temperature fluctuations but higher surface reflectivity.

The third PCA axis accounts for 7.76% of the original total variance. Grey level contrast stretched imagery delineates almost identical features as the third axis of the nine-channel Landsat and HCMM merged data set in the prior example. North-facing slopes and moist areas are highlighted as the axis contrasts surfaces that exhibit low reflectivity, high nighttime temperatures and low diurnal temperature fluctuations from bright surfaces with highly fluctuating surfaces. Maximum contrast is evident on north and south-facing slopes of Fisher Mesa.

Color composites produced from the three high order PCA axes showed no significant improvement over the previous example using just Landsat and HCMM data (Figure 33). Apparently, the HCMM thermal channels account for most of the elevational information contained in a DTE channel in this instance. This does not imply that additional channels of information that can be derived from elevation data, such as slope and aspect, are redundant.

Summary and Conclusions

Landsat, Heat Capacity Mapping Mission (HCMM) and Digital Terrain Elevation (DTE) data sets were spatially registered through an intermediate 1:250000 topographic base map for a semi-arid region in east central Utah. The three data sets were digitally combined to create a ten-channel data set.

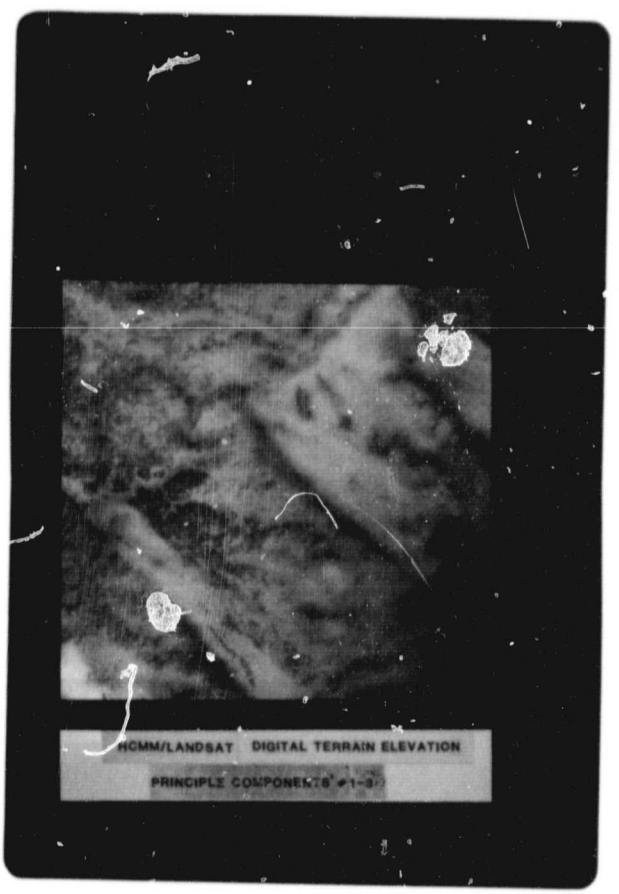

Figure 33. Contrast-stretched color composite produced from principal components 1-3 from the combined Landsat/DTE/HCMM data set.

Statistical relationships were measured between individual channels of the combined data set to determine both redundancy and independence of the individual data types. Correlations between original channels were measured, as well as correlations between original channels and principal components axes of several channel combinations.

Principal components transformation were applied to several channel combinations to reduce data set dimensionality and display as much of the original independent information as possible on three axes. Color composites were produced using photographic methods by assigning the three high order principal components axes subtractive primary colors. The technique was evaluated as a method to produce display analysis from Landsat, HCMM and DTE data combinations.

Registration of Landsat, HCMM and DTE data sets can be accurately performed using "rubber sheet stretching" techniques. The technique is simplified by registering each of the individual data types to a common 1:250000 topographic base map rather than directly to each other. This approach was used because accurate control points common to any pair of the three data types are difficult to identify.

Lack of common control points stems primarily from large resolution differences between the respective data types. Topographic base maps contain abundant control points common to HCMM, Landsat and DTE, and provide good geographic reference for image interpretation. WARP program aids control point selection and subsequent transformation model selection.

Statistical correlations among individual Landsat channels are high, indicating much redundancy of information. The same is true for a lesser extent for HCMM channels, with the exception of the DAY-VIS band, which is highly independent. DTE data correlates highly with HCMM thermal-infrared data, especially over sites with large elevational gradients. Landsat data and HCMM thermal-infrared data show extremely low correlations in regions with large elevational changes, although the relationship may increase over uniform terrain where surface albedo has more influence on surface temperature.

Principal components analysis (PCA) is a useful method to reduce the dimensionality of a large data set. Over 99 percent of the information contained in individual Landsat or HCMM data sets can be loaded on the first three PCA axes. Color composites generated from these PCA axes display the same high percentage of original channel information in a single high contrast color image. Color composites generated from combined Landsat/HCMM/DTE data sets display a lower portion of the original channel information because of increased amounts of independent information. The subtractive primary color compositing technique using three high order PCA axes is, therefore, limited by the amount of original independent information such that lower order axes need to be displayed to gather the remainder of the independent information.

Combined Landsat/HCMM/DTE data sets contains more useful surface terrain information than any individual data type. Topographic clarity of Landsat imagery can be enhanced by either DTE or HCMM data. HCMM improves delineation of cool north-facing slopes along steep

escarpments not evident in Landsat imagery alone. The independence of information between Landsat and HCMM are due to the surface properties which control the responses exhibited by each data type. Surface albedo and thermal-infrared emitters are controlled largely by different physical properties, but each offer meaningful and unique information about a rock or soil surface.

GENERAL SUMMARY AND CONCLUSIONS

Heat Capacity Mapping Mission (HCMM) thermal-infrared data were used to display the spatial distribution of diurnal surface temperatures for five dates in semi-arid east central Utah. HCMM data were used as input into a numerical model to estimate mean annual soil temperatures and annual surface temperature amplitudes.

HCMM data were spatially registered and combined with Landsat and Digital Terrain Elevation data to produce a 10-channel data set. Statistical relationships between the three data types were evaluated. Color composites were produced to graphically display the informational content of Landsat, HCMM and DTE data combinations.

Techniques were evaluated for spatial registration of HCMM, Landsat and DTE data. WARP program was developed to simplify the "rubber sheet stretching" process.

General conclusions from the analysis are:

1) HCMM thermal infrared data can be used to measure and display the spatial distribution of relative soil surface and plant canopy temperatures in arid and semi-arid regions.
2) HCMM thermal-infrared data is useful for surface terrain analysis. Surface features delineated by the data can be related to elevation, aspect, drainage, and material density.

3) Multi-temporal HCMM data sets can be accurately registered and digitally combined. WARP program improves the cartographic correction process by previewing the distortion which occurs during "rubber sheet stretching."

4) Multi-temporal HCMM and ancillary data can be used to delineate soils into groups based on their mean annual soil temperature.

5) HCMM, Landsat, and Digital Terrain Elevation (DTE) data sets can be cartographically registered and digitally overlaid to create a combined comprehensive data set for terrain analysis.

6) Combined Landsat, HCMM, and DTE data sets contain more information for surface terrain analysis than any of the three individual data types.

7) Principle components analysis loads much of the useful information contained in combined Landsat, HCMM, and DTE data sets onto three axes that can be displayed in a single color composite.

RECOMMENDATIONS

Future research efforts should be directed towards solving the difficult problem of thermal-infrared sensor calibration. In this study, HCMR sensor calibration problems excluded the use of HCMM data for absolute surface temperature measurements. The variability and uncertainties of HCMR sensor calibration throughout the duration of the HCMM project resulted in much data that provided only relative differences in surface temperatures.

Even with an accurately calibrated sensor, surface emissivity remains a difficult problem to overcome. Studies in humid and vegetated regions often reasonably assume an emissivity of 1.0 with little variation across a landscape. This assumption is invalid in desert regions and can result in serious errors in estimating surface temperatures. Desert sites with dry and sparsely vegetated surfaces can show quite low emissivity and much variability throughout a region. Future studies should be designed to determine the magnitude and variability of emissivity in deserts. Perhaps categories of rock, vegetation and soil groups which exhibit similar emissivities can be established.

Emissivity measurements useful for satellite thermal-infrared systems should be made for composite surfaces. Most studies on emissivity to date have dealt with homogeneous rock, soil or vegetative samples. Emissivities from those studies are not representative of the heterogeneous areas contained within a single pixel. Relationships such as the effect of vegetative density on emissivity need to be determined. Once surface emissivity estimates are established for

various surface categories, other types of data, such as visible or near-infrared, can be used to help classify and identify these categories prior to correction.

Besides the problems of data calibration and interpretation, the availability of diurnal thermal-infrared satellite data remains a major obstacle. The HCMM satellite provided a unique temporary opportunity to study the dynamic nature of diurnal surface temperature, with resolution unequalled by other systems. Thermal inertia mapping represents a promising method to study physical properties and process of soil but can only be accomplished with diurnal temperature data. Energy budget models to predict evapotranspiration and sensible and latent heat transfer also require diurnal temperature measurements. Therefore, it is strongly recommended that future satellite systems be designed to provide diurnal coverage at times corresponding to maximum and minimum surface temperatures, such that previously stated studies can progress.

Incorporation of multiple types of digital data into a comprehensive data base is recommended for future desert surface terrain studies and soil mapping. Thermal-infrared and digital elevation data has been shown to provide useful information when combined with Landsat data. The resolution of the HCMM satellite limited its use for soil mapping, but new systems, such as the Landsat-4 Thematic Mapper and the SPOT satellite, should provide the needed resolution. These systems combine high spatial resolution with broad spectral sensitivity that should be quite valuable for soil and geologic investigations in deserts.

Digital elevation data can be used to calculate additional channels of information related to surface topography. Slope and aspect maps can be produced accurately at any scale. Slope maps would be quite useful to separate soils initially into slope classes for soil mapping. Combination of Landsat and digital elevation data could be used to study basic environmental relationships such as vegetative surface cover and soil variability as related to aspect or slope.

LITERATURE CITED

Barnes, W. L. and J. C. Price. 1980. Calibration of a Satellite Infrared Radiometer. Applied Optics 19:2153-2161.

Bartholic, J. F., L. N. HamKen, and C. L. Wiegand. 1972. Aerial thermal scanner to determine temperatures of soils and of crop canopies differing in water stress. Agronomy Journal 64:603:608.

Blad, B. L. and N. J. Rosenberg. 1976. Measurement of crop temperature by leaf thermocouple, infrared thermometry and remotely sensed thermal imagery. Agronomy Journal 68:635-641.

Buettner, K. J. K. and C. D. Kern. 1963. Infrared emissivity of the Sahara from Tiros data. Science 142:671.

Buettner, K. J. K. and C. D. Kern. 1965. The determination of infrared emissivities of terrestrial surfaces. Journal of Geophysical Research 70:1329-1337.

Byrne, G. F., J. E. Begg, P. M. Fleming, and F. X. Dunn. 1979. Remotely sensed land cover temperature and soil water status — a brief review. Remote Sensing of Environment 8:291-305.

Byrne, G. F., K. Dabroska-Zielinska, and G. N. Goodrick. 1981. Use of visible and thermal satellite data to monitor an intermittently flooding marshland. Remote Sensing of Environment 11:393-399.

Campbell, G. S. 1977. An Introduction to Environmental Biophysics. Springer-Verlag, New York, NY.

Carlson, T. N. and F. E. Boland. 1978. Analysis of urban-rural canopy using a surface heat flux/temperature model. Journal of Applied Meteorology 17:998-1013.

Carter, B. J. and E. J. Ciolkosz. 1980. Soil Temperature Regimes of the Central Appalachians Soil Science Society of America Journal 44:1052-1058.

Cartwright, K. 1979. Tracing shallow groundwater systems by soil temperatures. Water Resources Research 10:847-855.

Cartwright, K. 1968. Thermal prospecting for groundwater. Water Resources Research 4:395-401.

Cogan, J. L. and J. H. Willand. 1976. Measurement of sea surface temperature by the NOAA 2 satellite. Journal of Applied Meteorology 15:173-180.

Commission of the European Communities Joint Research Centre. 1980. HCMM Satellite Follow-On Investigation No. 025: Soil Moisture and Heat Budget Evaluation in Selected European Zones of Agricultural and Envrionmental Interest (TELLUS Project). Ispra, Italy.

Conaway, J. and C. H. M. van Bavel. 1967. Evaporation from a wet soil surface calculated from radiometrically determined surface temperatures. Journal of Applied Meteorology 6:650-655.

DeGloria, S. D. 1982. Determining soil temperature/moisture regimes in forests and rangelands utilizing thermal remote sensing in Proceedings of Western Regional Technical Work Planning Conference of the National Cooperative Soil Survey, San Diego, CA.

Dodd, J. K. 1979. Determination of surface characteristics and energy budget over an urban-rural area using satellite data and a boundary layer model. M. S. Thesis. The Pennsylvania State University, University Park, PA.

Dutton, G. 1982. Land alive. Perspectives in Computing 2:26-39.

Egan, W. G. and G. E. Shaw. 1981. Effect of aerosols on optical remotely sensed data. in Fifteenth International Symposium on Remote Sensing of the Environment, Ann Arbor, MI.

Elmore, F. H. 1976. Shrubs and Trees of the Southwest Uplands. Southwest Parks and Monuments Association, Globe, AZ.

Eyton, J. R., R. Li, F. T. Ulaby. 1979. Combined radar and Landsat multitemporal crop classification. RSL Technical Report 360-10. The University of Kansas Center for Research, Inc., Lawrence, KS.

Eyton, J. R. 1983. Landsat multitemporal color composites. Photogrammetric Engineering and Remote Sensing 49:231-235.

Fischer, W. A., D. G. Orr, and D. D. Greenlee. 1978. An example of the merging of Landsat, topographic, and aeromagnetic data in a geologic and hydrologic study of a karst region: Claunch, New Mexico in Twelvth International Symposium on Remote Sensing of the Environment, Ann Arbor, MI.

Franzmeier, D. P., E. J. Pedersen, T. J. Longwell, J. G. Byrne, and C. K. Losche. 1969. Properties of Some Soils in the Cumberland Plateau as related to slope aspect and position. Soil Science Society of America Proceedings 33:755-761.

Fuchs, M. and C. B. Tanner. 1966. Infrared thermometry of vegetation. Agronomy Journal 58:597-601.

Fuchs, M. and C. B. Tanner. 1968. Surface temperature measurements of bare soils. Journal of Applied Meteorology 7:303-305.

Gay, L. W. and R. K. Hartman. 1981. The Surface Energy Budget of a Desert Site. School of Renewable Natural Resources, University of Arizona, Tucson, AZ.

Gray, H. L. 1968. Soil temperatures under forest and grassland cover types in northern New Mexico. USDA. Forest Service Research Note. RM-118.

Hatfield, J. L. 1979. Canopy temperatures: the usefulness and reliability of remote measurements. Agronomy Journal 71:889-892.

Heilman, J. L., E. T. Kanemasu, N. J. Rosenberg, and B. L. Blad. 1976. Thermal scanner measurement of canopy temperatures to estimate evapotranspiration. Remote Sensing Environment 5:137-145.

Heilman, J. L. and D. G. Moore. 1982. Evaluating Depth to Shallow Groundwater Using Heat Capacity Mapping Mission (HCMM) Data, Photogrammetric Engineering and Remote Sensing 48:1903-1906.

Heilman, J. L. and D. G. Moore. 1982. Evlauating near-surface soil moisture using Heat Capacity Mapping Mission data. Remote Sensing Environment 12:117-121.

Helwig, J. T. 1978. SAS Introductory Guide. SAS Institute, Inc., Cary, North Carolina.

Hendersen, C. E. and S. D. DeGloria. 1982. Characterization of slope classes for soil survey utilizing digital elevation models in Proceedings of Western Regional Technical Work Planning Conference of the National Cooperative Soil Survey, San Diego, California.

Hintz, K. F. and W. L. Stokes. 1964. Geologic map of southeastern Utah.

Hubner, G. 1981. Spectral Characteristics of Desert Surfaces unpublished report, IABG/WTH, Vicksburg, Mississippi.

Hutchinson, C. F. 1982. Techniques for combining Landsat and ancillary data for digital classification improvement. Photogrammetric Engineering and Remote Sensing 48:123-130.

Huntley, D. 1978. On the detection of shallow aquifers using thermal-infrared imagery. Water Resources Research 14:1075-1083.

Idso, S. B., R. D. Jackson, and R. J. Reginato. 1975. Detection of soil moisture by remote surveillance American Scientist 63:549-557.

Idso, S. B., T. J. Schmugge, R. D. Jackson, and R. J. Reginato. 1975. The utility of surface temperature measurements for the remote sensing of surface soil water status. Journal of Geophysical Research 80:3044-3049.

Imhoff, M. L. and G. W. Petersen. 1980. The Role of Landsat Data Products in Soil Surveys, Research Publication 105/UR, URSER, The Pennsylvania State University, University Park, Pennsylvania.

Jackson, R. D., R. J. Reginato, and S. B. Idso. 1977. Wheat canopy temperature: A practical tool for evaluating water requirements. Water Resources Research 13:651-656.

Justice, C. O., S. W. Wharton, and B. N. Holben. 1980. Application of digital terrain data to quantify and reduce the topographic effect on Landsat data. NASA Technical Memorandum 81988. Goddard Space Flight Center, Greenbelt, MD.

Kahle, A. B., A. R. Gillespie, and A. F. H. Goetz. 1976. Thermal inertia imaging: a new geologic mapping tool. Geophysical Research Letters 3:26-28.

Kocin, P. J. 1979. Remote Estimation of surface moisture over a watershed. M. S. Thesis. The Pennsylvania State University, University Park, PA.

Lammars, D. 1982. USDA Soil Conservation Service, Moab, Utah. personal communication.

Leonard, R. E., A. L. Leaf, J. V. Berglund, and P. J. Craul. 1971. Annual soil moisture-temperature patterns as influenced by irrigation. Soil Science 111:220-227.

Lillesand, T. M. and R. W. Kiefer. 1979. Remote Sensing and Image Interpretation. John Wiley and Sons, New York, NY.

Lorenz, D. 1966. The effect of the longwave reflectivity of natural surfaces on surface temperature measurements using radiometers. Journal of Applied Meteorology 5:421-430.

Losche, C. K., R. J. McCracken, and C. B. Davey. Soils of steeply sloping landscapes in the southern Appalachian mountains. Soil Science Society of America Proceedings 34:473-478.

Lougeay, R. 1982. Landsat thermal imaging of alpine regions. Photogrammetric Engineering and Remote Sensing 48:269-273.

McDole, R. E. and M. A. Fosberg. 1974. Soil temperature in selected southeastern Idaho soils: I. Evaluation of sampling techniques and classification of soils. II. Relation to soil and site characteristics. Soil Science Society of America Proceedings 38:480-491.

Marshall, T. J. and J. W. Holmes. 1979. Soil Physics, Cambridge University Press, Cambridge, MA.

Merva, G. E. 1975. Physioengineering Principles. The AUE Publisning Company, Inc., Westport, CT.

McLerron, J. H. and O. J. Morgan. 1965. Thermal mapping of Yellowstone National Park in Proceedings of the Fourth International Symposium on Remote Sensing of Environment, Ann Arbor, MI.

Merembeck, B. F. and F. Y. Borden. 1978. Principal components and canonical analysis for reduction of the dimensionality of large data sets. ORSER Tech. Report 5-78. The Pennsylvania State University, University Park, PA.

Millard, J. P., R. D. Jackson, R. C. Goettelman, R. J. Reginato, and S. B. Idso. 1978. Crop water-stress assessment using an airborne thermal scanner. Photogrammetric Engineering and Remote Sensing 44:77-85.

Mimms, D. L. 1982. Multi-temporal Landsat Data for Desert Soil Mapping. M.S. Thesis. The Pennsylvania State University. University Park, PA.

Mueller, O. P. 1970. Soil temperature regimes in a forested area of the northern Rockies. Soil Science 109:40-47.

Munn, L. C., B. A. Buchanan, and G. A. Nielsen. 1978. Soil temperatures in adjacent high elevation forests and meadows of Montana. Soil Science Society of America Journal 42:982-983.

Myers, W. L. 1980. Users Guide to EZLS Regression Program. Information Report 114/OR, ORSER, The Pennsylvania State University, University Park, PA.

Myers, V. I. and D. G. Moore. 1974. Remote sensing for defining aquifers in glacial drifts in Proceedings of the Eighth Symposium on Remote Sensing of the Environment, Ann Arbor, MI.

Newhall, F. 1980. Calculation of Soil Moisture Regimes from the Climatic Record.

NASA. 1978. Heat Capacity Mapping Mission (HCMM) Data Users Handbook for Applications Explorer Mission A (AEM). Goddard Space Flight Center, Greenbelt, MD.

NOAA Climatological Data — Utah. (monthly with annual summaries). EDIS, National Climatic Center, Asheville, NC.

Oke, T. R. 1978. Boundary Layer Climates. Methuen and Co., Ltd., London.

Pinter, P. J., M. E. Stanghellini, R. J. Reginato, S. B. Idso, A. D. Jenkins, and R. D. Jackson. 1979. Remote detection of biological stresses in plants with infrared thermometry. Science 205:585-587.

Platt, C. M. R., and Troup, A. J. 1973. A direct comparison of satellite and aircraft infrared (10-12 micron) remote measurements of surface temperature. Remote Sensing of Environment 2:243-247.

Pratt, D. A. and C. D. Ellyett. 1979. The thermal inertia approach to mapping of soil moisture and geology. Remote Sensing of Environment 8:151-168.

Price, J. C. 1981. The contribution of thermal data in Landsat multispectral classification. Photogrammetric Engineering and Remote Sensing 47:229-236.

Radke, J. D. 1982. Managing early season soil temperatures in the northern corn belt using configured soil surfaces and mulches. Soil Science Society of America Journal 46:1067-1071.

Reginato, R. J., S. B. Idso, J. F. Vedder, R. D. Jackson, M. B. Blanchard and R. Goettelman. 1976. Soil water content and evaporation determined by thermal parameters obtained from ground-based and remote measurements. Journal of Geophysical Research 81:1617-1620.

Richmond, G. M. 1962. Quaternary Stratigraphy of the La Sal Mountains. Geological Survey Professional Paper 324. U. S. Government Printing Office, Washington, DC.

Rieger, S. 1973. Temperature regimes and classification of some well-drained alpien soils in Alaska. Soil Science Society of America Proceedings 37:806-807.

Schmidlin, T. W. 1981. A Statistical Description of Nevada Soil Temperatures. M. S. Thesis. University of Nevada, Reno, NV.

Schmugge, T. 1978. Remote sensing of soil moisture. Journal of Applied Meteorology 17:1549-1557.

Schneider, S. R., D. F. McGinnis, Jr., and J. A. Pritchard. 1979. Use of satellite infrared data in geomorphology studies. Remote Sensing of Environment 8:313-330.

Schrier, H., L. C. Goodfellow, and L. M. LavKulich. 1982. The use of digital multi-date Landsat imagery in terrain classification. Photogrammetric Engineering and Remote Sensing 48:111-119.

Shul'gin, A. M. 1965. The Temperature Regime of Soils. Sivian Press, Jerusalem.

Smith, G. D., F. Newhall, L. H. Robinson, and D. Swanson. 1964. Soil Temperature Regimes — Their Characteristics and Predictability SCS-TP-144, Soil Conservation Service, USDA, Washington, DC.

Smith, G. D. and M. Leamy. 1981. Conversations in taxonomy. Soil Survey Horizons 22:9-14.

Soer, G. J. R. 1980. Estimation of regional evapotranspiration and soil moisture conditions using remotely sensed crop surface temperatures. Remote Sensing of Environment 9:27-45.

Soil Survey Staff. 1975. Soil Taxonomy. Agricultural Handbook 436, USDA. U.S. Government Printing Office, Washington, DC.

Stoner, E. R. and M. F. Baumgardner. Characteristic variations in reflectance of surface soils (unpublished manuscript) Agricultural Experiment Stations, Purdue University, West Lafayette, IN.

Stowe, D. A. and J. E. Estes. 1981. Landsat and digital terrain data for county-level resource management. Photogrammetric Engineering and Remote Sensing 47:215-222.

Stowe, L. L. and H. E. Fleming. 1980. The error in satellite retrieved temperature profiles due to the effects of atmospheric aerosol particles. Remote Sensing of Environment 9:57-64.

Sutherland, R. A. and J. F. Bartholic. 1977. Significance of vegetation in interpreting thermal radiation from a terrestrial surface. Journal of Applied Meteorology 16:759-763.

Taylor, S. E. 1979. Measured emissivity of soils in the southeastern United States. Remote Sensing of Environment 8:359-364.

Thompson, T. H. 1977. Use of infrared imagery in bank-storage studies. U.S. Geological Survey Journal of Research 5:1-10.

Turner, B. J. 1979. Classification and mapping of defoliated and undefoliated central Pennsylvania hardwood forests using two-date Landsat and topographic data. ORSER Technical Report 2-79. The Pennsylvania State University, University Park, PA.

Turner, B. J., G. M. Baumer, and W. L. Myers. 1982. The ORDER Remote Sensing Analysis System: A User's Manual. Research Publication 109/OR, ORSER, The Pennsylvania State University, University Park, PA.

Vann, J. R. and M. G. Cline. 1975. Estimating the mean annual soil temperature of areas correlated as the same soil series where both elevation and latitude vary. Journal of Soil and Water conservation 30:85-87.

Vincent, R. K. 1975. The potential role of thermal infrared multispectral scanners in geological remote sensing. Proceedings of the IEEE 63:137-147.

Vincent, R. K., J. B. Parrish, D. H. Coupland and E. Jaworski. 1981. HCMM Nighttime thermal IR imaging experiment in Michigan in Fifteenth International Symposium on Remote Sensing of Environment, Ann Arbor, MI.

Watson, K. 1975. Geologic Applications of thermal infrared images. Proceedings of the IEEE 63:128-136.

Watson, K., S. H. Miller, and D. L. Sawatzky. 1982. Registration of Heat Capacity Mapping Mission day and night images. Photogrammetric Engineering and Remote Sensing 48:263-268.

Whiting, J. M. 1976. Determination of groundwater inflow to prairie lakes using remote sensing. IEEE: Transactions on Geoscience Electronics 14:60-65.

Whittaker, R. H., S. W. Buol, W. A. Niering, and Y. H. Havens. 1968. A soil and vegetation pattern in the Santa Clara Mountains, Arizona. Soil Science 105:440-450.

Williams, D. L. and K. J. Ingram. 1981. Integration of digital elevatoin model data and Landsat MSS data to quantify the effects of slope orientation on the classification of forest canopy condition in Machine Processing of Remotely Sensed Data Symposium.

Wilson, L., M. E. Olsen, T. B. Hutchings, A. R. Southard and A. J. Erickson. 1975. Soils of Utah. Agricultural Experiment Station Bulletin 492, Utah State University, Logan, Utah.

APPENDIX A

DESCRIPTION OF ORSER SOFTWARE SYSTEM

(reproduction of: Newcomer, J. A., B. J. Myers, and W. L. Myers, 1981. ORSER Program Descriptions, ORSER Information Report 119/OR, The Pennsylvania State University, University Park, PA.)

ORSER PROGRAM DESCRIPTIONS

The ORSER data processing system consists of three major subsystems: preprocessing, analysis, and display. Detailed program descriptions may be found in the ORSER User Manual (Turner et al., 1978).

The Preprocessing Subsystem

Preprocessing of data tapes in the ORSER system involves the functions of reformatting, data management, geometric correction, and data transformation. Programs for these functions are described below. In cases where one is not sure of the contents of a tape, the TPINFO program can be used to output such information.

Reformatting Programs

The SUBSET program subsets an area of interest from a larger data set. This can be done from several satellite data formats, including those from Landsat, Skylab, Seasat, and the Heat Capacity Mapping Mission (HCMM). The original format is specified on a control card, as are the areas to be subset. The new data set is output in ORSER format, which increases processing efficiency and reduces computation costs for the subsequent analysis steps. Further subsets of the new data set may also be made. The SUBAIR program is similar to SUBSET, except that it subsets and reformats data from aircraft scanners.

The REFORMAT program outputs data in ORSER format from file-sequential tapes generated by the Video Image Communications and Retrieval (VICAR) image processing system and by digitizing systems such as the Optronics Scanning Densitometer. File-sequential multispectral scanner (MSS) tapes contain each spectral channel response for an image in a separate file. The program outputs these files to disk workspaces and then generates output on which each record contains all elements and channels for each scan line. Up to eight files may be reformatted in one run.

The RFMTDTT program reformats Digital Terrain Tapes (DTT's) into ORSER format. An entire DTT is reformatted in one run. The elevation information is scaled from 1 to 255, to fit into one byte on a nine-track tape. The data set is reoriented, to start from the northwest corner of the scene and proceed eastward, and then output in ORSER format. After reformatting, the data can be geometrically corrected and rubber-sheet stretched to overlay spectral information.

Data Management Programs

The MERGE program is used to merge satellite data from two ORSER format tapes containing data from passes of the same area from different dates. Up to six passes may be merged. The program is useful for studying temporal changes and for improving the classification of certain targets.

The SPAN program is used either to join data from adjacent panels of the same Landsat scene or to concatenate data from two consecutive Landsat scenes of the same pass. Landsat or ORSER formatted data can be used.

The SUBOUND program is a version of SUBSET used to subset irregularly bounded areas from larger data sets. These areas are defined by pairs of coordinates designating corners of a polygon.

The CONSOL program consolidates data blocks from two separate tapes onto a single tape or file for simultaneous analysis. Data in ORSER or Landsat formats may be used, with output being in ORSER format.

Geometric Correction Programs

The EZLS program is a general purpose least squares analysis program designed for both simplicity and flexibility. The program accommodates 30 independent variables; however, its capacity can easily be increased by redimensioning. (Myers, 1980) In the context of the ORSER system, EZLS generates polynomial transformation functions for geometric correction.

The SUBGM program geometrically corrects, rotates, scales, and/or rubber-sheet stretches a data set as it is being subset. The nearest-neighbor rule or the cubic convolution method may be used on an ORSER or a Landsat format tape. The UTILGM program can be used to determine the maximum number of scan lines that can be operated on by a run of SUBGM. This number is dependent on the number of elements per line and the amount of rotation desired.

Data Transformation Programs

The SUBTRAN program provides data handling capabilities which are not available in the other subsetting programs. These include linear data transformation; channel ratioing, scaling and translation; gray scale adjustment; data truncation; and channel and pixel averaging. Linear data transformation is generally used with a canonical transformation matrix generated by the CANAL program. However, any conformable transformation matrix may be used to premultiply the data elements. Because SUBTRAN requires a large amount of storage (280,000 bytes), it should not be used if its additional data handling abilities are not required. Output from the program can be in ORSER or a Landsat format, or in a format for use on a film recorder.

The RSCOR program accepts as input a covariance matrix containing up to 32 variables. It then outputs partial and multiple correlations, and the coefficient of determination.

The ROTATE program determines the principal component axes of an input covariance matrix. These axes are defined such that the first explains as much of the population dispersion as possible. The second, orthogonal to the first, explains as much of the remaining variance as possible. The third and subsequent axes, orthogonal to all previous axes, explain as much residual variance as possible. Generally, the first few axes explain most of the dispersion of the data. Thus, the dimensionality of the data set may be reduced from p-correlated to q-independent variates, where $q \leq p$. If desired, the program will rotate axes to have equal variance. This is a useful option for display on color devices.

The CANAL program is used to perform a canonical analysis on the MSS data based on the mean vectors, covariance matrices, and the number of observations for each category. The categories and their statistics must be obtained prior to using the program. The analysis performed by CANAL yields the minimum number of linear transformations that give maximum separability of the categories. Output consists of tables of matrices and category comparative and separability statistics. As a preprocessing method for MSS data, canonically transformed data have the following useful properties:

1. Under the assumption of equal category covariance matrices, canonical transformation yields data that may be classified by using the simpler, faster, and less expensive minimum Euclidean distance classifier rather than the optimum Bayesian maximum likelihood classifier.

2. Correlations of the original axes with the transformed axes can be used to interpret the ability of each original axis to discriminate among categories. Channels having weak correlations with the transformed channels are of little discriminant value, whereas those with large correlations are valuable for category discrimination.

3. In feature selection, canonical analysis can be used to reduce data dimensionality. Because the axes are statistically independent, and those with large variances may be assumed to have the greatest discriminatory power, the user may select for classification only those axes of highest information content.

The SUBTEXT program extracts textural features (the distribution of gray-levels across an image) from multispectral data for classification of terrain features. Eleven possible statistics can be calculated for each local area of 3-by-3 or 5-by-5 pixels. These include mean vector length, variance of vector lengths, measures of skewness and kurtosis, and a few distance measurements between vector endpoints. Each statistic becomes an additional component of the existing channel response vector.

The Analysis Subsystem

Most of the programs in the analysis subsystem either produce character maps on a line printer or a compressed map in a computer file which can be used to produce displays offline.

The NMAP program is designed to assist the user in visually recognizing and correlating blocks of MSS data on tape with areas seen on corresponding photography. The vector of channel responses for each pixel is used to calculate the vector norm, which serves as a measure of brightness. This representation of vector length is then level-sliced for purposes of mapping. NMAP can also be used for image enhancements, such as contrast stretching.

The UMAP program is used to map areas of spectral uniformity for use as spectral signature training fields, and to delineate areas of high

contrast and their boundaries. The uniformity matrices used by UMAP are weighted Euclidean distances between adjacent pixel vector endpoints. The UMAP program may be run with normalized or unnormalized data.

The CLUS program can be used for unsupervised classification and mapping of normalized or unnormalized MSS data. Instead of the user specifying a set of spectral signatures to be used in classification, a clustering algorithm develops its own signatures based on a determination of natural groupings of the data vectors in spectral space. The data are input in ORSER format with an operator-chosen critical distance or angle (for normalized data) to be used for initial clustering decisions. The program randomly selects the number of sample pixels needed to determine signatures for the categories present in the data block.

The STATS program is used to obtain basic statistical information for selected training areas in a data set. The program computes the class mean vector, the vector of standard deviations, and the covariance matrix for the chosen channels in a specified area. Histograms for the channel responses, a correlation matrix for the channels, and eigenvalues and eigenvectors can also be output. Each area of interest is defined by pairs of coordinates designating corners of a polygon that may not have more than 30 sides. Two or more areas may be combined if they do not overlap. The data must be in ORSER format.

USTATS is a hybrid of UMAP and STATS which computes category statistics based on groups of elements that exhibit a specified level of local uniformity.

The CLASS program classifies and maps MSS normalized or unnormalized vectors using the method of minimum Euclidean distance classification. With normalized data, classification is done on the measure of angular separation between given prototype or category mean vectors and the vectors input. Classification maps and tables, consisting of distances or angles of separation between categories, are output.

The MAXCLASS program assumes that the data follow a multivariate normal distribution. Each category is defined by a mean or prototype vector and a covariance matrix. The data are classified by their weighted distances of separation from each category, as set up by the Bayesian maximum likelihood criterion.

The RATIO program classifies areas using an algorithm based on the ratio of two selected channel responses. The ratio determination is made for each pixel selected that is within a given tolerance of the selected signatures. The pixel is then classified on the basis of the set of class boundaries the ratio falls between. Output consists of a character map and frequency-distribution tables for the ratioed values.

The PPD program is a modification of the CLASS program based on parallelepiped classification. The spectral characteristics of the classes are defined by upper and lower bounds for each channel.

The STCLASS program combines the CLASS program with the computational facilities of the STATS program. It generates new mean vectors, covariance and correlation matrices, and other statistics from the total set of observations and outputs a classification map.

The MAPCOMP program compares two character maps, element-by-element, and produces a comparison map with summary tables. MAPCOMP is useful for comparing maps obtained from different Landsat passes of the same area, and for comparing the results of two different analysis schemes applied to the same data set.

The Display Subsystem

Some programs in the display subsystem generate specialized line printer maps, while others convert a compressed map into a form suitable for offline production on devices such as cathode ray tubes or film recorders.

The DISPLAY program can be used to generate gray or color tone maps from input character maps. Multiple map copies can be printed and stray symbols can be cleaned from the output map. More commonly, however, the program is used to output data to the Ramtek color display system, a Versatec electrostatic printer/plotter or a film recorder. The output medium may be in the form of magnetic tapes, cards, or magnetic disc files.

The LMAP program is useful for producing small maps for publication. It generates black-and-white line maps, scaled to given specifications, and outputs them on a line plotter or on the screen of a Tektronix 4010 cathode ray tube terminal. LMAP accepts compressed character map data in ORSER format.

The DISPGM program geometrically corrects, rotates, scales, and rubber-sheet stretches character map input. Although it can output a line-printer map, its output is usually input to the DISPLAY program to take advantage of a greater variety of display options.

REFERENCES

Myers, W. L. 1980. User's Guide to EZLS Regression Program. Information Report 114/OR. Office for Remote Sensing of Earth Resources, Institute for Research on Land and Water Resources, The Pennsylvania State University.

Turner, B. J., D. N. Applegate, and B. F. Merembeck. 1978. Satellite and Aircraft Multispectral Scanner Digital Data User Manual. ORSER Technical Report 9-78. Office for Remote Sensing of Earth Resources, Institute for Research on Land and Water Resources, The Pennsylvania State University.

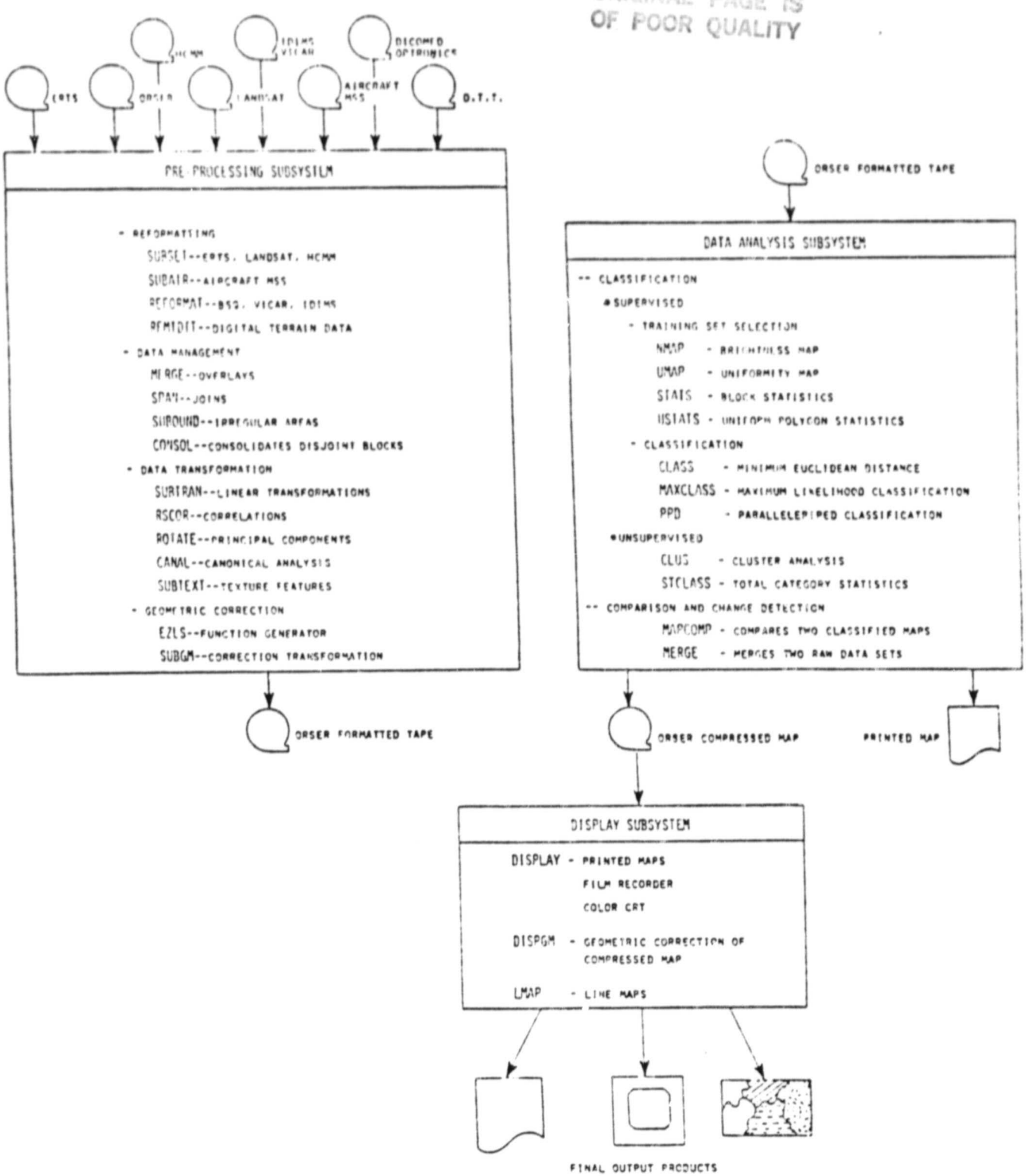

APPENDIX B

SOIL CONSERVATION SERVICE GENERAL SOILS MAPS AND DESCRIPTIONS

GENERAL SOILS MAP OF STUDY SITE

NORTH OF THE COLORADO RIVER

ORIGINAL PAGE
COLOR PHOTOGRAPH

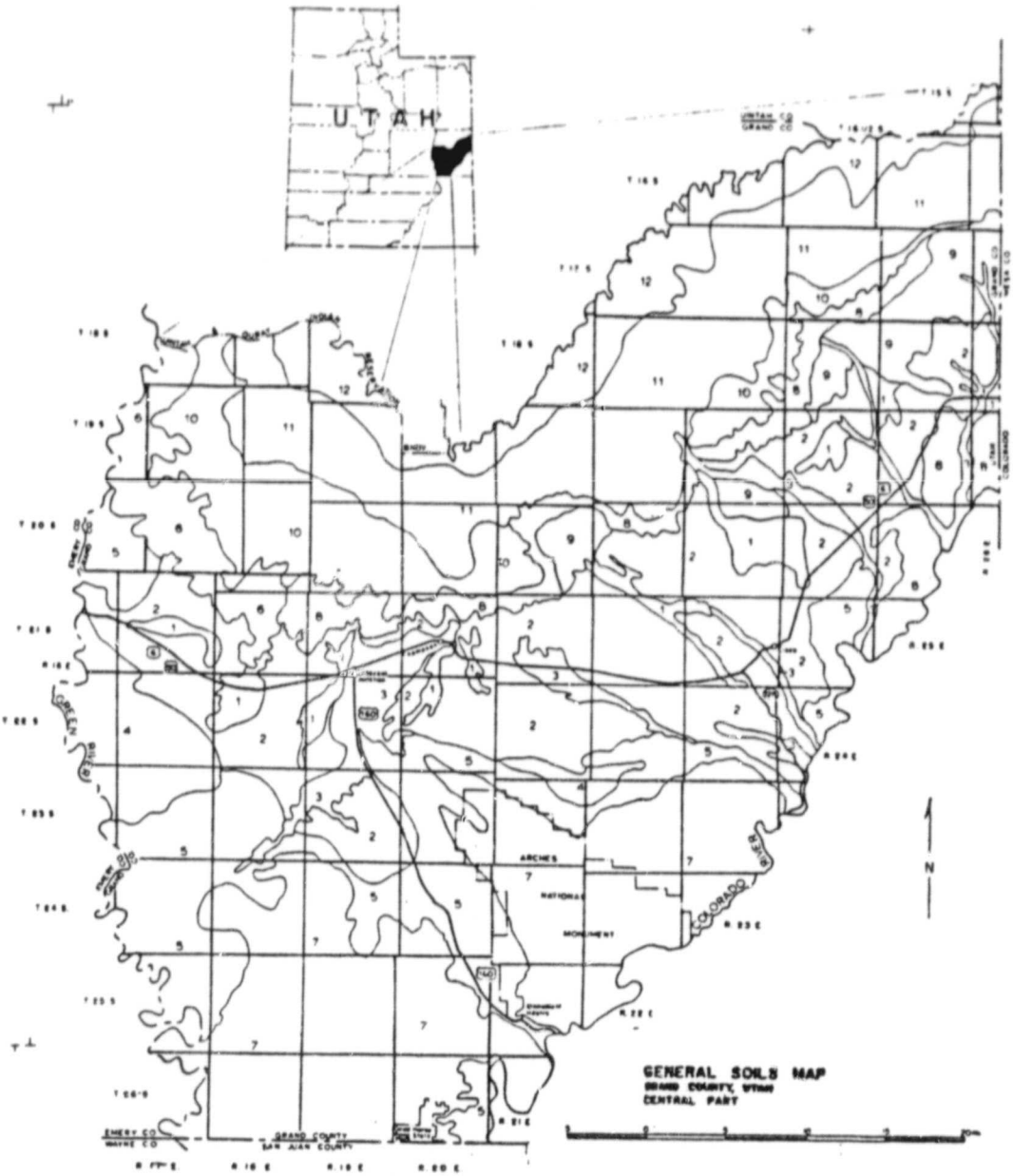

GRAND COUNTY UTAH

General Soil Map

Map Units

DOMINANTLY WELL DRAINED, NEARLY LEVEL TO MODERATELY STEEP SOILS ON STRUCTURAL BENCHES, CUESTAS, BOLSONS, SHALE PEDIMENTS, AND ALLUVIAL FAN PEDIMENTS IN ARID CLIMATE.

1. Mesa-Mack-Chipeta

   Shallow to very deep, well drained, gently sloping to moderately steep soils on alluvial fan pediments and shale plains.

2. Chipeta-Killpack-Blueflat

   Shallow to moderately deep, well drained, gently sloping to steep soils on shale plains, pediments, cuestas, and bolsons.

3. Toddler-Ravola-Glenton families

   Very deep, well drained, gently sloping soils on fans, flood plains, and along drainages.

4. Badland-Rock outcrop-Moenkopie

   Badland, Rock outcrop, and shallow, well drained, gently sloping to moderately steep soils formed in residuum from sandstone and interbedded shale on structural benches, ridgetops, and sideslopes.

5. Moenkopie-Nakai-Rock outcrop

   Shallow to deep, well drained, gently sloping to moderately steep soils, formed in residuum, alluvium, and some eolian materials from sandstone, on cuestas, structural benches, and valley sideslopes; and Rock outcrop.

6. Thedalund family, stony-Walknolls family-Pennell

   Shallow to deep, well drained, sloping to very steep soils on cuestas, benches, and in canyons.

DOMINANTLY WELL DRAINED, GENTLY SLOPING TO VERY STEEP SOILS ON STRUCTURAL BENCHES, CUESTAS, BENCHES, MESAS, AND CANYON ESCARPMENTS IN SEMIARID CLIMATE ZONE.

7. Rizno-Begay-Rock outcrop

   Shallow to very deep, well drained, gently sloping to moderately steep soils on structural benches, cuestas, and mesas.

8. Shalako, dry-Thedalund family, stony-Hanksville family

   Shallow to deep, well drained, gently sloping to very steep soils on benches, cuestas, alluvial fans, and canyon escarpments.

9. Barx-Strych

   Shallow to very deep, well drained, gently sloping to moderately steep soils on alluvial fan pediments, alluvial fans, and shall pediments.

DOMINANTLY WELL DRAINED, STEEP AND VERY STEEP SOILS ON CANYON ESCARPMENTS AND MOUNTAIN SIDESLOPES IN SEMIARID AND DRY SUBHUMID CLIMATE ZONE.

10. Thedalund family, moist-Thedalund family, stony-Dast family

    Moderately deep to deep, well drained, steep and very steep soils on canyon escarpments and mountain sideslopes.

DOMINANTLY WELL DRAINED, SLOPING TO VERY STEEP SOILS ON MOUNTAIN SIDESLOPES AND BENCHES IN SUBHUMID AND HUMID CLIMATE ZONE.

11. Dast family-Reva family-Shalako

    Shallow to very deep, well drained, sloping to very steep soils on benches and mountain slopes.

12. Sula family-Razorba family, warm-Reva family

    Shallow to very deep, well drained, steep and very steep soils on mountain slopes.

GENERAL SOILS MAP OF STUDY SITE

SOUTH OF THE COLORADO RIVER

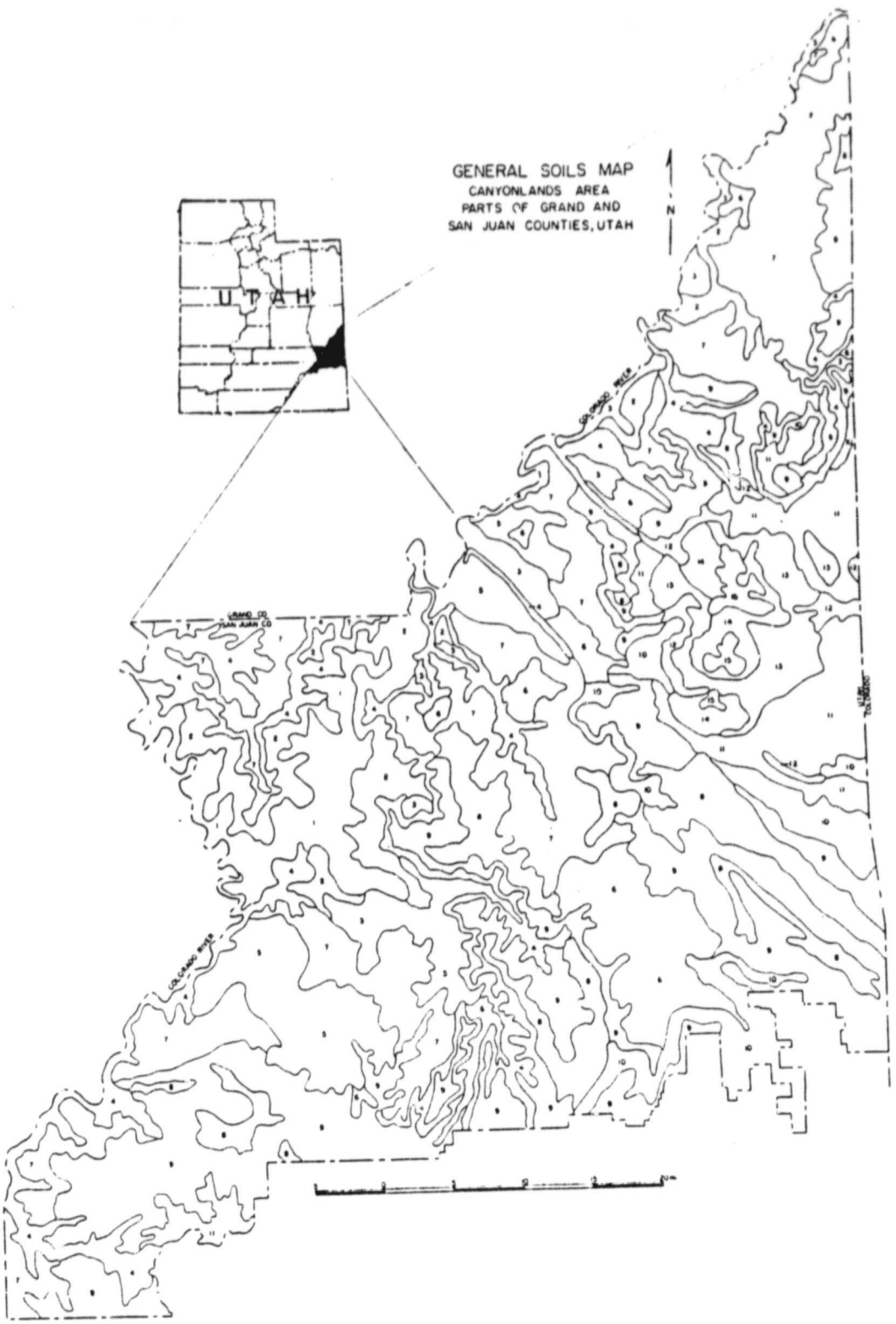

CANYONLAND AREA UTAH

General Soil Map

Map Units

DOMINANTLY WELL DRAINED AND SOMEWHAT EXCESSIVELY DRAINED, NEARLY LEVEL TO MODERATELY STEEP SOILS ON LOW BENCHES, TERRACES, CUESTAS, AND VALLEYS IN ARID CLIMATE ZONE.

1. Rock outcrop-Moenkopie

   Rock outcrop, and very shallow and shallow, well drained, gently sloping to moderately steep soils formed in residuum from sandstone and shale; on low benches and cuestas.

2. Moenkopie-Rock outcrop-Hoskinnini

   Very shallow and shallow, well drained, nearly level to moderately steep soils formed in residuum from sandstone, shale and limestone; on low benches and cuestas, and Rock outcrop.

3. Thoroughfare-Sheppard-Monue

   Deep and very deep, well drained and somewhat excessively drained, nearly level and gently sloping soils formed in alluvium and eolian deposits from sandstone and shale; on valley floors, low benches and terraces.

DOMINANTLY, WELL DRAINED TO EXCESSIVELY DRAINED, GENTLY SLOPING TO EXTREMELY STEEP SOILS ON BENCHES, CUESTAS, MESAS, ESCARPMENTS AND CANYON WALLS IN SEMIARID CLIMATE ZONE.

4. Ustic Torriorthents-Lithic Torriorthents-Rock outcrop

   Very shallow to very deep, well drained and somewhat excessively drained, steep to extremely steep soils formed in colluvium and residuum from sedimentary rocks; on escarpments and canyon walls, and Rock outcrop.

5. Rock outcrop-Rizozo-Mespun

   Rock outcrop, and very shallow to very deep, well drained to excessively drained, gently sloping to extremely steep soils formed in colluvium, residuum, alluvium and eolian deposits from sandstone and shale; on escarpments, canyon walls, mesas, benches and cuestas.

DOMINANTLY WELL DRAINED AND SOMEWHAT EXCESSIVELY DRAINED, NEARLY LEVEL TO STRONGLY SLOPING SOILS ON BENCHES, TERRACES, FANS, MESAS AND VALLEYS IN SEMIARID CLIMATE ZONE.

6. Begay-Windwhistle-Ildefonso

Moderately deep to very deep, well drained and somewhat excessively drained, nearly level and gently sloping soils formed in alluvium and eolian deposits from sandstone; on benches, terraces and valleys.

7. Rizozo-Rock outcrop

Very shallow and shallow, well drained, gently sloping to strongly sloping soils formed in residuum from sandstone, and some igneous and metamorphic rocks; on benches, cuestas and mesas, and Rock outcrop.

DOMINANTLY WELL DRAINED, NEARLY LEVEL TO VERY STEEP SOILS ON UPLAND BENCHES, FANS, CUESTAS, HILLSIDES AND ESCARPMENTS IN DRY SUBHUMID CLIMATE ZONE.

8. Palma-Cahona-Hagerman

Moderately deep to very deep, nearly level and gently sloping soils formed in eolian deposits and alluvium from sandstone; on upland benches, fans and cuestas.

9. Rizozo-Rock outcrop-Ildefonso

Very shallow to very deep, gently sloping to moderately steep soils formed in residuum, eolian deposits and alluvium from sandstone and diorite; on upland benches, cuestas and fans, and Rock outcrop.

10. Ustic Torriorthents-Ustollic Calciorthids-Ustollic Haplargids

Moderately deep to very deep, strongly sloping to very steep soils formed in residuum and colluvium from shale and sandstone; on hillsides, landslides and escarpments.

DOMINANTLY WELL DRAINED, GENTLY SLOPING TO VERY STEEP SOILS ON HIGH BENCHES, FANS, LANDSLIDES AND ESCARPMENTS IN MOIST SUBHUMID AND HUMID CLIMATE ZONES.

11. Herm-Hangdo-Falcan

    Shallow to very deep, gently sloping to moderately steep soils formed in alluvium, colluvium, and eolian deposits from igneous and sedimentary rocks; on high benches, fans, and landslides.

12. Ponil-Falcon-Toone

    Shallow to very deep, moderately steep to very steep soils formed in residuum, colluvium and alluvium from sedimentary rocks; on landslides and escarpments.

DOMINANTLY WELL DRAINED, GENTLY SLOPING TO EXTREMELY STEEP SOILS ON HIGH MOUNTAINSIDES, FANS, LANDSLIDES AND CIRQUES IN HUMID CLIMATE ZONE.

13. Flygare-Skylick-Sligting

    Very deep, gently sloping to steep soils formed in colluvium and alluvium from diorite, shale and sandstone on high mountainsides, fans and landslides.

14. Duchesne-Leighcan-Broad Canyon

    Deep and very deep, strongly sloping to extremely steep soils formed in colluvium and glacial till from diorite; on high mountainsides.

15. Rubble land-Leighcan-meredith

    Rubble land, and deep and very deep moderately steep to extremely steep soils formed in colluvium from diorite; on high mountainsides and cirques.

APPENDIX C

WARP PROGRAM DESCRIPTION

WARP PROGRAM DESCRIPTION

R. L. Day

The WARP program is used to graphically display the spatial distortion that a digital data set undergoes when it is registered to another digital data set or rectified to a cartographic base map. The magnitude and distribution of the distortion can be interpreted to evaluate control point and transformation model selection. Details of cartographic correction are described in the ORSER User's Manual. The WARP program uses several ORSER subroutines written by Danielle Applegate.

The WARP program transforms "original" space scan line and element coordinates to "corrected" space coordinates. "Original" space coordinates are entered on a BLOCK card. Transformation model coefficients are entered on COEF cards (see EZLS Program Description in ORSER User's Guide).

"Corrected" space scan line and element coordinates are then plotted on either a Houston Instruments or Versatec plotter. Coordinate nodes are connected with lines which represent rows and columns of pixels. Control point coordinates can be plotted on the output grid to show their spatial distribution.

Control Cards

All values are integer format and right justified in the field unless specified.

BLOCK Card

Cols.	Description of Contents
1-5	BLOCK
9-13	Beginning scan line
14-18	Ending scan line
19-23	Beginning element
24-28	Ending element
29-33	Scan line increment
34-38	Element line increment

The BLOCK card specifies input block specifications. The scan line and element line increment indicate the sampling interval of input coordinate nodes which will be plotted. For example, a scan line increment of 2 result in every other scan line being plotted.

COEF Card

The ORSER User's Guide describes in detail the format of the COEF card. In WARP only two COEF cards are used at a time. Coefficient describing transformation equations F3 and F4 are used but are entered on COEF cards numbered COEF1 and COEF2 instead. This differs from the use of COEF cards in SUBGM or SUBTRAN.

AXES Card (Optional)

Cols.	Description of Contents
1-4	AXES
9-13	Scan line color or thickness (integer)
14-18	Element line color or thickness (integer)
19-23	Scan line label color or thickness (integer)
24-28	Element line label color or thickness (integer)
29-33	Labelling increment (integer)

The axes card describes colors of lines and labels on the Houston Instruments plotter (1=BLACK, 2=RED, 3=GREEN, 4=BLUE) on line thickness on the Versatec plotter. Values range from 1 (0.005 inch) to 5 (0.025 inch) in 0.005 inch increments. The labelling increment describes the interval of labels on both rows and columns.

SPLIT Card (optional)

Cols.	Description of Contents
1-5	SPLIT
13	1 means plot scan lines (black otherwise)
18	1 means plot element lines (black otherwise)

A split card allows rows (scan lines) and columns (element lines) of the output plot to be plotted separately or individually.

VTEC Card (optional)

Cols.	Description of Contents
1-4	VTEC

Directs output to a Versatec electrostatic plotter rather than the default Houston Instruments.

SCALE Card (optional)

Cols.	Description of Contents
1-5	SCALE
9-13	Scale factor (real format)

A scale card scales the output plot. By default, the plot occupies the maximum area allowed by the selected plotter.

CP Card (optional)

Cols.	Description of Contents
1-2	CP
6-7	Number of control points

The CP is used to plot the location of control points on the output plot. Following the CP card, the coordinates (scan lines and elements) of the control points must follow with the following format for each control point:

Cols.	Description of Contents
1-7	Element coordinate (real format)
10-17	Scan line coordinate (real format)

The number of control point coordinates must equal the number of control points entered on the CP card.